NUMERICAL MODELING OF DUCTILE FRACTURE

A Dissertation

Presented to

The Graduate Faculty of The University of Akron

In Partial Fulfillment

of the Requirements for the Degree

Doctor of Philosophy

Jun Zhou

December, 2013

NUMERICAL MODELING OF DUCTILE FRACTURE

Jun Zhou

Dissertation

Approved:

_____
Advisor
Dr. Xiaosheng Gao

_____
Committee Member
Dr. Shing-Chung Wong

_____
Committee Member
Dr. Gregory Morscher

_____
Committee Member
Dr. Ernian Pan

_____
Committee Member
Dr. Kevin Kreider

Accepted:

_____
Department Chair
Dr. Sergio Felicelli

_____
Dean of the College
Dr. George K. Haritos

_____
Dean of the Graduate School
Dr. George R. Newkome

_____
Date

ABSTRACT

This thesis sought to investigate and develop valid numerical approaches to predict ductile fracture under different stress state and loading conditions.

As the first portion of this work, the plastic flow and fracture behaviors of three aluminum alloys (5083-H116, 6082-T6 and 5183 weld metal) under the effects of strain rate and temperature were studied through a series of experiments and finite element analyses. The fracture behavior under the influential factor of stress triaxiality was also studied. The applicability of the Johnson-Cook plasticity and fracture models were investigated with mixed results. For all three materials, the dependency of the failure strain on triaxiality is adequately described.

The stress state effect on plasticity and ductile fracture behaviors was further explored for aluminum alloy 5083-H116 through tests on plane strain specimens and torsion specimens, focusing on the third deviatoric stress invariant (lode angle). A stress state dependent plasticity model, J_2-J_3 model, together with the Xue-Wierzbicki fracture criterion which defined the damage parameter as a function of the stress triaxiality and the Lode angle, was implemented and calibrated with the test data. The calibrated model was utilized to study the residual stress effect on ductile fracture resistance, using compact tension specimens with residual stress fields generated from a local out-of-plane

compression approach. Fracture tests with positive and negative residual stresses were conducted on the C(T) specimens. Both experimental and finite element results showed significant effect of residual stress on ductile fracture resistance.

In an attempt to predict ductile fracture under shear-dominated conditions, this study combined the damage mechanics concept with the Gurson-Tvergaard-Needleman porous plasticity model that accounts for void nucleation, growth and coalescence. The GTN model was extended by coupling two damage parameters, representing volumetric damage and shear damage respectively, into the yield function and flow potential. The new model was validated through a series of numerical tests in comparison with existing GTN type models, and applied to predict the ductile fracture behaviors of a beta-treated Zircaloy-4. With model parameters calibrated using experimental data, the model was able to predict failure initiation and propagation in various specimens experiencing a wide range of stress states.

ACKNOWLEDGEMENTS

The accomplishment of this degree program would be impossible without the knowledgeable guidance and continuous support from my advisor, Dr. Xiaosheng Gao. I would like to take this opportunity to thank him for his help over the 5 years.

I would also like to express my sincere appreciation to my committee faculty members: Dr. Shing-Chung Wong, Dr. Gregory Morscher, Dr. Ernian Pan, Dr. Kevin Kreider. Their investment in terms of time and ideas are greatly appreciated.

I am also grateful for the friends and group members I got the chance to interact with on the daily basis, including Sunil Parakash, Tingting Zhang, Tuo Luo, Yuan Zhai, Wenzhi Wang, Shen Shang, Yifei Gao, Chao Zhang. Special thanks to Dr. Liang Xue at the Northwestern University for his valuable discussion.

Last but not the least, I would like to thank my family, especially my wife Haodan, and hereby dedicate this thesis to them for their endless support.

TABLE OF CONTENTS

LIST OF TABLES

Table Page

LIST OF FIGURES

CHAPTER I

INTRODUCTION

1.1 Background and motivation

Structural fracture has been a big threat to human life and economy. The first historically recorded study of fracture strength was by Leonardo da Vinci (1452- 1519) on the tensile strength of a short iron wire. Since then, understanding on fracture problems has been broadened and deepened, especially after the start of last century. Human efforts in eliminating fracture caused losses have achieved significant success. But more complexities arise nowadays due to emerging new technology, new structure designs and new materials.

Considering the way the material deforms before fracture, fracture is usually classified into two types, brittle or ductile. In ductile fracture, extensive plastic deformation takes place before fracture. On the other hand, brittle fracture happened more suddenly, before apparent plastic deformation takes place. For most industrial applications, materials with higher ductility are usually more desirable when the requirement for strength is satisfied. Ductile materials like metals are widely used in fields of aeronautics, automobiles, nuclear engineering, oil and gas etc. Prevention of ductile failure has been of utmost interest, and tremendous amount of efforts have been made to understand the mechanism of ductile fracture.

Fracture mechanics is a traditional theoretical system that studies fracture behaviors of a material with existing initial macroscopic crack. The crack-opening driving force around a crack tip is evaluated with concepts of the stress intensity factor, energy release rate or J-integral, whose critical value at crack propagation is regarded as fracture toughness. Test standards have been established for obtaining the fracture toughness to characterize the material's resistance to fracture. Fracture mechanics approach has achieved great success in the industrial applications, but has also a number of limitations [1, 2]. Firstly, it can only deal with preexisting cracks and cannot predict crack initiation. Secondly, fracture toughness is not a material intrinsic property as it strongly depends on specimen geometry. At last, the theory doesn't describe the mechanism of material failure at the crack tip. With all these limitations, fracture mechanics cannot be used to model situations with complex loading where the material failure depends strongly on the local stress and deformation histories.

The limitations of the fracture mechanics approach (so called 'Global Approach') led to the development of physics-based damage models which actually describe features of the local damage phenomenon in the rupture process zone (Local Approach to Fracture [3, 4]. This concept provided key insights for development of "transferable" fracture models for damage assessment.

1.2 Ductile failure mechanisms and modeling

From the micro-mechanical point of view, ductile fracture in metallic alloys usually follows a multi-step failure process involving several concurrent and mutually interactive mechanisms [5, 6]: (a) nucleation of microscopic voids by either fracture or

decohesion of the second-phase particles and inclusions, (b) growth of the fine microscopic voids due to localized plastic deformation (c) localization of plastic flow between the growing voids, and (d) final tearing or rupture of the ligaments between the grown and enlarged voids.

1.2.1 Stress state effect

This whole fracture process is strongly affected by the stress state. Research on the effect of the stress state on ductile fracture can be traced back to the early work of Ludwik and Scheu in 1923 [7], in which the authors noticed the effect of maximum principal stress on the fracture. Ludwik's theory was further explored by Orowan [8] in his work on notch brittleness. Experimental evidence of the effect of stress state was given by Bridgman [9] who showed that strains to failure in tension tests were greatly increased under superimposed hydrostatic pressure. The influence of superimposed hydrostatic pressure on the fracture mechanisms of copper, aluminum and brass were also studied by French and Weinrich [10-12], which gave similar results.

In the late 1960s, theoretical studies of micro mechanism of ductile fracture were conducted by McClintock [13], Rice and Tracey [14], who investigated the growth of isolated cylindrical or spherical void surrounded by an ideally plastic matrix subjected to uniform remote stressing. Their works showed the dominant effect of stress state on the void growth rate. Rice and Tracey's solution related the void growth rate to the stress triaxiality directly. Inspire by their findings, Gurson proposed a well-known micro-mechanism based constitutive model, which described the material softening due to void growth [15].

On the other hand, Hancock and Mackenzie [16] proposed an empirical failure initiation criterion based on Rice and Tracey's solution: assuming inverse proportionality of failure strain to the void growth rate, the failure strain is an exponentially decaying function of the stress triaxiality. This empirical failure criterion was validated through tension tests on notched tensile bars conducted by the authors. A widely used ductile fracture criterion was provided by Johnson and Cook [17] , in which a damage parameter was defined as a weighted integral with respect to the effective strain and the integrand is the reciprocal of the effective failure strain as a function of the stress triaxiality, strain rate and temperature. Due to its simple form and broad consideration, the Johnson-Cook fracture models is very popular in industrial applications [18, 19].

The common tribute of the above mentioned papers are that the materials fracture is affected by the stress triaxiality. However, triaxiality seems to be not the only factor that affects ductile rupture. Johnson and Cook [17] observed a phenomenon that, in the torsion test where the triaxiality is lower compared to the tension test, the fracture strain is lower for some material such as 4340 steel. By comparing the experiment data between simple tension test and torsion/shear test, McClintock [20] and Xue [21] both showed that the two types of loading had a mixed effect on the fracture strain magnitude. Bao and Wierzbicki [22] conducted a series of tests including upsetting tests, shear tests and tensile tests on 2024-T351 aluminum alloy, where a wide range of stress triaxiality was covered. It was observed that the dependence of the failure strain on the stress triaxiality was not monotonic. Instead, the relationship followed a trend as shown in Figure 1.1, where three distinct regimes described the different types of tests: for triaxiality between

zero and 0.4, shear fracture is also observed besides void growth; for negative triaxiality, damage is dominated by the shear fracture.

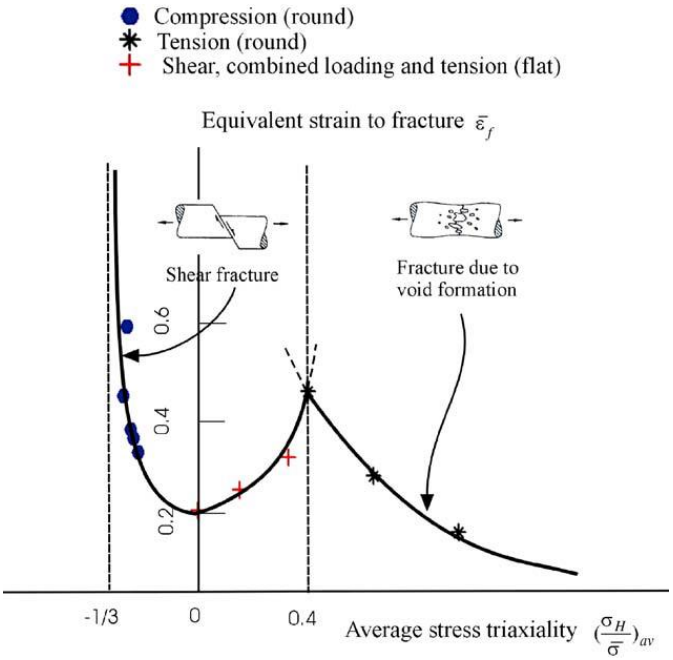

Figure 1. 1 Dependence of the equivalent strain to fracture on the stress triaxiality [22].

The fact that triaxiality is not the only factor that affects ductile rupture leads to the exploration of other possible elements. The Lode angle/parameter, which is related to the third invariant of stress deviatoric, is believed to be a factor that influences the material ductility by many authors. Studies by Kim et al. [23-25] and Gao et al. [26, 27] on the void-contained cell model found that the Lode parameter should be considered in order to distinguish the stress state with the same triaxiality ratio, since the macroscopic stress strain response and the void growth/coalescence behavior of a representative material volume significantly vary for each stress state even though the triaxiality stays the same. Barsoum and Faleskog [28] conducted tests on double notched tube specimen under combined tension and torsion at fixed stress ratios. In their tests, as the triaxiality

decreases with an increasing amount of shearing, a shift in rupture mechanism from void internal necking to internal shearing occurs, accompanied with a dramatic change in the Lode parameter and a significant drop in ductility. Xue and Wierzbicki [29] presented a ductile failure criterion as a function of both stress triaxiality and the Lode angle, and assumed the influence on fracture strain of the two to be independent. Their study results were plotted as a 3-D fracture locus in the space of both triaxiality and the Lode parameter.

1.2.2 Shear-induced damage

From the microscopic point of view, the void growth mechanism is limited under lower triaxiality, when the ductile fracture mainly is caused by shear localization. Under this mechanism, the void size can be much smaller than that for failure governed by void growth and inter ligament necking. From the test of Barsoum and Faleskog [28], the SEM fractographs of ductile fracture in a Weldox 420 presents a shift in rupture mechanism from void internal necking to internal shearing, Figure 1.2.

The formation of shear localization can be attributed to many factors: the material inhomogeneity, plastic yielding vertex, friction, etc [30]. Shear softening due to void distortion and inter-void linking is believed by many authors to be a possible mechanism that leads to shear localization and final fracture. Knowledge of the void shearing mechanisms on softening and shear localization is more qualitative than quantitative. For an initially spherical void in a linearly viscous material, Fleck and Hutchinson [31] observed that the void became spheroidal under remote shearing, and then rotated, before a penny-shaped crack was eventually formed. More recently, Barsoum and Faleskog [32]

conducted a fully three-dimensional (3D) analysis on similar shear specimens containing spherical voids to simulate their experiments [28] of ductile fracture in a double-notched tube specimen under combined tension and torsion. Tvergaard [33] modeled the failure of a row of voids in a shear field, and observed the micro-mechanism features that the voids collapsed to microcracks and continued to rotate and elongate with further shear deformation, until localization of plastic flow occurred. The behavior of initially spheroidal voids in a shear field was also analyzed by Scheyvaerts et al. [34] with different initial orientations of the spheroid. Besides the voids behavior in a shear field, Anderson et al. [35] studied the behaviors of a row of micro-cracks in a material subject to shear, and showed that localization could result from crack rotation and stretching.

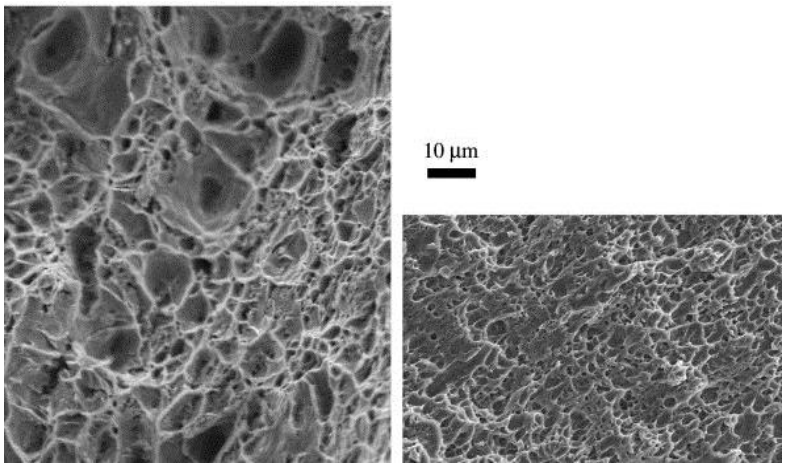

Figure 1. 2 SEM fractographs of ductile fracture in a Weldox 420 showing different rupture mechanisms [28]: (a) necking of intervoid ligaments and (b) intervoid shearing.

In the earlier micro-mechanics constitutive models, the void nucleation, growth and coalescence mechanism was described in details, but the mechanism of the shear-induced damage was not accounted for. These models are not applicable for modeling

fracture under low stress triaxiality where void growth is limited and shear deformations dominates. This motivated a number of recent modifications to include shear-induced damage in the model.

The theoretical study of void damage under shear loading for ductile fracture can be traced back to early 1960s. McClintock [35] studied the void rotation and distortion under simple shear loading, and found that the ligament of voids could be reduced, hence the reduction of effective loading area. This didn't attract much attention until Xue [36] implemented this idea to account for the shear induced damage in his extended Gurson-type model. On the other hand, Nahshon and Hutchinson [37] proposed the shear damage law in a phenomenological way and assumed shear damage varied linearly with the porosity and the effective strain increment. In both Xue and Nahshon-Hutchinson models, the original form of the GTN model was maintained and the void volume fraction in the model was treated as a generalized damage parameter including a void growth contribution and a shear-induced damage contribution. And both assumed that the shear-induced damage was a function of the Lode angle. These modifications have shown improvement in predicting shear dominant failure under low triaxiality conditions. However, these models tended to overestimate in the cases of moderate to high triaxiality. Nielsen and Tvergaard [38] recognized this problem and had to introduce an ad hoc modification to the shear damage evolution law to reduce the shear damage under high triaxiality.

The modeling of shear-induced damage is still being explored by many researches. This thesis also presented a new model to account for shear-induced damage based on Gurson-type models, as described in Chapter 5.

1.3 Residual stress effect on fracture

Residual stresses in the engineering structures are generated from forming, welding, heat treatment etc., which play an important role in either increasing or decreasing the fracture resistance. The compressive residual stress usually improves the fracture toughness, while the tensile residual stress can detrimentally reduce the loading capacity of the structure. This is usually attributed to the additional crack driving force and change of the crack front constraint [39, 40]. As part of the investigation on ductile fracture behaviors, this thesis studied the application of the fracture models to specimens under residual stress.

To quantify the effect of residual stress on fracture toughness, it is necessary to introduce well characterized and reproducible residual stress fields into fracture specimens. There are plenty of literatures on residual stress generation techniques, which can either be mechanical or thermal process. Almer et al. [41] deformed large tensile specimens and cut the gauge sections to produce compact tension (CT) specimens. Meith et al. [42] applied local compression to the sides of fracture specimens. Because of the strain incompatibility between elastic and plastic region caused by the permanent plastic deformation, the residual stress field can be generated in the specimen. This local out-of-plane compression (LOPC) approach was further explored by Mahmoudi et al.[43], who ran a series experiments and finite element analyses to examine how the position of compression tools influences the residual stress distribution in the specimen.

This thesis work employed the LOPC approach and used two pairs of compression punches to generate various residual stress fields in C(T) specimens. The

residual stress field was obtained by conducting finite element simulation of the out-of-plane compression process. After the residual stress field was generated, fracture tests of C(T) specimens having positive and negative residual stresses were conducted and simulated numerically.

1.4 Research objectives and thesis outline

This thesis explored different aspects of ductile fracture modeling. The objective of the research is to investigate and develop valid numerical approaches for ductile damage modeling under complex loading conditions. Both empirical damage initiation criteria and micro-mechanics based models are studied and verified with experiments.

The following lists the different aspects of the research objectives to be achieved through this thesis work:

1) Study the effects of strain rate and temperature on flow stress and ductile failure strain, and investigate the applicability of Johnson-Cook plasticity model and Johnson-Cook damage model for aluminum alloys.
2) Study the Lode angle effect on material plasticity behavior and fracture behaviors with a *J2-J3* plasticity model and the Xue-Wierzbicki fracture model.
3) Calibrate the above models, and study the residual stress effect on ductile fracture resistance for an aluminum alloy.
4) Extend the Gurson-type model to account for shear-induced damage and use it to study the fracture behavior of a Zircaloy.

Here is a simple outline of the thesis framework:

Chapter 1 is a general introduction. It reviews the background of ductile modeling that motivated this research.

Chapter 2 provides an overview of common modeling approaches for ductile fracture study.

Chapter 3 studies the effects of triaxiality, strain rate and temperature on both flow and ductile fracture behavior for three aluminum alloys (5083-H116, 6082-T6 and 5183 weld metal) with a series of axisymmetric tensile specimens, and investigate the applicability of Johnson-Cook plasticity model and Johnson-Cook damage model for these materials.

Chapter 4 studies the effects of the Lode angle on the flow and ductile fracture behaviors for aluminum alloy 5083-H116 through tests on plane strain specimens and torsion specimens, and implements Xue-Wierzbicki fracture model to model the residual stress effect on fracture behavior. A local out-of-plane compression approach was employed to generate residual stress fields in the compact tension specimens.

Chapter 5 builds a new extended GTN model and compares with the existing models. A calibration procedure is provided and used to simulate the crack initiation and growth for a beta-treated zircaloy-4.

Chapter 6 concludes the research, and starts an extended model for future work attempts.

CHAPTER II

DUCTILE FRACTURE MODELING APPROACHES

There is great amount of theoretical research about ductile fracture. A brief literature review is given in this chapter on common modeling approaches. For convenience, a short description of stress tensor and its invariants is presented as a prior.

2.1 Stress tensor and its invariants

Let σ_{ij} be the stress tensor and σ_1, σ_2 and σ_3 be the principal stress values. I_1 represents the first invariant of the stress tensor and the summation convention is adopted for repeated indices. The hydrostatic stress (or mean stress) can be expressed as

$$\sigma_h = \frac{1}{3} I_1 = \frac{1}{3}\sigma_{ii} = \frac{1}{3}(\sigma_1 + \sigma_2 + \sigma_3) \tag{2. 1}$$

Let σ'_{ij} be the stress deviator tensor and σ'_1, σ'_2 and σ'_3 be its principal values, i.e.

$$\sigma'_{ij} = \sigma_{ij} - \sigma_h \delta_{ij} \tag{2. 2}$$

where δ_{ij} represents the Kronecker delta. It is obvious that the first invariant of the stress deviator tensor is zero. The second and third invariants of the stress deviator tensor are defined as

$$J_2 = \frac{1}{2}\sigma'_{ij}\sigma'_{ji} = -(\sigma'_1\sigma'_2 + \sigma'_2\sigma'_3 + \sigma'_3\sigma'_1)$$
$$= \frac{1}{6}\left[(\sigma_1 - \sigma_2)^2 + (\sigma_2 - \sigma_3)^2 + (\sigma_3 - \sigma_1)^2\right] \quad (2.3)$$
$$J_3 = \det(\sigma'_{ij}) = \frac{1}{3}\sigma'_{ij}\sigma'_{jk}\sigma'_{ki} = \sigma'_1\sigma'_2\sigma'_3$$

The von Mises equivalent stress is related to the second invariant of stress deviator tensor as

$$\sigma_e = \sqrt{3J_2} \quad (2.4)$$

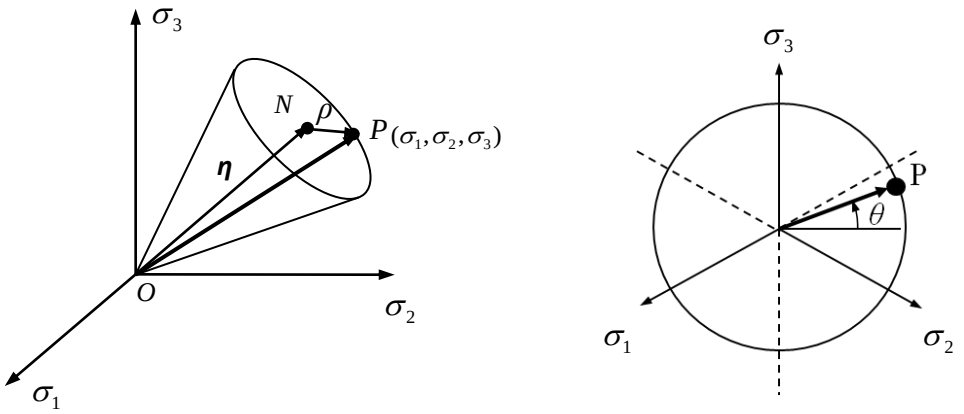

(a) (b)

Figure 2. 1 The stress state represented in (a) principal stress space, (b) the deviatoric plane

A principal stress state ($\sigma_1, \sigma_2, \sigma_3$), can be geometrically represented by a vector $\overrightarrow{OP}$ in the Cartesian coordinate system, with the three principal stresses as axes, as shown in Figure 2.1(a). It is also convenient to represent it in the Haigh–Westergaard cylindrical coordinates (η, ρ, θ), where η, ρ are simply the magnitude of, respectively, the hydrostatic stress vector $\overrightarrow{ON}$ and the deviatoric stress vector $\overrightarrow{NP}$ as shown in Figure

2.1(a). The azimuth angle can be characterized by the Lode angle θ in the deviatoric plane as shown in Figure 2.1 (b).

Stress components in the cylindrical coordinate system can be related to the principle stresses and their invariants as below

$$\begin{aligned} &\eta = \sigma_h \sqrt{3} = I_1 / \sqrt{3} \\ &\rho = \sqrt{2J_2} \\ &\theta = \tan^{-1}\left\{\frac{1}{\sqrt{3}}\left[2\left(\frac{\sigma_2 - \sigma_3}{\sigma_1 - \sigma_3}\right) - 1\right]\right\}, \text{ or } \cos\left(3\theta + \frac{\pi}{2}\right) = \frac{3\sqrt{3}J_3}{2J_2^{3/2}} = \xi \end{aligned} \tag{2. 5}$$

There are many equivalent definitions to lode angle in literatures, some of them use the same name 'Lode parameter', such as 'ξ' in the above equation, Bai and Wierzbicki[44]. Barsoum and Faleskog [32] defined another Lode parameter μ as

$$\mu = \frac{2\sigma_2 - \sigma_1 - \sigma_3}{\sigma_1 - \sigma_3} \tag{2. 6}$$

This parameter can be easily related to the Lode angle with

$$\tan\theta = \frac{\mu}{\sqrt{3}} \tag{2. 7}$$

Stress triaxiality is defined as the ratio of the hydrostatic stress (or mean stress) over the von Mises equivalent stress,

$$T^* = \sigma_h / \sigma_e = \sqrt{2}\eta / (3\rho) \tag{2. 8}$$

It can be observed that, when von Mises equivalent stress is known, the stress state is fully defined by two nondimensional parameter, stress triaxiality and Lode angle or Lode parameter.

2.2 Common modeling approach for ductile fracture

The ductile fracture models can be divided into three main categories:

i). Non-weakening fracture initiation criterion. This type of fracture models do not account for material damage induced weakening effect. The advantages of these models are: 1) it's easy to calibrate material parameters with experimental data, due to the decoupling of material response and damage prior to failure, 2) numerical implementation is also easier for finite element application.

ii). Continuum damage models. In this type of models, damage is coupled with the plastic behavior. It treats the effect of damage in a purely phenomenological way, and do not explicitly describe the details in the microstructure. It is based on the idea that the actual sustainable stress level in the material increases due to reduction of the effective loading area resulted from microcracks and microvoids. This method avoids complex micro features, and treats material behaviors in a macroscopic sense.

iii). Micro-mechanics based model. The micro-mechanics based models monitor the micro scale features, mainly the void, in a phenomenological way, and can replicate the process of nucleation, growth and coalescence. Most of the micro mechanical models are the Gurson-type models, constructed as a yield function that incorporates the void growth mechanism and the void induced material softening.

2.2.1 Fracture initiation criterion (Non-weakening)

In this type of damage models, a damage parameter *D* is usually defined to indicate the extent of material deterioration but has no influence on material constitutive behavior prior to fracture.

A common definition of damage *D* is based on accumulated plastic strain, which is calculated from the integral of equivalent plastic strain $\bar{\varepsilon}^p$ factored by a weight function *f* :

$$D = \int_0^{\bar{\varepsilon}^p} f\left(\sigma_{ij}, \bar{\varepsilon}^p, \dot{\bar{\varepsilon}}^p, T, ...\right) d\bar{\varepsilon}^p \tag{2. 9}$$

The weight function *f* can be related to macro-scale field variables, such as stress state σ_{ij}, equivalent plastic strain $\bar{\varepsilon}^p$, equivalent plastic strain rate $\dot{\bar{\varepsilon}}^p$ and temperature *T*, etc, as shown in Eq. (2.9).

When the accumulated damage reaches a critical value, failure occurs. This critical value can be used to normalize the damage calculation, and gives a unit value for damage at fracture initiation.

Assuming damage accumulates linearly with equivalent plastic strain under fixed loading conditions (stress component ratio, strain rate, temperature, etc), a simple form of damage can be defined as

$$D = \frac{\bar{\varepsilon}^p}{\varepsilon_f} \tag{2. 10}$$

where ε_f is the effective failure strain at given loading conditions.

When the loading condition is not constant, damage can be defined as the integral of equivalent plastic strain $\bar{\varepsilon}^p$ weighted by the reciprocal of the effective failure strain,

$$D = \int_0^{\bar{\varepsilon}^p} \frac{d\bar{\varepsilon}^p}{\varepsilon_f(\sigma_{ij}, \dot{\bar{\varepsilon}}^p, T, ...)} \tag{2. 11}$$

A widely used damage model is given by Johnson and Cook [17], where they define ε_f as

$$\varepsilon_f = \left[D_1 + D_2 \exp(D_3 T^*)\right]\left[1 + D_4 \log\frac{\dot{\bar{\varepsilon}}^p}{\dot{\bar{\varepsilon}}_0^p}\right]\left[1 + D_5 \frac{T - T_0}{T_{melt} - T_0}\right] \tag{2. 12}$$

The first term, originated from Hancock [16], describes the stress triaxiality dependency of the failure strain. This represents the stress state effect with only one parameter, T^*. The second and third term defines the effect of equivalent plastic strain rate and temperature respectively, where $\dot{\bar{\varepsilon}}_0^p$ is a reference plastic strain rate, T_0 and T_{melt} are the room temperature and the melting temperature. D_1, D_2, D_3, D_4 and D_5 are five material constants.

The Johnson-Cook fracture model is usually combined with the Johnson and Cook constitutive model [45], where its yield stress $\bar{\sigma}$ is defined as:

$$\bar{\sigma} = \left[A + B\varepsilon_p^n\right]\left[1 + C\log\frac{\dot{\bar{\varepsilon}}^p}{\dot{\bar{\varepsilon}}_0^p}\right]\left[1 - \left(\frac{T - T_0}{T_{melt} - T_0}\right)^q\right] \tag{2. 13}$$

where *A*, *B*, *n*, *C*, and *q* are five material constants. The first term of the right hand side in Eq. (2.13) represents the quasi-static stress-strain relation at room temperature; the second term indicates strain-rate hardening; the third term gives the temperature softening effect.

The effects of stress state, strain rate and temperature on failure strain are assumed to be independent, to make the model easier to calibrate. For quasi-static loading under room temperature, only stress state dependency is in effect. Due to its simple form and broad consideration, the Johnson-Cook fracture model is very popular for industrial applications.

The stress state dependency of failure strain, for quasi-static loading under room temperature, has been studied by many researchers. Wierzbicki [46] calibrated seven different damage initiation criteria for 2024-T351 aluminum alloy under a wide range of the stress triaxiality values. Facture loci of these calibrated models were plotted together against experiment data for comparison. Among these models, the Xue-Wierzbicki model gave the best prediction. The Xue-Wierzbicki model defined the effective failure strain as a function of both triaxiality and lode parameter:

$$\varepsilon_f(T^*,\xi) = \varepsilon_f^{\xi=1}(T^*) - (\varepsilon_f^{\xi=1}(T^*) - \varepsilon_f^{\xi=0}(T^*))[1-(1-|\xi|^n)^{1/n}] \qquad (2.14)$$

where $\varepsilon_f^{\xi=1} = C_1 e^{-C_2 T^*}$ and $\varepsilon_f^{\xi=0} = C_3 e^{-C_4 T^*}$ correspond to the fracture strain for two limiting cases, axisymmetric tension loading (ξ =1) and plane strain and pure shear loading (ξ = 0) respectively. C_1, C_2, C_3, C_4 and n are five parameters need to be calibrated.

There are many other common damage initiation criteria, such as Cockcroft–Latham criteria [47], Wilkins' criteria [48], etc. Wilkins' model does not explicitly introduce the concept of failure strain, but it can be converted to a similar form to Eq. (2.11) [21]. For all this type of models, the non-weakening/uncoupled assumption makes them suitable to be integrated with a plasticity model without much difficulty. Moreover, it even allows multiple fracture criteria to be used for a single material, such as the case in commercial codes ABAQUS [49].

For prediction of fracture initiation in crack-free bodies, since damage induced material softening usually does not play an important role until it's close to final fracture for many ductile materials, the error induced by the uncoupled assumption is not too bad [50]. However, for modeling of crack propagation, the softening of a material point significantly affects the surrounding stress field and the final results, and the uncoupled assumption is not persuasive enough. Furthermore, instant failure after fracture initiation will lead to dynamic instability due to the sudden drop of stress state at the material point.

As a remedy, a post-initiation softening behavior can be defined as a complement to the fracture initiation law. Once fracture initiation criterion is satisfied, the material stiffness is degraded progressively according to the specified degradation law. This methodology was adopted by ABAQUS [49] and Li [51].

2.2.2 Continuum damage mechanics

The first continuum damage mechanics model was developed by Kachanov [51], and further extended by Lemaitre [50, 52]. In their works, the damage variable D represents the reduction of the effective loading area resulted from micro voids and

cracks. Assuming isotropic damage, the actual stress the matrix material undergoes is defined as the applied stress σ_e divided by (1-*D*):

$$\sigma_M = \frac{\sigma_e}{1-D} \tag{2. 15}$$

The yield function is modified accordingly

$$F = \sigma_M - \sigma_y = \frac{\sigma_{eq}}{1-D} - \sigma_y \tag{2. 16}$$

where σ_y is the yield stress.

The damage evolution laws in continuum damage mechanics were usually derived through a thermodynamic framework [52], or by introducing the weakening effect into the uncoupled damage model. For instance, Borvik et al [18] introduced a weakening factor to the Johnson-Cook strength equation

$$\sigma_e = \left(1-\beta_b D\right)\left[A + B\varepsilon_p^n\right]\left[1 + C\log\frac{\dot{\bar{\varepsilon}}^p}{\dot{\bar{\varepsilon}}_0^p}\right]\left[1-\left(\frac{T-T_0}{T_{melt}-T_0}\right)^q\right] \tag{2. 17}$$

where *D* is the same as in the original Johnson-Cook damage model, and β_b defines the material softening. Similarly, Xue [21] used an exponential term D^β to account for the weakening effect:

$$\sigma_e = \left(1-D^\beta\right)\sigma_M \tag{2. 18}$$

2.2.3 Micro-mechanical models

The pioneer work by McClintock [13] and Rice and Tracey [14] on growth of cylindrical and spherical voids in infinitely large, plastic solids studied the major influencing factors in the fracture process, and indicated that it is possible to develop mechanism-based, micromechanical models to describe the complex ductile failure process. Since then tremendous efforts have been made in building micromechanical fracture models. Gurson [15] proposed a homogenized yield surface for void-containing materials based on the maximum plastic work principle. Rousselier [53] described the mechanical behavior of voided materials using thermodynamic and plastic potentials.

More recent efforts on this area have focused on extending/modifying these models to develop computational schemes that simulate the ductile fracture process under various circumstances. Tvergaard [54, 55] introduced two adjustment parameters into the Gurson model to account for the effect of void interaction and material strain hardening. Chu and Needleman [56] proposed void nucleation models controlled by the local stress or plastic strain. Tvergaard and Needleman [57] introduced a simplified method to provide for rapid deterioration of stiffness after localization has occurred in the material. Koplik and Needleman [58] proposed a unit cell approach to calibrate the micromechanical parameters of the homogenized model.

1) GTN model

The Gurson model, with additional developments by Tvergaard and Needleman, is often referred as the GTN model and has been widely used to describe the material

behavior during the ductile fracture process. The yield function of GTN model takes the following form

$$\Phi = \left(\frac{\sigma_e}{\sigma_M}\right)^2 + 2q_1 f \cosh\left(\frac{q_2}{2}\frac{\sigma_{kk}}{\sigma_M}\right) - 1 - \left(q_1 f\right)^2 = 0 \tag{2. 19}$$

where: f is the current void volume fraction; σ_e is the macroscopic effective stress; σ_{kk} is the hydrostatic stress; and σ_M is the current yield stress of the matrix material. The adjustment parameters q_1 and q_2 were introduced by Tvergaard [54, 55] to improve model predictions.

The plastic strain rate is defined as

$$\dot{\varepsilon}_{ij}^{p} = \dot{\lambda} n_{ij} \tag{2. 20}$$

where $\dot{\lambda}$ is the plastic multiplier and the associated (normality) flow rule is invoked to define the normal of the plastic strain rate, *i.e.*, $n_{ij} = \frac{\partial \Phi}{\partial \sigma_{ij}}$.

The evolution of the void volume fraction is due to two contributions, void growth and void nucleation.

$$\dot{f} = \dot{f}_g + \dot{f}_n, \tag{2. 21}$$

Void growth is based on bulk material incompressibility under plastic deformation

$$\dot{f}_g = \left(1 - f\right)\dot{\varepsilon}_{kk}^{p}, \tag{2. 22}$$

where $\dot{\varepsilon}_{kk}^{p}$ represents the first invariant of the plastic strain rate.

Void nucleation can be stress or strain controlled. A commonly used strain-controlled void nucleation law is taken to follow a normal distribution as suggested by Chu and Needleman [56]

$$\dot{f}_n = A_N \dot{\varepsilon}_M^p , \quad A_N = \frac{F_n}{S_n \sqrt{2\pi}} \exp\left[-\frac{1}{2}\left(\frac{\varepsilon_M^p - \varepsilon_n}{S_n} \right)^2 \right] , \tag{2. 23}$$

where ε_M^p represents the matrix plastic strain, and F_n, ε_n and S_n are material parameters.

In the GTN model, the effect of rapid void coalescence after the onset of localization is taken into account by replacing f in Eq. (2.19) with an effective porosity f^* defined by the following bilinear function

$$f^* = \begin{cases} f & \text{for } f \le f_c \\ f_c + \dfrac{1/q_1 - f_c}{f_f - f_c}(f - f_c) & \text{for } f_c \le f \le f_f \end{cases} \tag{2. 24}$$

where f_c is the critical void volume fraction at which void coalescence begins and the material softening is accelerated thereafter. Another material constant is the void volume fraction cutoff at failure f_f . As f reaches f_f , f^* increases to $1/q_1$ and the material loses all stress carrying capacity.

By enforcing equality between the rates of macroscopic plastic work and the matrix plastic dissipation, the matrix yield stress, σ_M , and the matrix plastic strain rate, $\dot{\varepsilon}_M^p$, are coupled through

$$\sigma_M \dot{\varepsilon}_M^p = (1-f)\sigma_{ij}\dot{\varepsilon}_{ij}^p \tag{2. 25}$$

where the matrix material follows a prescribed hardening function $\sigma_M(\varepsilon_M^p)$.

2) Modified GTN model with shear damage

Despite the apparent success and popularity of the GTN model in predicting ductile fracture, it still suffers from several significant limitations. A major drawback of the GTN model is its inapplicability to model the localization and fracture under low stress triaxiality, shear dominated deformations, since it does not predict void growth and damage under shear loading. This motivated a number of recent modifications to include shear-induced damage in the model, among which the work by Xue [36] and Nahshon and Hutchinson [37] received the most attention.

In these modifications, the void volume fraction as appeared in Eq. (2.19) is replaced by a general damage parameter containing contributions of both volumetric damage and shear damage while the form of the GTN yield function is retained.

Nahshon and Hutchinson claimed that *f* is no longer directly tied to the plastic volume change but rather should be regarded as a damage parameter, and introduced an additional term in the evolution equation of *f* to account for shear damage. Xue directly introduced a new damage parameter, *D*, which contains both void damage and shear induced damage, and substituted the $q_1 f$ term in Eq. (2.19) with *D*. The modified yield function can be expressed as

$$\Phi = \left(\frac{\sigma_e}{\sigma_M} \right)^2 + 2D\cosh\left(\frac{q_2}{2} \frac{\sigma_{kk}}{\sigma_M} \right) - 1 - D^2 = 0, \tag{2. 26}$$

In establishing shear damage evolution law, both Xue [36] and Nahshon and Hutchinson [37] first derived the evolution of shear damage under the pure shear or simple shear state, then extended it to other stress states by introducing a Lode angle dependent function. Nahshon and Hutchinson proposed the shear damage law in a phenomenological way which assumes it linearly depends on the porosity and the effective strain increment. Inspired by the solution for coalescence of holes in a shear band by McClintock et al. [59], Xue developed his shear damage law based on the change of the void ligament of a unit cell model under simple shear deformation. The damage evolution law can be summarized as follows, where (2.27a) represents the Nahshon and Hutchinson model and (2.27b) represents Xue's model, and (2.27c) show Lode angle dependent functions

$$\dot{f} = \dot{f}_g + \dot{f}_n + \dot{f}_s, \quad \dot{f}_s = k_\omega f \omega(\sigma_{ij}) \frac{\sigma_{ij} \dot{\varepsilon}_{ij}^p}{\sigma_e}, \tag{2.27a}$$

$$\dot{D} = q_1 \left(\dot{f}_g + \dot{f}_n \right) + \dot{D}_s, \quad \dot{D}_s = q_3 f^{q_4} g(\theta) \varepsilon_M^p \dot{\varepsilon}_M^p, \tag{2.27b}$$

$$\omega(\sigma_{ij}) = 1 - \left[\cos(3\theta + \pi/2) \right]^2, \quad g(\theta) = 1 - \frac{6|\theta|}{\pi}, \tag{2.27c}$$

The shear damage evolution laws of both models share three common features. First, shear damage is a weighted integration of equivalent plastic strain increment (the fraction in the Nahshon and Hutchinson model can be regarded as a definition of the equivalent plastic strain increment). Second, the Lode angle dependency functions,

$\omega(\sigma_{ij})$ and $g(\theta)$, have the same limit values. It equals to one at the generalized shear (pure shear state + hydrostatic state) and zero at the generalized tension/compression (uniaxial tension/compression + hydrostatic state). Third, one material parameter, k_ω or q_3, is used to scale the shear damage growth rate. This parameter can be calibrated using experimental data obtained from a shear dominated test.

The major difference between the two models is the void volume dependency. There is an additional parameter q_4 in Xue's model, where shear damage is scaled by f^{q_4}. The value of q_4 is 1/2 for 2D problem and 1/3 for 3D problem. This parameter has a significant effect on the predicted shear damage since porosity f can vary significantly during the loading history.

Since the model has one generalized damage parameter in Eq. (2.26), the onset of localization and the final material failure process can be modeled by introducing a D^* in a similar fashion as the f^* concept described in Eq. (2.24).

3) Other extensions of the Gurson-type model

The Gurson-type was extended by Gologanu et al. [60, 61] to consider spheroidal voids. In the so called GLD model, both void volume fraction and the void shape evolve as deformation increased. The spheroidal model was further extended by Scheyvaerts et. [34], to include the effect of void rotation. The prediction of the extended model agreed with the 3D cell model study, and captured the effect of the initial void shape and orientation on the void rotation rate.

Thomason [62] developed a coalescence model based on the mechanism of internal necking, and did not introduce any extra parameters. The coalescence model was later implemented by Pardoen and Hutchinson [63], Zhang, et. [64].

Many researchers also studied the application of Gurson-type model for various types of matrix material with features such as: anisotropy [65, 66] and kinematic hardening [67, 68], stress state dependent plasticity [69]. Materials with heterogeneous microstructures has also been studied by many authors [70-72].

CHAPTER III

MODELING OF FRACTURE INITIATION: TEMPERATURE, STRAIN RATE AND TRIAXIALITY EFFECT

In ductile fracture modeling with failure initiation criteria described in section 2.1.1, the key is to find the failure strain under different loading conditions. In order to calculate the failure strain, the plastic flow behavior of the material needs to be accurately captured in the plasticity model.

This chapter presents an experimental and numerical study to investigate the effects of strain rate and temperature on flow stress and ductile failure strain of three aluminum alloys, a 5083-H116, a 6082-T6 and a 5183 weld metal. In addition, the effect of the stress triaxiality on ductile failure strain was also studied. With the experimental data obtained, the applicability of the Johnson-Cook plasticity and ductile fracture models was examined. The plasticity model was assumed to be uncoupled with damage model for simplicity.

The chapter is organized as follows. Section 3.1 provides information about the materials and experimental procedures. Section 3.2 gives the plastic flow behavior of the materials under different loading conditions. Section 3.3 presents the fracture properties of materials and all the numerical results. And finally, Section 3.4 summarizes the major findings.

3.1 Materials and Experiments

Table 3.1 Chemical compositions (wt %)

	5083-H116	6082-T6	5183 weld metal
Al	Balance	Balance	Balance
Si	0.20	1.01	0.40
Fe	0.35	0.31	0.40
Cu	0.052	0.09	0.10
Mn	0.69	0.40	0.5~1.0
Mg	4.41	0.61	4.3~5.2
Cr	0.086	0.02	0.05~0.25
Zn	0.081	0.02	0.25
Ti	0.065	0.03	0.15

Aluminum alloys, because of their light weight, good mechanical properties and corrosion resistance, provide a viable replacement for steels in many engineering structures. These structures may be subjected to dynamic loading and experience varying temperature. Understanding the effects of strain rate and temperature on the plastic flow and ductility properties of these aluminum alloys is crucial to structural reliability assessments.

The aluminum alloys of interest were 5083-H116 (a work-hardened marine alloy), 6082-T6 (a precipitation hardened marine alloy), and welded joint of 5183 filler joining two 5083-H116 plates. 5083-H116 was procured in 25 mm thick rolled plate that was 1.2 m wide by 3.6 m long to ASTM B928-04a from the Belaya Kalitva Metallurgical Products Company while 6082-T6 was procured in 25 mm thick by 0.2 m wide by 3.6 m

long flat bars to ASTM B221 from Taber Extrusion, LLC. Base metal specimens were extracted from the center of the plate thickness in the transverse orientation, relative to the rolling direction. Chemical compositions of the three aluminum alloys are presented in Table 3.1. These materials were considered because they are the most often used aluminum alloys in marine structures. The test matrix included smooth and notched round tensile specimens. The diameter of the gage section of the smooth round bar was 6.35 mm. Notched round tensile specimens impart higher stress triaxiality to the material in the gage section than the uniform tensile specimens. All the notched round bars had the same diameters of 15.2 mm in the smooth sections and 7.62 mm at the root of the notch so that the specimens sampled the same amount of material. Three notch radii, 1.27 mm, 2.54 mm and 6.35 mm, were considered for specimens D, B and E respectively. As the notch radius decreases, the stress triaxiality increases. Notched round bar tensile tests in the B-notch and E-notch configurations were conducted on the 5083-H116 base metal, 6082-T6 base metal, and 5183 weld metal. The D-notch specimens were tested only for the 5083-H116 base metal. A 25 mm extensometer was centered about the gage section for each specimen and measured a global extension of the notched gage section.

Table 3.2 Test conditions

	5083-H116	6082-T6	5183 weld metal
Temperature	24, 66, 149	24, 66, 149	24, 66, 149
Strain rate level	1, 2, 3	1, 3	1, 3
Notch	B,E,D	B,E	B,E

All test conditions are listed in Table 3.2. Smooth round tensile specimens were tested at room temperature (24 ℃) and two elevated temperatures (66 ℃ and 149 ℃),

and under different dynamic loading rates. Because 5083-H116 gains its strength from the work-hardening described by the H116 condition, the testing temperature of 149 ℃ was selected as the upper temperature for calibrating the thermal softening relation as it is safely below the hot-working temperature of 316 ℃. Quasi-static (Level 1, 0.004 ~ 0.006 s^{-1}) and high rate tests (Level 3, 150~220 s^{-1}) were conducted for all three materials, and medium rate tests (Level 2, 0.15~0.70 s^{-1}) for 5083-H116 only. Notched round tensile specimens were only tested at room temperature (24 ℃) under quasi-static loading.

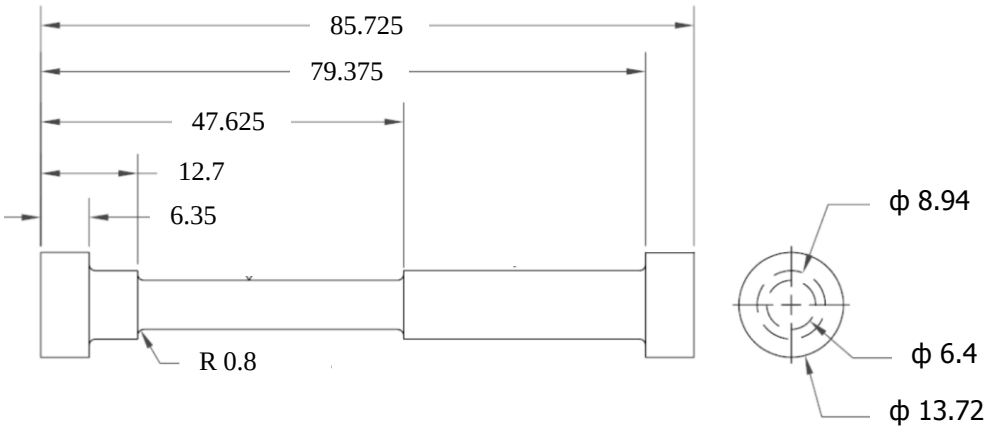

Figure 3. 1 Schematic of dynamic, uniform tensile specimen (dimensions in mm).

Figure 3.1 illustrates the dynamic specimen design. At highest loading rates, the machine's load cell did not adequately resolve load, nor would an extensometer or diametral gage maintain physical contact with the specimen throughout testing. Instead, the specimen design incorporated a larger diameter region than the gage section that was designed to remain elastic throughout testing. Two strain gages were applied 180° apart to this larger diameter region and wired in a Wheatstone half-bridge circuit to form an integral load cell. The integral load cell was calibrated to 10% of the predicted maximum

load prior to testing and the calibration was extrapolated to full scale. Specimen axial strain measurement was achieved by applying two 3 mm high-elongation strain gages to the gage section of the specimen at 180° apart and also wired in a Wheatstone half-bridge. All the tests were done by NSWCCD (Naval Surface Warfare Center, Carderock Division) and detailed test procedures are provided in paper [73].

3.2 Plastic flow behavior

A number of plasticity models with different function forms have been proposed to describe the strain rate and temperature effects on flow stress, among which the Johnson–Cook plasticity model is widely used because of its simplicity. It assumes the uncoupled behavior of strain hardening, strain rate hardening, and temperature softening effect. In this section, attempts were made to interpret the experimental results with a slightly modified Johnson-Cook plasticity model.

3.2.1 Strain hardening for room temperature (RT), quasi-static (QS) loading

In the original Johnson-Cook plasticity model (2.13), the first bracket at the RHS presents the strain hardening effect under RT and QS. Any other strain hardening law or simple piecewise stress-strain relation can be used instead to improve accuracy. It was found that the stress-strain relation at RT and QS loading could be very well described by a power-law function for all three materials, where the current yield stress is expressed as a power function of the total strain ε

$$\sigma = \sigma_0 \left(\frac{\varepsilon}{\varepsilon_0} \right)^N \qquad \text{when } \sigma > \sigma_0 \tag{3.1}$$

where σ_0 represents the initial yield stress, ε_0 is the initial yield strain and N is the strain hardening exponent. Keeping other portion of the Johnson-Cook plasticity model (Eq. (2.13)) unchanged, the model was modified as

$$\bar{\sigma} = \sigma\left(\bar{\varepsilon}^p\right)\left[1 + C\log\frac{\dot{\bar{\varepsilon}}^p}{\dot{\bar{\varepsilon}}_0^p}\right]\left[1 - \left(\frac{T - T_0}{T_{melt} - T_0}\right)^q\right] \tag{3.2}$$

where $\sigma\left(\bar{\varepsilon}^p\right)$ is the stress-strain relation (strain hardening law) defined through Eq. (3.1).

The strain hardening exponent N was obtained by performing linear regression on the true stress vs. true strain curve before necking. All parameters for the modified Johnson-Cook plasticity model are listed in Table 3.3. Figure 3.2 gives the stress-strain curves at various strain rates at RT for all three materials.

Table 3.3 Calibrated parameters for the modified Johnson-Cook plasticity model

	σ0 (MPa)	N	ε0	C	q
5083-H116	189.6	0.155	0.00277	0.005	NA
6082-T6	288.7	0.064	0.00419	0.0034	1.033
5183 weld metal	113.8	0.238	0.00212	0	NA

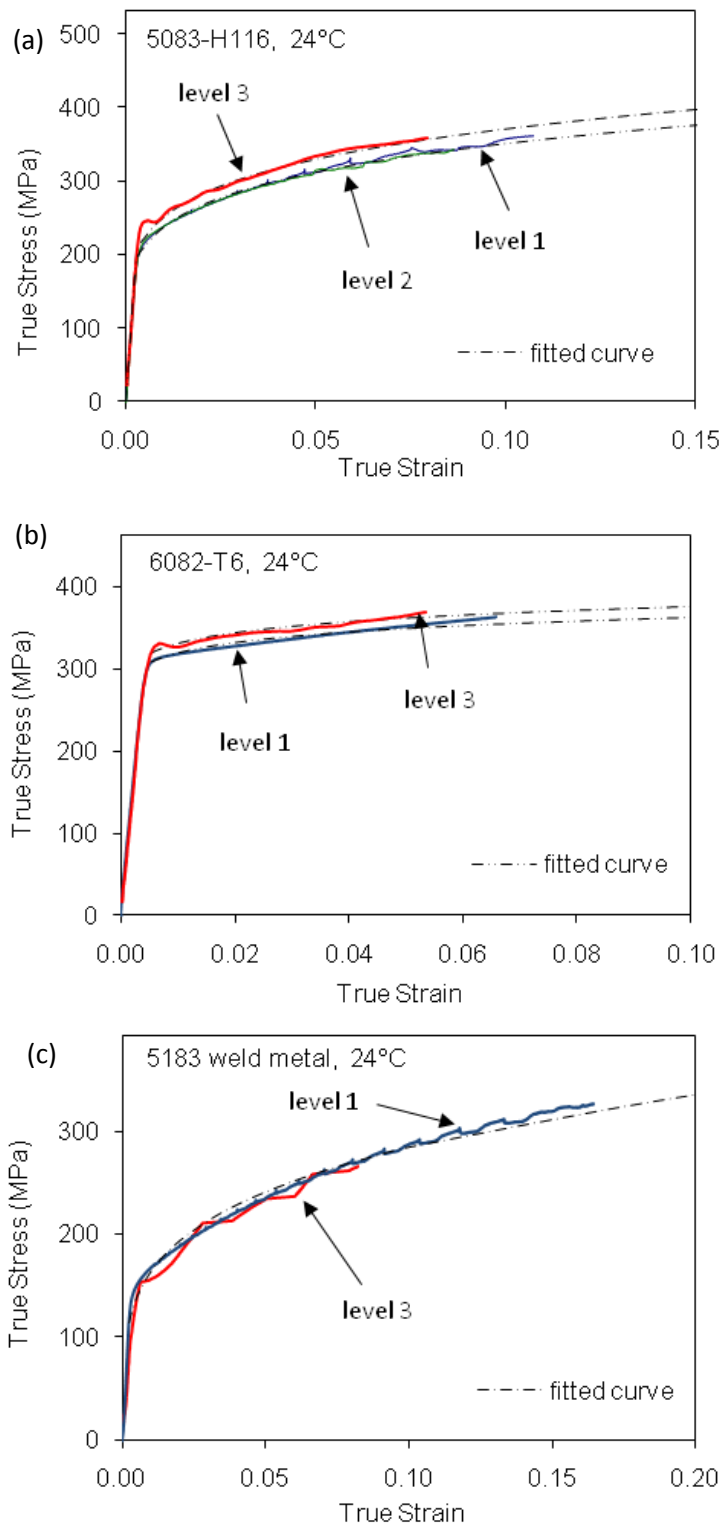

Figure 3. 2 Comparison of the stress-strain relations predicted by the Johnson-Cook model with experimental data at different strain rates: (a) 5083-H116 (b) 6082-T6 and (c) 5183 weld metal.

3.2.2 Strain rate effect on flow stress

As shown in the Figure 3.2(a), the flow stress of 5083-H116 did not exhibit the same strain rate sensitivity in the test strain rate range. At higher rate loading, the specimens displayed rate hardening; however, the difference of stress-strain curves between the medium rate loading and QS loading before necking was quite small, it even displayed noticeable negative strain rate sensitivity after necking, which could be observed clearly from the load-displacement relation shown in Figure 3.8 discussed later.

This unusual feature of rate softening at low stain rates can be explained by the effect of dynamic strain aging (DSA), which exists in most 5XXX series Al-Mg alloy [74]. DSA is introduced when the solute magnesium atoms lock dislocation during dislocation motion at low strain rates and sufficiently high temperature [75], which results in higher strength. As the strain rate increases, the frequency of this interaction will decrease, which results in strain rate softening in the low strain rate range. Another phenomenon indicating the DSA effect is the serration of stress-strain curve, the well-known Portevin-LeChaterlier phenomenon [76], which was observed for both 5083-H116 and 5183 weld metal from Figure 2(a) and (c). However, the 5183 weld metal did not exhibit noticeable strain rate sensitivity in the range considered in this study.

The complex rate sensitivity of the 5XXX alloys suggested that the effect of strain rate on flow stress could not be adequately described by the simple Johnson-Cook like constitutive laws in the range of the loading rate considered in this study. However, for the reason that DSA almost has no effect at high strain rate and since the stress-strain curves at different strain rates had similar shapes, the Johnson-Cook type models might

still be applicable in the high strain rate region. Mukai et al. [77] studied various Al-Mg alloys and found only when the strain rate was beyond 10 s^{-1}, the flow stress would increase with increasing strain rate. Thus we performed calibration for Johnson-Cook model using only high loading rate data and the QS data. Figure 2(a) shows the stress-strain relation predicted by the Johnson-Cook model with C = 0.005 and $\dot{\varepsilon}_p$ = 180 s^{-1} (fitted curve) as well as the experimental curves. It should be emphasized that the Johnson-Cook model cannot predict the plasticity behavior correctly as the strain rate is less than $10s^{-1}$. To quantify the low or negative strain rate sensitivity at the low strain rate region, further studies are required.

Compared to the AA 5XXX series, the 6082-T6 has much less magnesium concentration and no obvious DSA effect was observed in our tests (the stress-strain curves do not show serration). The stress-strain curves of 6082-T6 at high loading rate obtained from five specimens showed considerable scatter. Using the mean of these dynamic stress-strain curves and the QS data, the calibrated C-value was 0.0034. Figure 2(b) gives the stress-strain relation predicted by the Johnson-Cook model with C = 0.0034 and $\dot{\bar{\varepsilon}}^p$ = 190 s^{-1} as well as the experimental curves. The strain rate hardening property of 6082-T6 has been studied by other authors. Chen et al. [78] conducted a series of tests at a wider strain rate range from 10^{-3} to $900s^{-1}$ and found only a slight rate hardening for this material.

If the Johnson-Cook plasticity model is to be used to describe these materials, based on the limited experimental data obtained in this study, the model parameters could be calibrated as listed in Table 3.3.

3.2.3 Temperature effect on flow stress

5083-H116 and 5183 weld metal exhibited similar temperature dependency of flow stress. As can be seen from Figure 3.3(a) and (c), before temperature was raised beyond a certain level, the flow stresses of these materials showed very little variation with temperature. Clausen et al. [74] also observed that the flow stress was not sensitive to temperature in the range of 20 ℃ to 100 ℃ for 5083-H116. As temperature continued to increase, both materials displayed noticeable temperature softening.

Because thermal softening only occured at relatively high temperature, the Johnson-Cook plasticity model would not work in the temperature range considered in this study. By comparing the stress-strain curves at RT and at 149 ℃ for 5183 weld metal, Figure 3.3(c), the initial yield stress did not change much but the 149 ℃ curve showed considerable less strain hardening. For this reason, stress-strain curves obtained at different temperatures for 5083-H116 and 5183 weld metal were used in the input files of the finite element analyses presented in Section 4.4.

Compared to the 5XXX alloys, the temperature softening behavior of 6082-T6 could be very well described by the Johnson-Cook plasticity model at the temperature range considered in this study with a calibrated q-value of 1.033. This is manifested in Figure 3.3(b), where the solid lines represented the stress-strain curves obtained experimentally at 24 ℃, 66 ℃ and 149 ℃ respectively and the three dash-dotted lines represented the corresponding curves given by the Johnson-Cook plasticity model using the calibrated parameters.

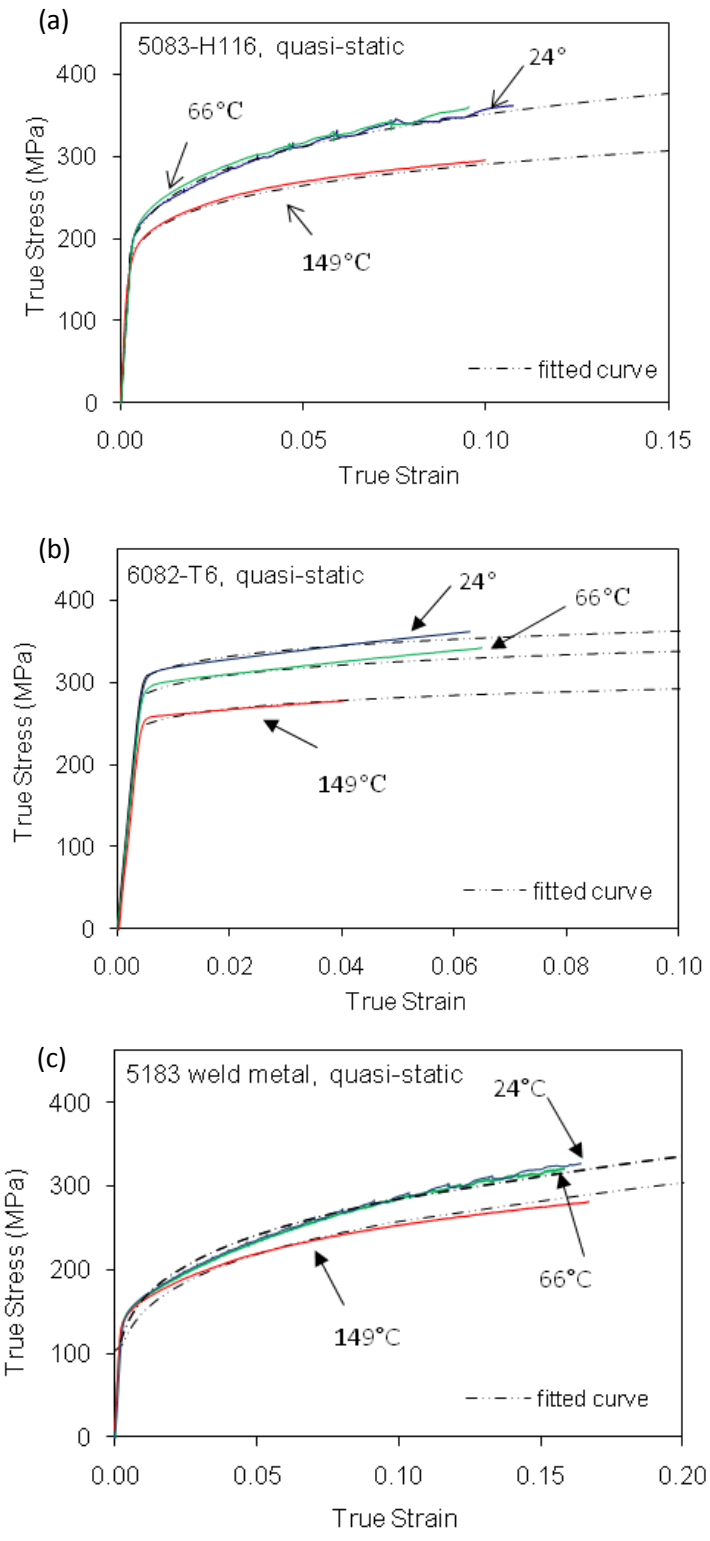

Figure 3. 3 Comparison of the stress-strains relation predicted by the Johnson-Cook model with experimental data at different temperatures: (a) 5083-H116 (b) 6082-T6 and (c) 5183 weld metal.

3.3 Fracture behavior and numerical results

The Johnson–Cook fracture model, which is widely used in structural reliability analysis, provides a simple mathematical relation to describe the effects of stress triaxiality, strain rate and temperature on the equivalent strain to ductile fracture. In this section, the fracture behavior of materials was studied, and the fracture model was calibrated through both experimental data and numerical results.

In the calibration of the fracture model, the effective failure strain needed to be determined for each loading case. A common method to get equivalent failure strain is by measuring the area reduction of round tensile specimen [74]. This method is an approximate method for the reason that the plastic flow becomes inhomogeneous after necking, which results in non-uniform strain distribution on the fracture surface. In this thesis, an inverse method was employed to obtain the local failure strain: by comparing the finite element simulated loading history with the experimental record, the equivalent strain at critical element when the failure initiated was extracted.

3.3.1 Finite element modeling and Fracture criterion

Finite element analyses of the specimens were conducted to study the fracture behavior of the materials using the software package ABAQUS [79]. For round tensile specimens, axi-symmetric conditions were considered and the 4-node, axisymmetric, solid elements with reduced integration (CAX4R) were used. Details of the finite element models, mesh refinement and convergence studies can be found in Gao et al. [80].

The Johnson-Cook fracture model is restated here for convenience

$$D = \int_0^{\bar{\varepsilon}^p} \frac{d\bar{\varepsilon}^p}{\varepsilon_f(T^*, \dot{\bar{\varepsilon}}^p, T)} \tag{3.3a}$$

$$\varepsilon_f = \left[D_1 + D_2 \exp(D_3 T^*)\right]\left[1 + D_4 \log\frac{\dot{\bar{\varepsilon}}^p}{\dot{\bar{\varepsilon}}_0^p}\right]\left[1 + D_5 \frac{T - T_0}{T_{melt} - T_0}\right] \tag{3.3b}$$

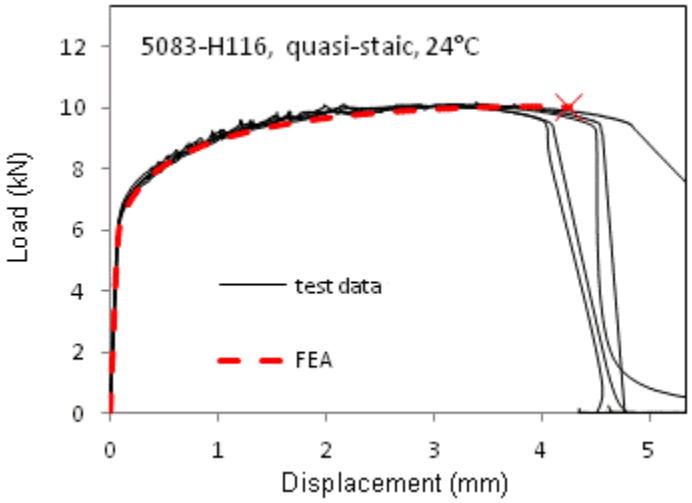

Figure 3. 4 Comparison of the numerically predicted and measured load-displacement response for the smooth tensile bars at RT and QS loading rate.

The damage parameter *D* defined in Eq. (3.3a) accounts for the history effect when the stress triaxiality, strain rate and temperature do not remain constant. For all the specimens in this study, fracture started at the specimen center. Therefore, the history of stress triaxiality, plastic strain rate and equivalent strain increment of the center element were output to compute *D*. The sudden load drop on the measured load-displacement curve designated fracture initiation. By comparing the computed and measured load-displacement curves, the increment numbers at which the center element fractured were

determined. Figure 3.4 compares the predicted load-displacement curve with test data for 5083-H116 for the smooth tensile bar at RT and QS loading rate, where the "red cross" indicates the average failure position.

3.3.2 Triaxiality effect on failure strain

As described in the Johnson-Cook fracture model, the triaxiality-dependent, rate-dependent and temperature-dependent terms in Eq. (3.2) are not coupled, thus the calibrations of the parameters D_1 to D_5 were performed separately. We first calibrated the parameters D_1 to D_3 using the room temperature, QS data.

Figure 3.5 compares the predicted load-displacement curves with experimental records for the notched round bars, where the solid black lines represent the experimental measurements and the dashed red lines represent the numerical predictions. In general, the numerical results matched the experimental records very well.

A nonlinear optimization process was employed to determine parameters D_1 to D_3, where an optimization function was chosen as to minimize the difference between the average of the computed damage values and one

$$\min_{(D_1,D_2,D_3)}\left(Error\right)=\min_{(D_1,D_2,D_3)}\frac{1}{M}\sum_{i=1}^{M}\left[1-D_f^{(i)}\right]^2 \tag{3.4}$$

where M is the number of specimens and $D_f^{(i)}$ is the computed damage parameter value for specimen i using Eq. (3.3a) with the assumed values of D_1, D_2 and D_3. A Matlab program using the Nelded-Mead simplex method [81] was written to optimize the error function for finding best fit parameters.

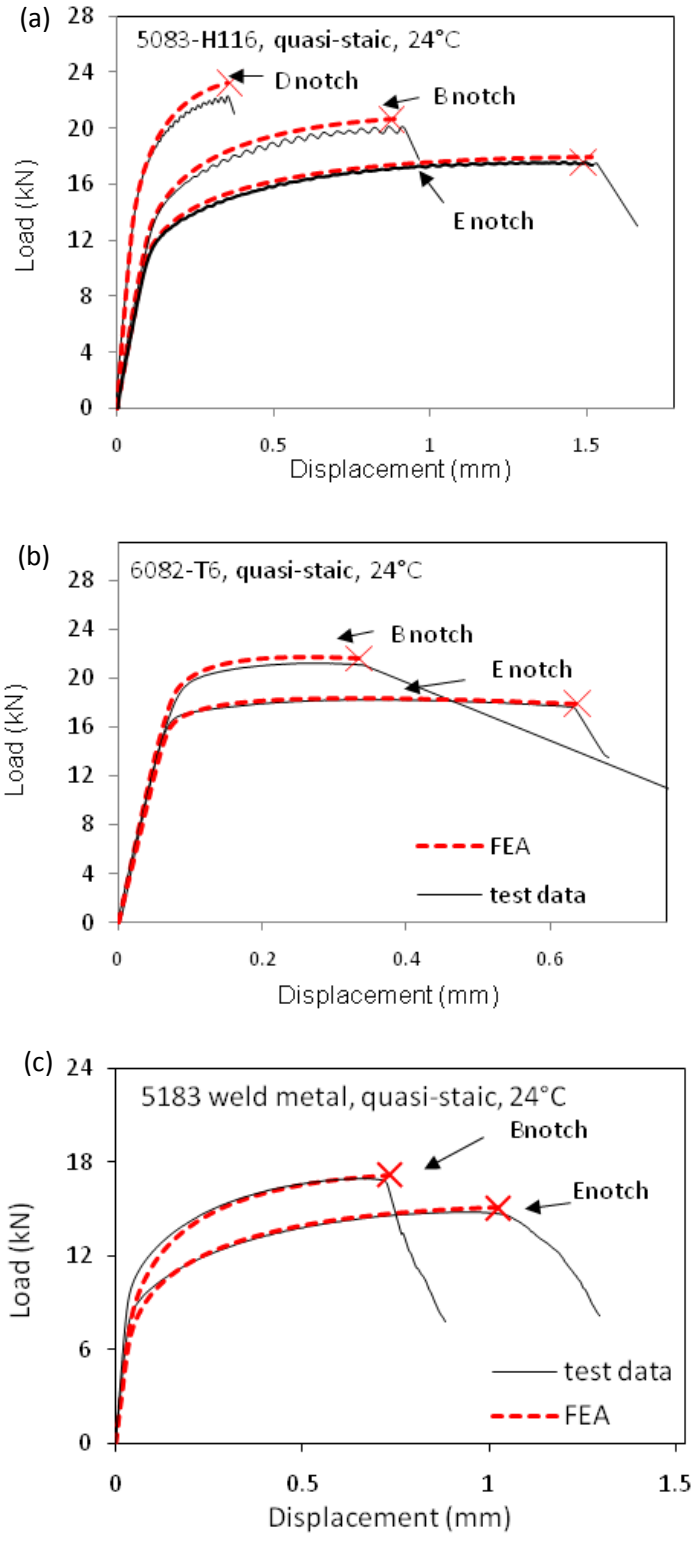

Figure 3. 5 Comparison of the predicted and measured load-displacement responses for the notched round bars at room temperature and QS loading rate: (a) 5083-H116 (b) 6082-T6 and (c) 5183 weld metal.

For round tensile specimens, failure started at the specimen center. As can be seen in Figure 3.6, the variation of stress triaxiality in the center element was not very large during the loading process for several specimens. A simple way to obtain the parameters is to average the stress triaxiality during the loading history up to fracture initiation, $T^*_{av} = \frac{1}{\varepsilon_f}\int_0^{\varepsilon_f} T^* d\bar{\varepsilon}^p$, and fit the failure strain vs. triaxiality data obtained for the smooth and notched specimens into a function in the form expressed as the first bracket of Eq. (3.3b).

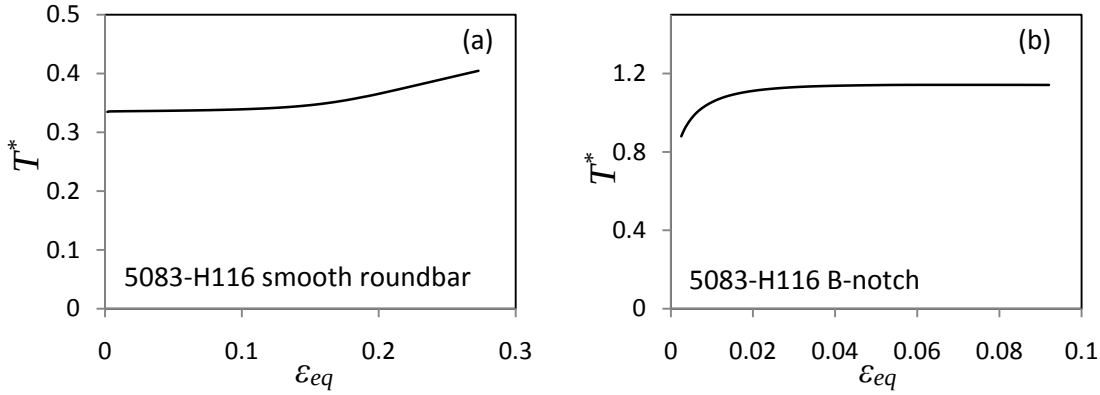

Figure 3. 6 Variation of the stress triaxiality in the center element during the loading history:(a) 5083-H116 smooth roundbar (b) 5083-H116 B-notch.

The calibrated D_1 to D_3 values from the optimization process described above are listed in table 3.4. Figure 3.7 shows the variation of effective failure strain with stress triaxiality at room temperature and QS loading, where the solid line represents the function form with the calibrated parameters (D_1, D_2, D_3) and the symbols represent the effective failure strain and the corresponding average stress triaxiality for the smooth and three notched tensile specimens respectively. It was found out that material parameters calibrated using average stress triaxiality were quite close to the ones given by

optimization method. For all three materials, failure strain was a decay function of the stress triaxiality. For the 5183 weld metal, due to the material variability introduced by the welding process, a larger scatter in strain to failure was observed in the experiments.

It is important to point out that the parameter D_1 calibrated above did not represent a limit value for ductility. As described by Johnson and Cook [17], the function form of ε_f versus T^* given by the first bracket of Eq. (3.3b) was only valid for triaxiality level lower than 1.5, they also mentioned that the fracture strain varied approximately in a linear manner from the value at T^* = 1.5 to a minimum value $\varepsilon_{f(\min)}$ corresponding to the spall stress.

Table 3.4 Calibrated parameters for the Johnson-Cook fracture model

	D1	D2	D3	D4	D5
5083-H116	0.005	0.845	-1.89	0.0897	7.970
6082-T6	0.0164	2.245	-2.798	0.0070	3.658
5183 weld metal	-0.900	1.185	-0.128	0.0975	9.584

For 5083-H116, the parameters calibrated appear different from the original paper [73], because the necking of the smooth roundbar specimen was not well captured. Here the calibration process was redone and new calibrated values were obtained as shown in Table 3.4.

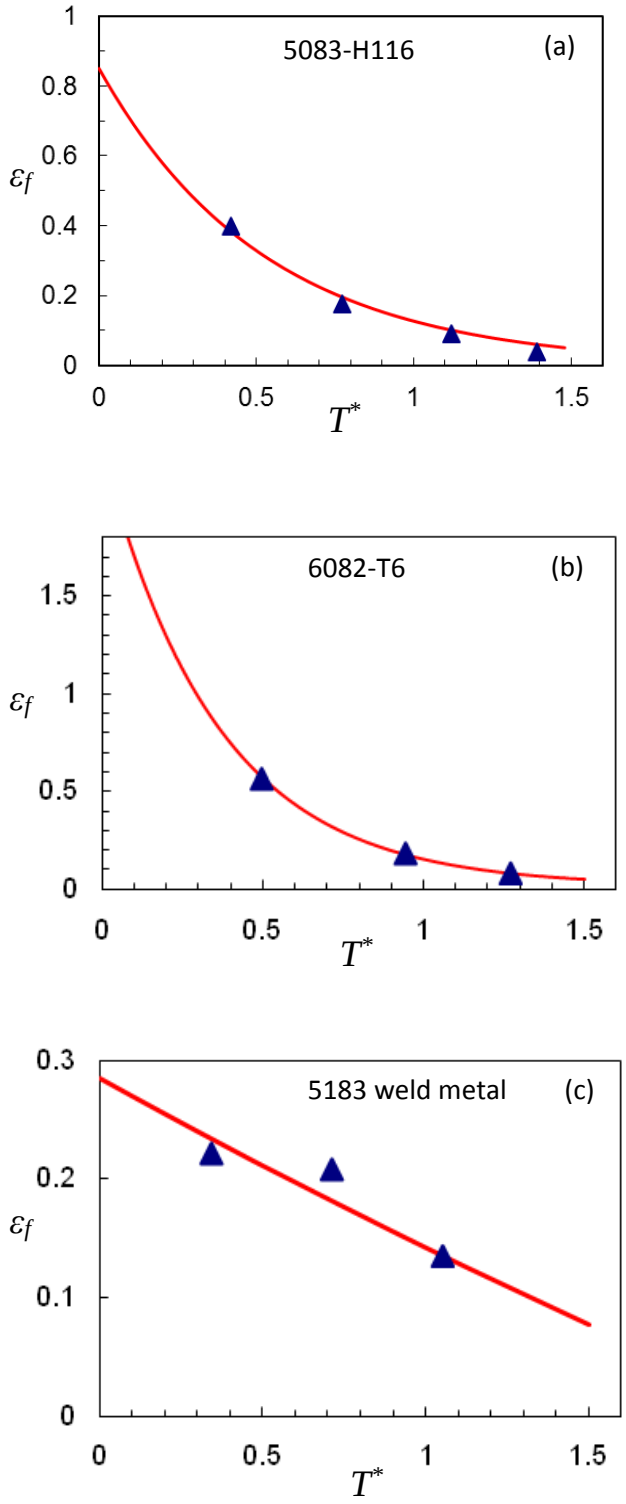

Figure 3. 7 Effective failure strain vs. stress triaxiality at room temperature, QS loading rate: (a) 5083-H116 (b) 6082-T6 and (c) 5183 weld metal.

3.3.3 Strain-rate effect on ductile failure strain

Similar to the plastic flow behavior, the variation of the failure strain with strain rate was not monotonic for 5083-H116. As shown in Figure 3.8, the 5083-H116 specimens tested at the intermediate loading rates exhibited lower elongation than those tested quasi-statically. The high inhomogeneity of plastic flow at the intermediate strain rate could be a possible explanation of the lower ductility than quasi-static loading [82]. In the strain rate range where DSA works, the negative strain rate hardening will lead to strain localization [83], which results in higher probability of failure and thus decreases the ductility.

At high strain rate, the ductility of 5083-H116 increased significantly. From the picture of the fractured specimens shown in Figure 3.9, a transition from a slant fracture surface at low rate to a cup-cone fracture surface at high rate was observed, which indicated the change of failure mechanism with the increasing loading rate. The cup-cone fracture surface was a result of the void formation, growth and coalescence mechanism while the slant fracture surface was caused by shear failure. This change of failure mechanism was also demonstrated by the microscopic pictures of fracture surface given by [77] for a high purity aluminum alloy with 5% Magnesium, which showed that the void size did not change much as the strain rate increased from 10^{-4} to $2s^{-1}$, but the voids grew to much larger sizes at the strain rate of $1.5x10^{3}$.

Because the fracture behavior of 5083-H116 at the intermediate loading rate was very complex, finite element analysis was only conducted at the level 3 loading rate. The Johnson-Cook plasticity model with the calibrated parameters given in Section 3.2 was

incorporated into ABAQUS via a user defined subroutine and used in the dynamic analysis.

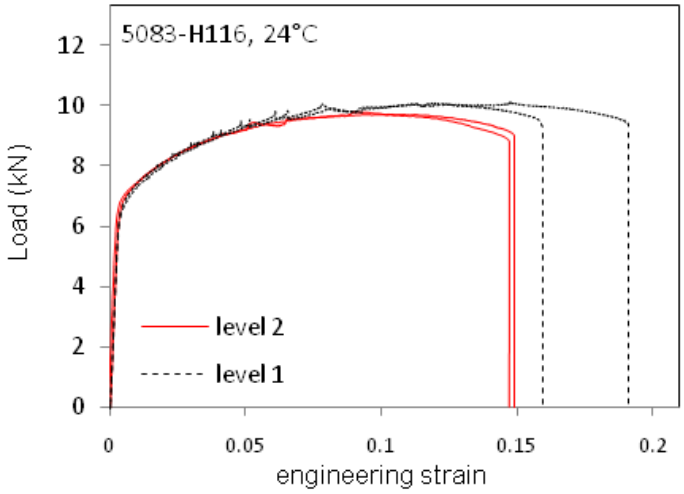

Figure 3. 8 Compares of the level 1 (QS) and level 2 (strain rate < 1 s^{-1}) load vs. engineering strain curves for 5083-H116 smooth specimens tested at room temperature.

(a) (b) (c)

Figure 3. 9 Fractured 5083-H116 specimens tested at room temperature and various loading rates: (a) quasi-static; (b) intermediate rate; (c) high rate.

In the high rate tests, engineering strains in the gage section were measured using strain gages. As the applied load approached the maximum value, necking developed in

the gage section, resulting the strain gage failure in two possible scenarios: 1) If necking occurred at the spot where the strain gage was placed, the strain gage might debond from the specimen after necking develops; 2) If necking occurred at a location other than where the strain gage was placed, the readings of the strain gage would not reflect the post-necking deformation experienced by the specimen. Consequently, the experimental records did not have the complete deformation history and we couldn't determine the failure point from the load-displacement records. Instead, we used the load vs. time records to find the instant when failure initiates (sudden load drop).

The finite element analysis of each specimen involved an iterative process. We varied the applied velocity at the specimen ends until the computed engineering strain vs. time of the gage section matched the experimental records. The experimental data suggested that the engineering strain rate in the gage section gradually increased to a constant value. Figure 3.10 (a)-(f) compare the computed load vs. time and engineering strain (gage section) vs. time histories with experimental records for the smooth round bars of the three materials tested at room temperature under level 3 dynamic loading.

Using the level 3 dynamic test data and the optimization procedure described above, the parameter D_4 was calibrated as 0.0897, 0.007 and 0.0975 for 5083-H116, 6082-T6 and the 5183 weld metal respectively. A positive D_4 indicated that the failure strain became larger as the strain rate increased. Compared to the significant increase of ductile failure strain at high strain rates, the D_4 value was quite small which indicated that 6082-T6 had very low rate sensitivity on ductility.

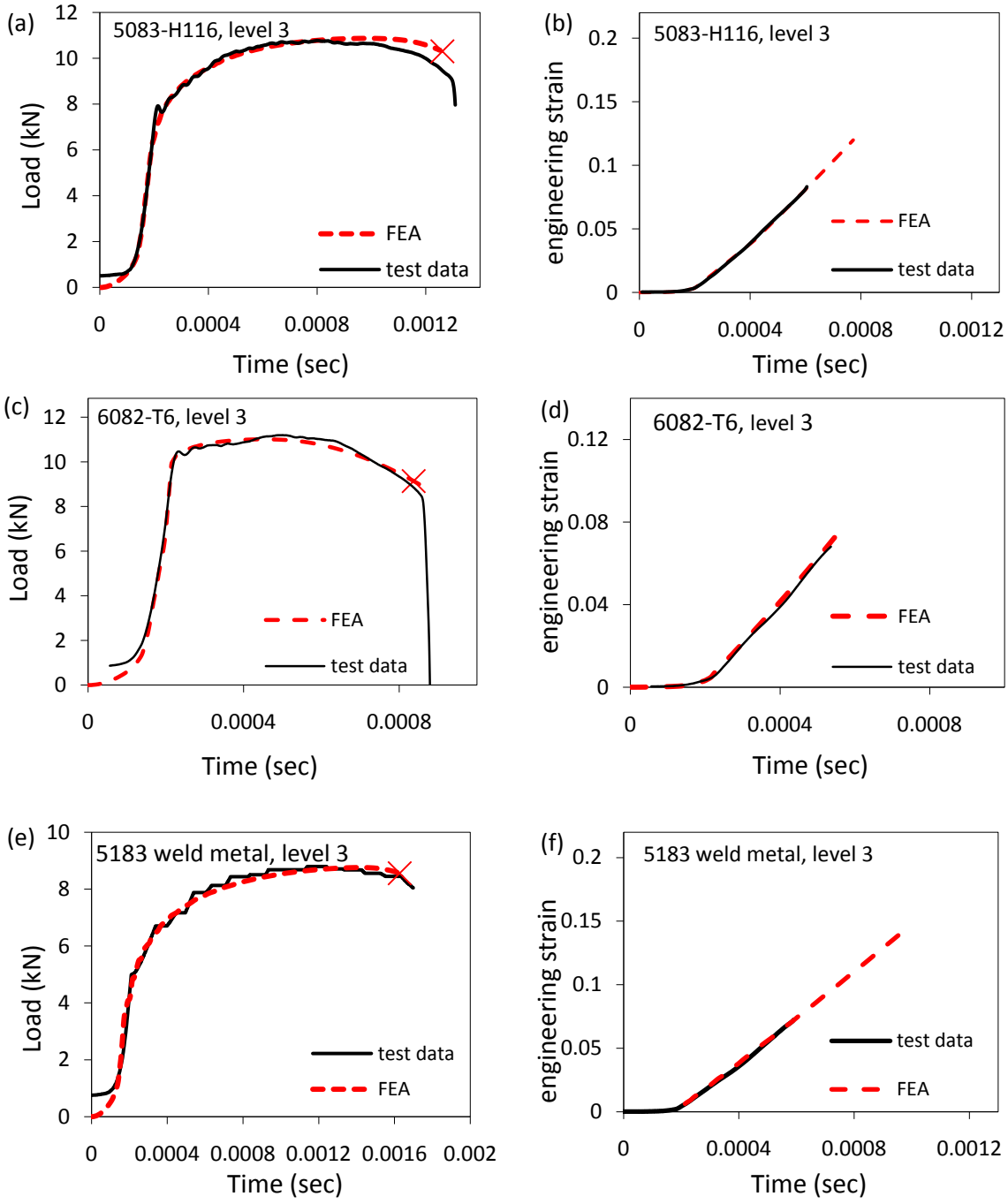

Figure 3. 10 Comparison of the computed load vs. time and gage section displacement vs. time histories with experimental records for the smooth round bar at room temperature and level 3 dynamic loading: (a, b) 5083-H116; (c, d) 6082-T6; (e, f) 5183 weld metal.

3.3.4 Temperature effect on ductile failure strain

Figure 3.11 shows the load vs. displacement curves for 5XXX series smooth specimens tested at 66 ℃ and 24 ℃ under QS loading. At either temperature level, several specimens were tested and only the specimens exhibiting least and most ductility were shown in Figure 3.11. The ductility was apparently lower at 66 ℃. However, the ductility of 5XXX at 149 ℃ was much higher than at 24 ℃, which could be seen from Figures 3.12(a) and (c). Based on the research of Skinner et al. [82] on different aluminum alloys where DSA effect exists, minimum ductility occurred at intermediate temperatures. At elevated temperatures two mechanisms affect ductility and flow behavior: dynamic recovery results in lower strength and higher ductility whereas DSA effect has opposite effects. In our case, DSA had a strong effect at lower elevated temperature (66 ℃), which resulted in lower ductility; however, at higher elevated temperature (149 ℃), the dynamic recovery dominated and serration of stress-strain curve was not observed.

From the above discussions, the Johnson-Cook fracture model was not suitable for the 5XXX alloys in the temperature range considered. The calibrated D_5 values in Table 3.4 for the 5XXX alloys were from data tested at RT and at 149 ℃, which only serve the purpose for comparison of the temperature effect on ductility of different materials.

In contrast to the 5XXX series, the ductility of 6082-T6 increased as temperature increased monotonically as shown in Figure 3.12 (b), and the failure strain of this material could be very well described by the Johnson-Cook fracture model.

The parameter D_5 was calibrated as 7.970, 3.658 and 9.584 for 5083-H116, 6082-T6 and the 5183 weld metal respectively. A positive D_5 indicated that the failure strain became larger as temperature increased. 6082-T6 showed less ductility change compared to the other two materials. Figure 3.12 also compares the computed and the experimentally measured load-displacement curves of the smooth round tensile specimen tested at different temperatures.

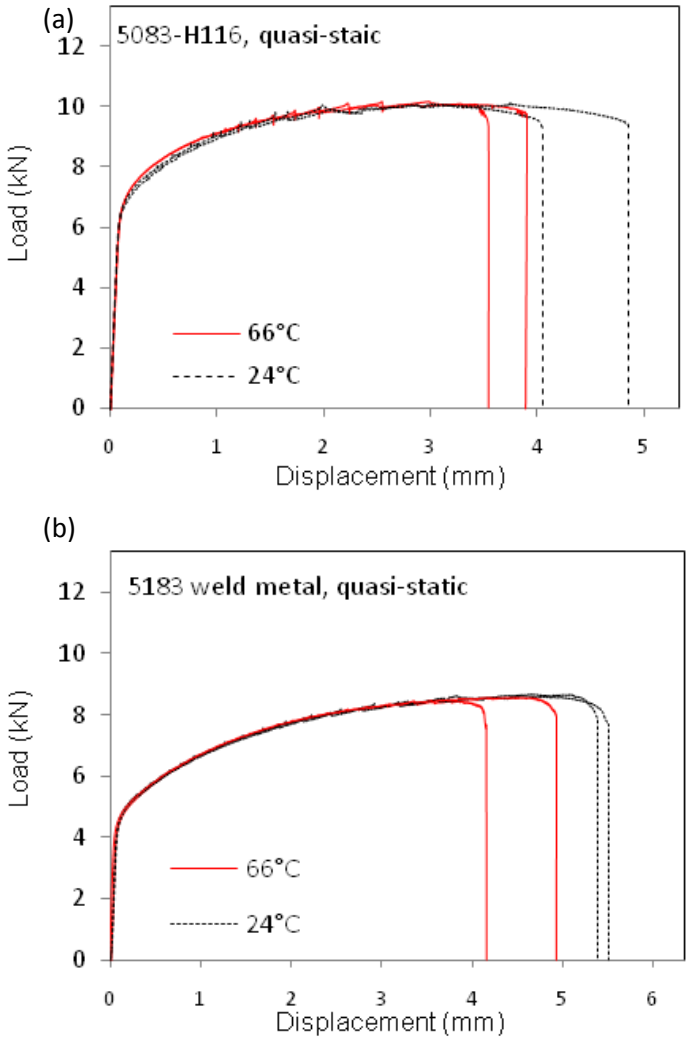

Figure 3. 11 Comparison of the QS load vs. displacement curves for smooth specimens tested at 66 ℃ than 24 ℃: (a) 5083-H116 (b) 5183 weld metal.

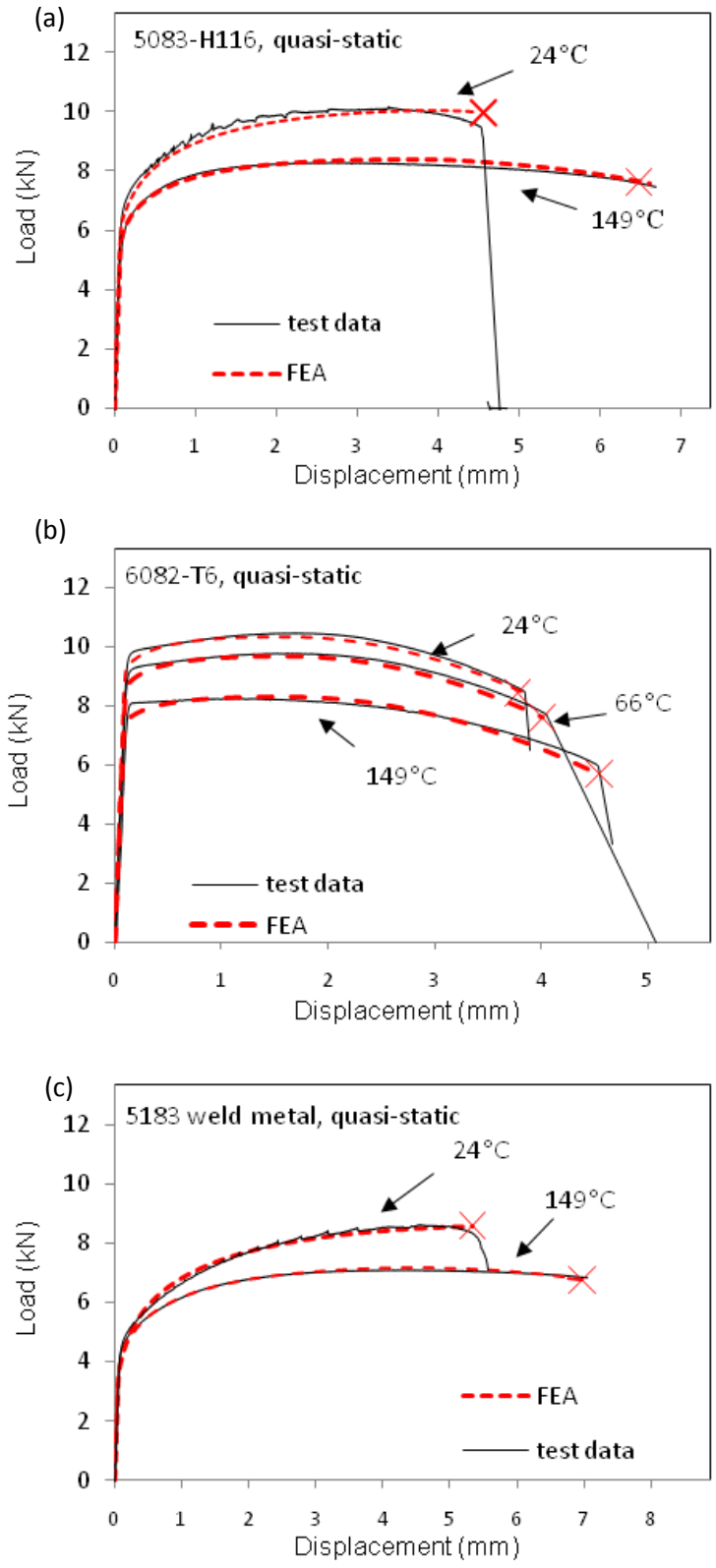

Figure 3. 12 Comparison of the predicted and measured load-displacement responses for tests at different temperatures: (a) 5083-H116 (b) 6082-T6 and (c) 5183 weld metal.

3.4 Concluding Remarks

In this study, the effects of strain rate and temperature on the plastic response and ductile failure strain of three aluminum alloys often used in marine structures, AA 5083-H116, AA 6082-T6 and AA 5183 weld metal, were investigated. As a first step, the applicability of the Johnson-Cook plasticity and ductile fracture models was examined. The primary findings can be summarized as follows:

1) Flow stress and failure strain of AA 5083-H116 showed negative strain rate dependency at low dynamic loading rate ($< 1s^{-1}$) at room temperature, which was strongly related to the DSA effect. But at high strain rate, this material exhibited rate hardening and significant increase in ductility.

2) The flow stress of the 5183 weld metal was not sensitive to the strain rate, whereas the ductility increased significantly at high strain rate.

3) At room temperature the flow stress of AA 6082-T6 displayed strain rate hardening effect while the ductility increase at high strain rate was insignificant.

4) Before the temperature was raised beyond a certain level, the QS flow stresses of AA 5083-H116 and the 5183 weld metal showed no obvious temperature dependency but the ductilities of these alloys were lower at 66 ℃ than at 24 ℃. As temperature continued to increase, both materials displayed noticeable temperature softening and increase of ductility.

5) Both temperature softening and increase of failure strain with elevating temperature of AA 6082-T6 could be well described by the Johnson-Cook plasticity and fracture models.

6) For all three materials, the equivalent strain to failure was a decaying function of the stress triaxiality and well captured by the Johnson-Cook model, and the material parameters calibrated using average stress triaxiality gave enough accuracy in comparison with the optimization method.

Our results showed that the strain-rate dependent and temperature dependent relations given by the Johnson-Cook plasticity and fracture models generally cannot applicable for the AA 5XXX series especially in the temperature and loading rate range where DSA effect exist. To develop more accurate and useful mathematical relations for rate and temperature dependencies of these materials, further experimental and numerical work needs to be conducted. In this chapter, only axisymmetric tensile specimens were tested, and the *J3* or the Lode angle effect was not taken into account, which is discussed in Chapter 4.

CHAPTER IV

FRACTURE MODELING INCLUDING THE RESIDUAL STRESS EFFECT

In this chapter, the stress state effect on plasticity and ductile fracture behaviors of an AA 5083-H116 was further explored through a series of experiments under quasi-static loading at room temperature，with the focus on the Lode angle/third deviatoric stress. A recently developed stress state dependent plasticity model, the J_2-J_3 plasticity model, was implemented to describe the plastic response of this material. Furthermore, the Xue-Wierzbicki ductile failure criterion, which defines the damage parameter as a function of the stress triaxiality and the Lode angle, was implemented to model the material fracture behavior. The calibrated plasticity model and ductile failure model were utilized to study the residual stress effect on ductile fracture resistance. A local out-of-plane compression approach was employed to generate residual stress fields in the compact tension specimens. Fracture tests of C(T) specimens having zero, positive and negative residual stresses were conducted.

4.1 Plasticity and Fracture Models

The most popular continuum plasticity model is the so-called J_2-flow theory. This theory assumes hydrostatic stress as well as the third invariant of the stress deviator has no effect on plastic yielding and the flow stress However, increasing experimental

evidences showed that this assumption was invalid for many materials. Inspired by the extensive experimental results reported by Spitzig et al. [84], Brunig [85] presented an I_1-J_2 yield criterion which incorporate the pressure dependency. Later, the third invariant of stress deviator, J_3, was added to the I_1-J_2 yield criterion by Brunig [86] to study the deformation and localization behavior of hydrostatic stress sensitive metals. Recently, Gao et al. [69, 87] noticed the plastic response of a 5083 aluminum alloy was also J_3 dependent. A I_1-J_2-J_3 plasticity model proposed by Gao et al. [69] was adopted in this study.

4.1.1 Stress state dependent Plasticity modeling

The isotropic, stress state dependent plasticity model is formulated in terms of the invariants of stress tensor. The general forms of the yield function (F) and the flow potential (G) are expressed as functions of I_1, J_2 and J_3. Eq. (4.1) describes the yield condition and the flow rule:

$$F(I_1, J_2, J_3) - \bar{\sigma} = 0; \quad \dot{\varepsilon}_{ij}^{p} = \dot{\lambda} \frac{\partial G(I_1, J_2, J_3)}{\partial \sigma_{ij}} \tag{4.1}$$

where $\bar{\sigma}$ is the hardening parameter, $\dot{\varepsilon}_{ij}^{p}$ are the rates of the plastic strain components and $\dot{\lambda}$ is the plastic multiplier. If plasticity behavior of this material has no pressure dependency, the following first order homogeneous function can be used to defining the yield function (F) [69]

$$F = c_1 (27 J_2^3 + b_1 J_3^2)^{1/6} \tag{4.2}$$

where b_1 are material constants and c_1 is determined by substituting the uniaxial condition into Eq. (4.2) so that the equivalent stress defined by $\sigma_e = F$ equals to the applied stress:

$$c_1 = 1/(4b_1/729+1)^{-1/6} \tag{4.3}$$

The flow potential (G) takes a similar form

$$G = c_2(27J_2^3 + b_2 J_3^2)^{1/6} \; ; \; c_2 = 1/(4b_2/729+1)^{-1/6} \tag{4.4}$$

If the flow potential and the yield function are identical, i.e., $F = G$, a material is said to follow the associated flow rule. Furthermore, if $b_1 = b_2 = 0$, the plasticity model degenerates to the formulation of classical J_2-flow theory and σ_e becomes the von Mises equivalent stress.

The hardening parameter depends on the strain history. By enforcing the equivalence of plastic work, i.e,

$$\bar{\sigma}\dot{\bar{\varepsilon}}^p = \sigma_{ij}\dot{\varepsilon}_{ij}^p \tag{4.5}$$

The equivalent plastic strain increment can be defined as

$$\dot{\bar{\varepsilon}}^p = \sigma_{ij}\dot{\varepsilon}_{ij}^p / \bar{\sigma} \tag{4.6}$$

Therefore, the hardening behavior can be described by a stress vs. plastic strain relation $\bar{\sigma}(\bar{\varepsilon}^p)$, where $\bar{\varepsilon}^p = \int \dot{\bar{\varepsilon}}^p \mathrm{d}t$.

4.1.2 Fracture criterion

The cumulative strain damage models assume that the damage toward eventual fracture is due to the plastic deformation history and the equivalent fracture strain depends on the stress state subjected by the material. Here a damage parameter, *D*, is introduced and given by

$$D = \int_0^{\bar{\varepsilon}^p} \frac{d\bar{\varepsilon}^p}{\varepsilon_f(\boldsymbol{\sigma})} \tag{4.7}$$

with ε_f being the failure strain under the current stress state characterized by the triaxiality T^* and the Lode parameter ξ

$$\xi = \frac{27 J_3}{2\sigma_e{}^3} \tag{4.8}$$

ξ is related to the Lode angle, θ, through $\xi = \cos(3\theta + \pi/2)$. Therefore

$$\varepsilon_f(\boldsymbol{\sigma}) = \varepsilon_f(T^*, \xi) \tag{4.9}$$

Under proportional loading and if T^* and ξ remain unchanged during the loading history, when the equivalent plastic strain, $\bar{\varepsilon}^p$, reaches the critical value ε_f, *D* will equal to unit. For general cases, when the cumulative damage according to Eq. (4.7) reaches one, ductile failure is said to have happened.

In Eq. (4.9), if ξ is a constant, ε_f becomes a function of T^* only. Here an exponentially decaying function having the same form as the Johnson-Cook fracture model is used to describe the dependency of ε_f on T^*

$$\varepsilon_f^{\xi=const.} = [A + B\exp(C \cdot T^*)] \tag{4.10}$$

where *A*, *B* and *C* are material constants to be calibrated using experimental data.

The Lode angle distinguishes the deviatoric stress state and it is mathematically convenient to use the parameter ξ defined in Eq. (4.8), whose range is from -1 to 1, to quantify the Lode angle. Wilkins et al. [48] was first to introduce the effect of Lode angle on ductile fracture, where the function $\varepsilon_f(T^*, \xi)$ was taken to be symmetric with respect to ξ. Here we follow Xue and Wierzbicki [88] and assumed $\varepsilon_f(T^*, \xi)$ takes the following form

$$\varepsilon_f(T^*, \xi) = \varepsilon_f^{\xi=1}(T^*) - (\varepsilon_f^{\xi=1}(T^*) - \varepsilon_f^{\xi=0}(T^*))[1-(1-|\xi|^n)^{1/n}] \tag{4.11}$$

where a symmetric function of ξ is used to interpolate the value of ε_f between two bounding values $\varepsilon_f^{\xi=1}$ and $\varepsilon_f^{\xi=0}$. The two bounding curves, $\varepsilon_f^{\xi=1}(T^*)$ and $\varepsilon_f^{\xi=0}(T^*)$ given by Eq. (4.12), can be calibrated by conducting simple mechanical tests: ξ =1 for notched, round tensile specimens and ξ =0 for flat-grooved plates under tension and the thin-walled torsion specimen. Calibration of parameter *n* requires performing additional tests using specimens having ξ values between zero and one, which can be done by conducting combined torsion-tension tests of thin-walled cylindrical specimens.

$$\varepsilon_f^{\xi=1} = [A_1 + B_1 \exp(C_1 \cdot T^*)]; \quad \varepsilon_f^{\xi=0} = [A_2 + B_2 \exp(C_2 \cdot T^*)] \tag{4.12}$$

Fracture is assumed to have initiated at a material point once the failure criterion is reached. The post-initiation softening process needs to be considered in order to model crack propagation. As illustrated by Li et al. [89], because the finite element has a finite

size, additional work is needed to propagate the crack through the element, i.e., the element gradually loses its strength as crack grows through it. A mesh-independent, post-initiation material degradation model based on an effective plastic displacement (u_f) is available in ABAQUS [79] and was adopted in this study. The element was removed when it was fully degraded (stresses being reduced to zero).

The plasticity and ductile fracture models described above were implemented into ABAQUS/Explicit via a user defined subroutine VUMAT following the a Backward-Euler procedures developed by Kim and Gao [90] and Gao et al. [69].

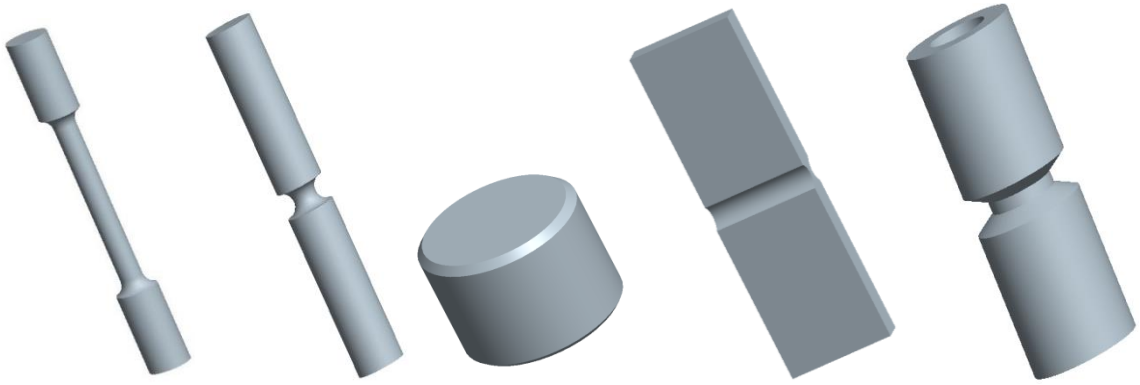

Figure 4. 1 Sketches of a smooth round bar, a notched round bar, a cylindrical compression specimen, a grooved plane strain specimen and a torsion specimen.

4.2 Model Calibration for AA 5083-H116

The plasticity and ductile fracture models described above were calibrated in this section for an AA 5083-H116. Except the smooth and notched round tensile bars described in Chapter 3, the test matrix also included cylindrical compression specimens, grooved plane strain specimens and the Lindholm-type specimen subjected to different

tension-torsion ratios, as plotted in Figure 4.1. Detailed descriptions of specimen geometries and finite element modeling can be found in [69]. All specimens were machined from a 25mm thick plate, with tensile axes oriented transversely to the rolling direction. All tests were performed at room temperature and are considered to be quasi-static.

4.2.1 Calibration of Plasticity model

The stress-strain relationship was obtained from the smooth round bar test as given in Chapter 3. The pressure insensitivity of plasticity was proved by comparing the numerical predictions and the experimental measurements for the smooth tensile specimen and the compression specimen respectively, Figure 4.2. The experimental data are represented by black thinner lines while the finite element result is represented by a red thicker line. Using the stress strain data obtained from uniaxial tensile test, the predicted load-displacement curve of the cylindrical compression specimen fitted well with the test data as shown in Figure 4.2(b), which indicated the plasticity behavior of this material had no pressure dependency.

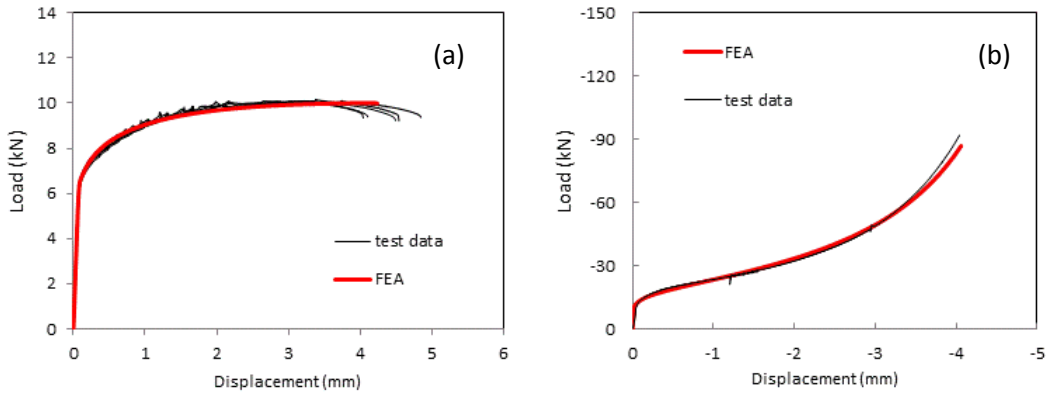

Figure 4. 2 Comparison of the numerical and experimental load vs. displacement curves for (a) the smooth tensile specimen and (b) the compression specimen.

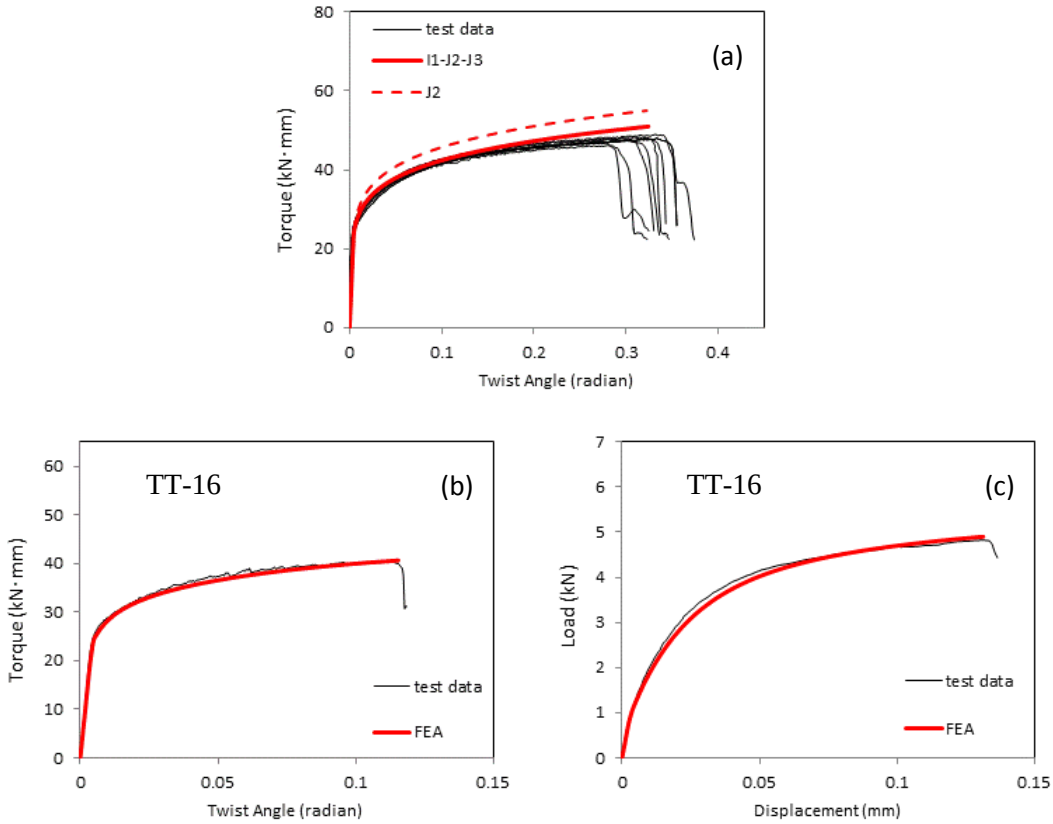

Figure 4. 3 Comparisons of load vs. displacement and/or torque vs. twist angle responses between the experimental data: (a) the pure torsion specimen, (b) & (c) the torsion-tension specimen (TT-16)

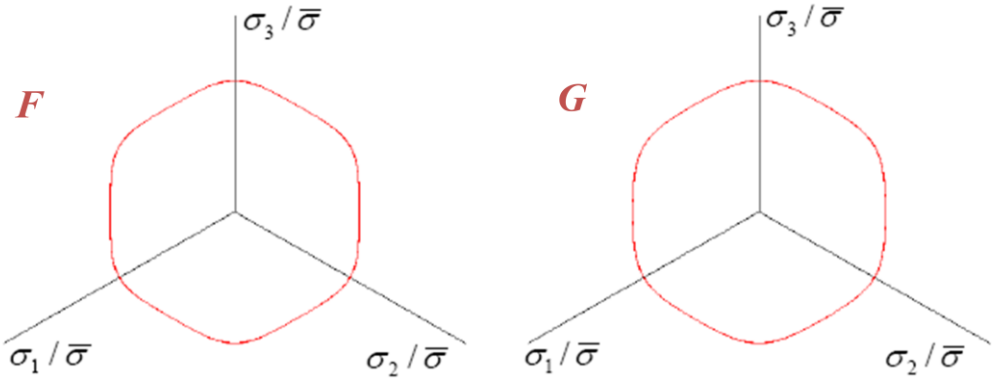

Figure 4. 4 Yield surface and flow potential in the deviatoric plane

Torsion and tension specimens exhibit different Lode parameters, thus were used to examine the J_3 dependency. As found in reference [69], the simulation of pure torsion test using stress-strain curve from uniaxial tensile test and the J_2-plasticity model over-predicted the torque vs. twist angle responses, as shown in Figure 4.3(a) (dotted red line), which indicated the plastic response is J_3 dependent. It was found that parameter b_1 had strong effect on the predicted torque vs. twist angle response of the torsion specimen while parameter b_2 had pronounced effect on the predicted axial force-displacement response of torsion-tension specimen. The final calibrated material constants were b_1 = -60.75 and b_2 = -50. Figure 4.3(b) and (c) compare the predicted and measured torque vs. twist angle and axial force-displacement responses. With these material constants determined, the yield surface (F) and flow potential (G) in the deviatoric stress plane are given in Figure 4.4.

Other specimens which were not used in the calibration process were simulated to verify the calibrated material model. Figure 4.5(a) compares the predicted and measure load-displacement curves for a notched round bar, Figure 4.5(b) compares the predicted and measure load-displacement curves for a grooved plane strain specimen, and Figure 4.5(c) and (d) compare the predicted and measured torque vs. twist angle and axial force-displacement responses for a torsion-tension specimen with a different torsion-tension ratio than the specimen shown in Figure 4.3. As can be seen in Figure 4.5, excellent agreements between numerical and experimental results were found for all cases.

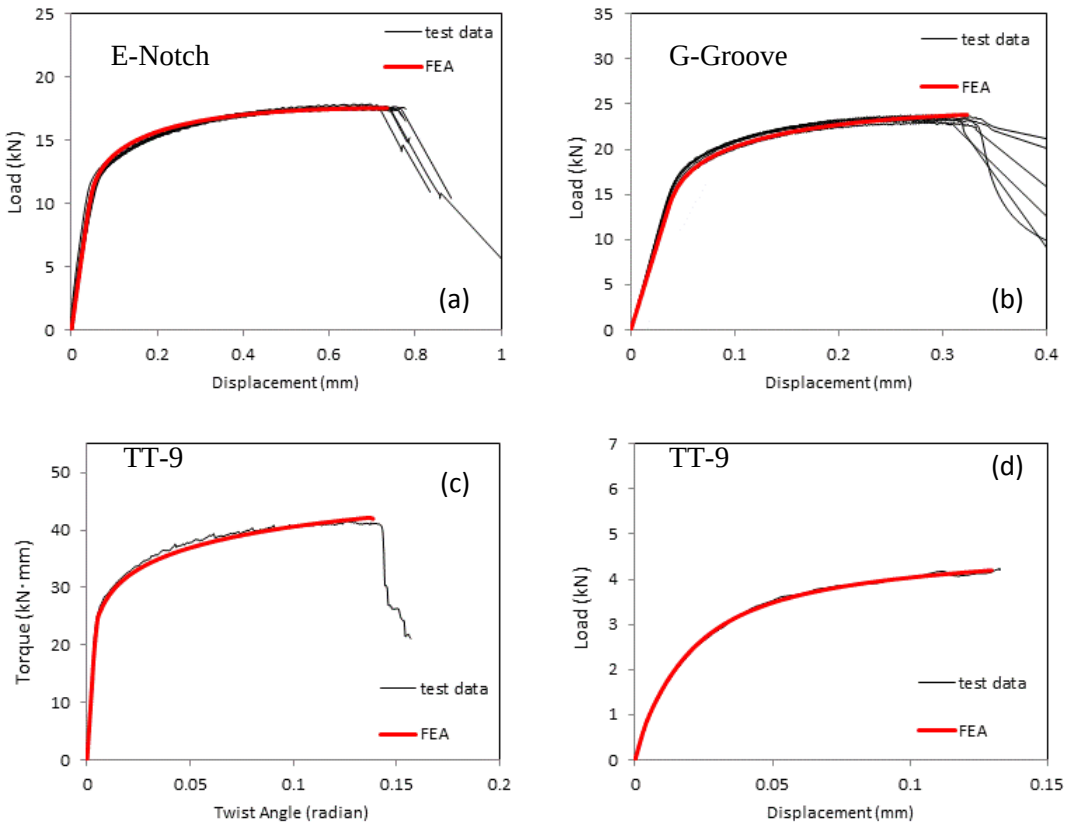

Figure 4. 5 Comparisons of the predicted load vs. displacement and/or toque vs. twist angle responses: (a) notched round bar (E-Notch); (b) plane strain specimen (G-Groove); (c) & (d) torsion-tension specimen (TT-9).

4.2.2 Calibration of the fracture model

As described in Section 4.1.2, failure strain is a function of T^* and ξ. However, both T^* and ξ at a material point varies during the loading history [69], the average values, given by Eq. (4.13), were used.

$$T^*_{av} = \frac{1}{\varepsilon_f}\int_0^{\varepsilon_f} T^* d\bar{\varepsilon}^p ; \quad \xi_{av} = \frac{1}{\bar{\varepsilon}_f}\int_0^{\bar{\varepsilon}_f} \xi d\bar{\varepsilon}^p \tag{4.13}$$

Using the calibrated J_2-J_3 plasticity model, the load-displacement response of each tested specimen was computed. The method to obtain the critical strain was same as

described in Chapter 3. The histories of stress triaxiality, Lode parameter, and plastic strain increment of the critical element were direct outputs, and T_{av}^{*} and ξ_{av} were calculated according to Eq. (4.13).

For axi-symmetric tensile specimens, including smooth round bar and all notched round bars, ξ in the center element equaled to 1 and T^{*} varied with the notch radius. For grooved plane strain specimens, ξ in the center element equaled to 0 and T^{*} varied with the groove radius. For the Lindholm-type specimen subjected to pure torsion, both ξ and T^{*} equaled to zero in the gage section. For the Lindholm-type specimen subjected to combined torsion and tension, ξ and T^{*} in the gage section varied with the imposed torsion-tension ratio.

Fitting the failure strain vs. triaxiality data obtained from $\xi = 1$ and $\xi = 0$ specimens to functions given by Eq. (4.12), parameters (A_1, B_1, C_1) and (A_2, B_2, C_2) were calibrated. The calibrated values were $A_1 = 0$, $B_1 = 0.85$, $C_1 = -1.9$ (these were different from Chapter 3, because a different approach was used), $A_2 = 0$, $B_2 = 0.64$ and $C_2 = -1.9$. The ε_f vs. T^{*} curves for these two cases are plotted in Figure 4.6. As can be seen, for both cases the failure strain decreased dramatically as the stress triaxiality increased. The difference between the two curves indicated the Lode angle dependency, although this dependency was not as strong compared to the result obtained by Bai et al. [44] for aluminum alloy 2024-T351. Using the two ε_f vs. T^{*} curves and the torsion-tension data, which had ξ values between 0 and 1, the shape parameters n was determined. The orange circular symbol in Figure 4.6 shows a data point obtained from a torsion-tension specimen having $\xi = 0.81$ and $T^{*} = 0.31$. The calibrated shape parameter for this material was $n = 1.31$.

After the parameters in Eq. (4.11) were calibrated, the 3D failure surface in the space of ξ and T^* was fully defined. Figure 4.7 shows the 3D failure locus by using the calibrated parameters A_1 =0, B_1=0.85, C_1=-1.9, A_2 =0, B_2=0.64, C_2=-1.9, and n = 1.31.

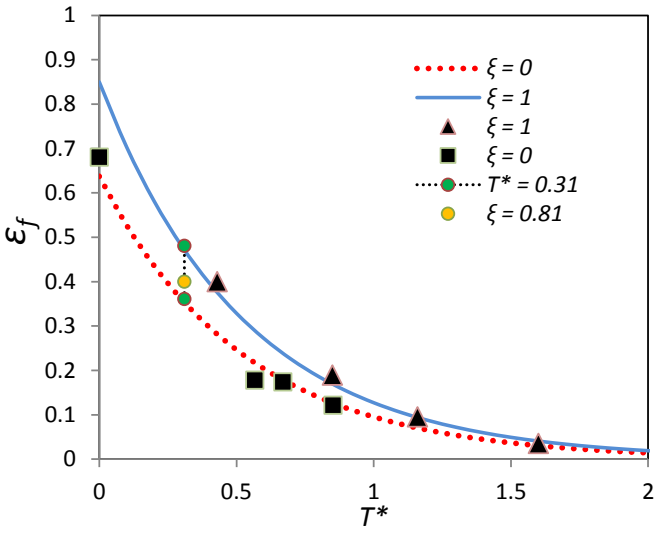

Figure 4. 6 Failure strain vs. stress triaxiality.

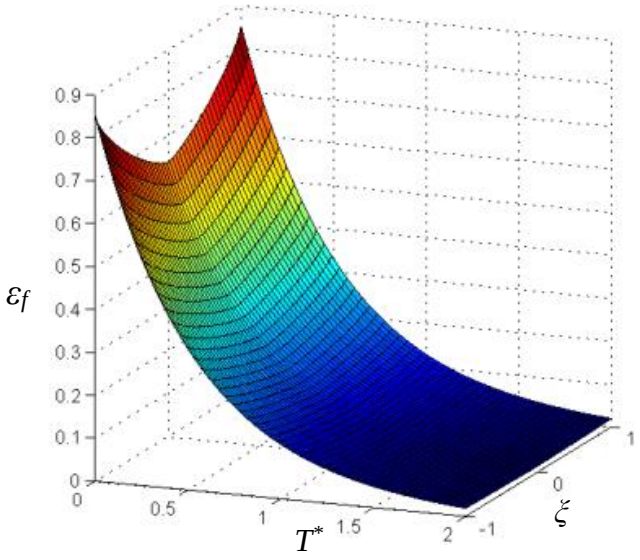

Figure 4. 7 3D plot of the failure locus.

4.3 Fracture Specimen and Residual Stress Generation

Here we employed the LOPC approach and used two pairs of compression punches to generate various residual stress fields in C(T) specimens. In the numerical analysis, the residual stress field was obtained by conducting finite element simulation of the out-of-plane compression process. After the residual stress field was generated, fracture tests of C(T) specimens having positive and negative residual stresses were conducted and simulated numerically.

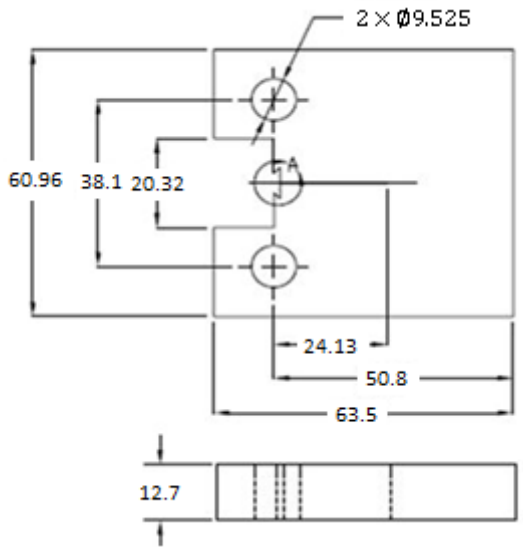

Figure 4. 8 Geometry of the plane-sided C(T) specimen (mm).

The 1/2T C(T) specimens (thickness: 12.7 mm) were used in fracture tests. The specific design utilized in this study was modified from the standard design specified by ASTM-E1820 as a means of applying controlled residual stresses. The aim was to introduce residual stresses into the C(T) specimen by compressing the two faces with cylindrical punches to a specified displacement to produce a pair of permanent

depressions on both faces of the specimen. Figure 4.8 shows the geometry of the C(T) specimen.

4.3.1 Experiment design

From the analyses performed by Mahmoudi et al. [43], the size and position of the punching tools had strong influence on the magnitude and distribution of the residual stress field. Thus one can tailor the residual stress field at the crack tip by varying the position of the set of depressions relative to the crack tip. Mahmoudi et al [43] conducted two series of tests, one involved single pair of compression tools which place punches directly along the line of crack, the other one used double pairs of punches. To avoid the direct contact of punches on the material in the crack growth plane, only double pairs punch LOPC method was adopted here. The position of punches are illustrate in the Figure 4.9. When the punches are ahead of the crack tip, Figure 4.9(a), positive residual stress will be generated; and negative residual stress will be generate for punches behind of the crack tip, Figure 4.9(b).

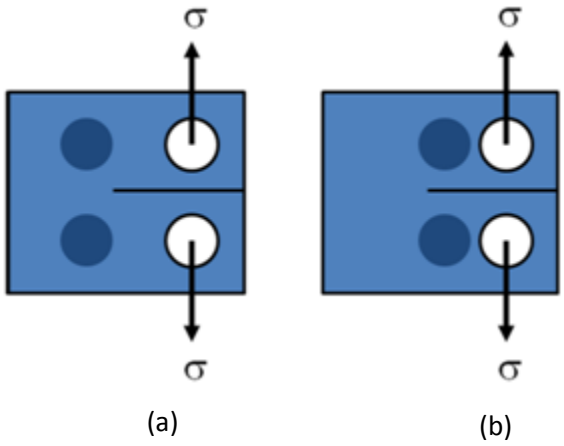

Figure 4. 9 Punching tool positions

A series finite element analyses were conducted first to determine the diameter, applied displacement, and locations of each depression, in order to obtain larger residual stress influenced region. From these analyses, the 8.89 mm punch radius was selected and the punch position was chosen to be $\delta_x / R = 1$ and -1, $\delta_y / R = 1.2$, where δ_x and δ_y are the distances from the punch center to the crack tip parallel and normal to the crack growth direction respectively and *R* is the radius of the punch.

4.3.2 Mechanical Test Preparation

With the aid of the above analyses, fixtures were designed for use in side compression. The specimen was sandwiched between two guide plates. The guide plates were aligned with the specimen by threading two pins through one guide plate, the pin loading holes of the specimen, and through the other guide plate. These guide pins ensured consistency in locating the side compression indentations between specimens. Two side compression punches (one on either side of the crack plane) were placed in the top guide plate and two mating punches were placed in the bottom guide plate. Once assembled, the compression force was applied to the top punches while the bottom punches remained fixed. Sets of fixtures were designed and machined for both the $\delta_x / R = 1$ and $\delta_x / R = -1$ configurations ($\delta_y / R = 1.2$). Figure 4.10 illustrate the schematic of side compression fixture.

4.4 Experimental and Numerical Results

In this section, the results of the experiment and numerical analysis for the fracture specimen with or without residual stresses are presented and compared.

4.4.1 C(T) specimens without residual stress

The plane-sided C(T) specimen was considered first. Due to symmetry of the geometry and the boundary conditions, only a quarter of the specimen was meshed. The element size along the crack path was 0.254 mm in all three directions. The eight-node, isoparametric, brick elements with reduced integration were used in the analysis. Figure 4.11(a) shows the quarter-symmetric finite element mesh and Figure 4.11(b) shows a close-up of the crack tip region.

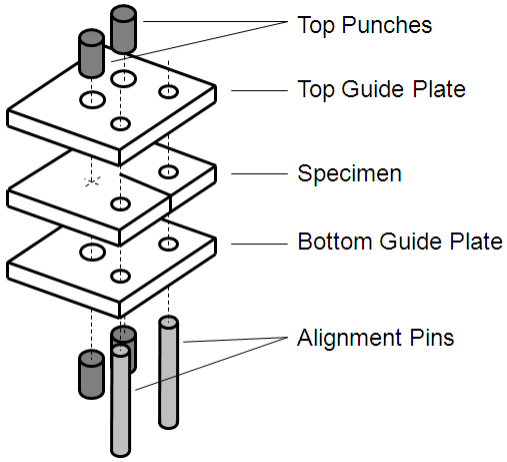

Figure 4. 10 Schematic of side compression fixture

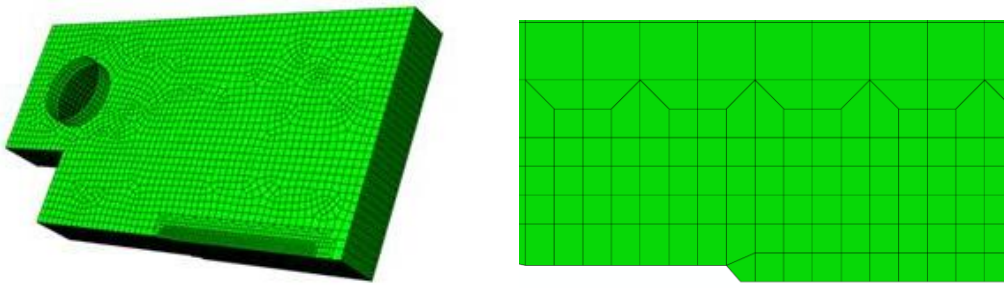

(a) (b)

Figure 4. 11 Finite element mesh of the plane-side CT specimen

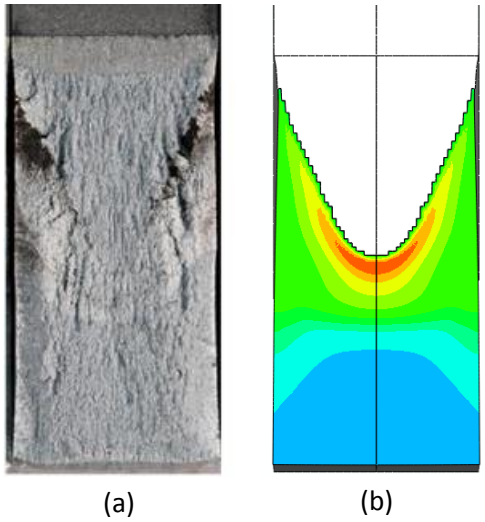

Figure 4. 12 Fracture surface and stress triaxiality distribution in the plane-sided C(T) specimen

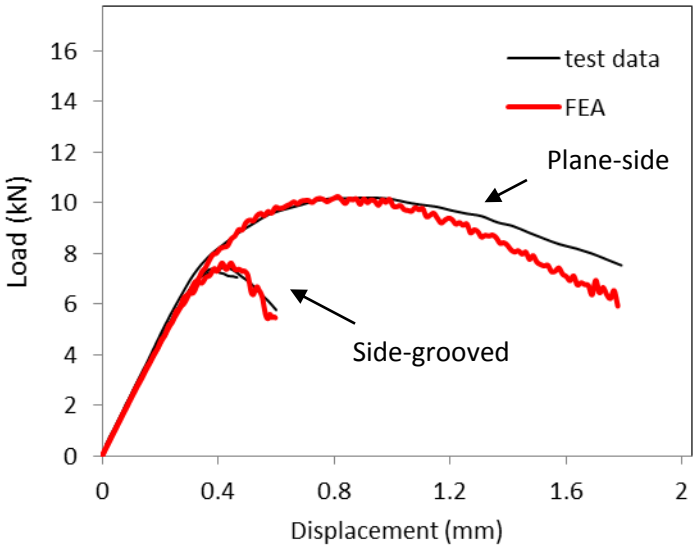

Figure 4. 13 Comparison of the load-displacement curves for side-grooved and plane-sided specimens

Figure 4.12 compares the predicted crack profile with the fracture surface of the broken specimen and the agreement was very good. A “V” shape crack profile, seen in both test and simulation results, showed strong crack tunneling effect. This was due to the variation of the constraint in the thickness direction, where the plane stress prevailed at the free surface and the plane strain condition prevailed in the center. Figure 4.12 (b) displays the stress triaxiality contour on the crack plane, where the stress triaxiality decreased from the mid-plane to the free surface.

The computed and measured load vs. load line displacement curves of the plane-sided C(T) specimen are compared in Figure 4.13. Good agreement was observed before fracture initiation and at the early stage of crack growth. The simulation result slightly under predicted the applied force at the later stage.

In order to promote plane strain constraint along the crack front and obtain more uniform though thickness crack growth, the C(T) specimens were side-grooved by 20% of the thickness (10% each side). Consequently, a quarter-symmetric finite element model was generated for the side-grooved specimen, in which the same element type and size were used as those for the plane-sided specimen. With the side grooves, the constraint level was significantly raised close to specimen edges and as a result, more uniform crack growth (less tunneling) was observed. Figure 4.14(a) compares the predicted crack profile with the crack surface of the broken specimen. Figure 4.14(b) shows stress triaxiality became almost uniform through specimen thickness due to the side grooves.

Because the constraint level was raised by the side grooves, fracture became easier, resulting in a lower load carrying capacity by the specimen. Figure 4.13 compares the load-displacement curves for the side-grooved specimen with that of the plane-sided specimen. The load carrying capacity of the C(T) specimen was significantly reduced by the side grooves. The model predicted load-displacement curves are also included in Figure 4.13, showing good agreements with test data.

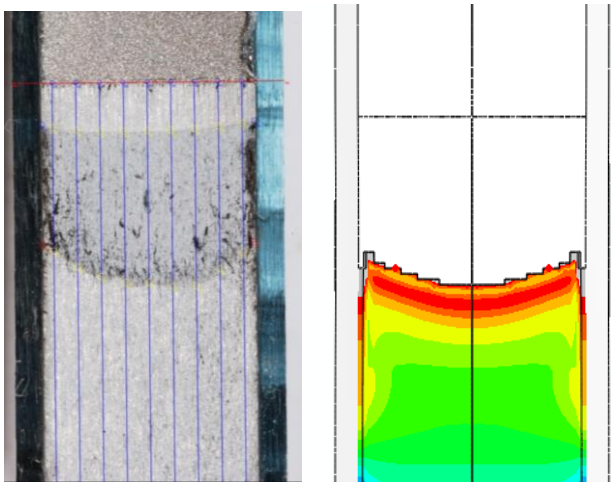

Figure 4. 14 Fracture surface and stress triaxiality distribution in the side-grooved C(T) specimen.

In conducting the experiments, the test was stopped after some amount of crack extension and the specimen was broken by fatigue loading. The post fatigue marks were used to determine the amount of crack growth. Due to the non-uniform crack growth through the specimen thickness, a nine-point average was used to determine the crack length. We compared the model predicted crack growth with experimental measurements at the same applied load levels and found very good agreements between the two. For examples, C(T)-17 had crack extensions of 6.81 mm (measured from post fatigue marks)

when the test was stopped. The finite element analyses predicted the amount of crack extension of 7.11 mm at the same load level.

4.4.2 Fracture tests with Residual stress

The C(T) specimens considered hereafter were all side-grooved. In the finite element analysis, the cylindrical punches were modeled as rigid surfaces, and a friction coefficient of 0.001 (almost frictionless) between the punch and the specimen surface was used. The rigid punch was given a displacement slowly normal to the side surface of the C(T) specimen and after the reaction force reached the level of the applied load, the punch was removed from the specimen surface.

1) Tensile residual stress

Two levels of compression forces, 182 kN and 220 kN, were used in the experiments to generate tensile residual stresses. The average total indentation depths (after the punches were removed) were 0.083 mm and 0.244 mm for 182 kN and 220 kN respectively. The finite element analyses resulted in 0.089 mm and 0.259 mm total indentation depths for these two cases.

Since the LOPC method creates residual stress field by introducing plastic strain into structure, too much side compression may results in the crack extension. Several methods, such as dye injection and SEM observation of the fracture surface, were used to verify if this has happened. From result of the dye and also SEM observations, the tensile residual side compression did result in crack initiation and growth when 220 kN load was applied. SEM observations also showed clear damage i.e. inclusions broken and pulled loose from the matrix. However, this was not observed for the 182 kN case.

The simulation results for both cases confirmed the experimental observations. Figure 4.15 shows the crack front region after side compression, suggesting crack did extend about 1.5 mm when 220 kN of compression force was employed, whereas crack extension did not happen when 182 kN compression force was applied.

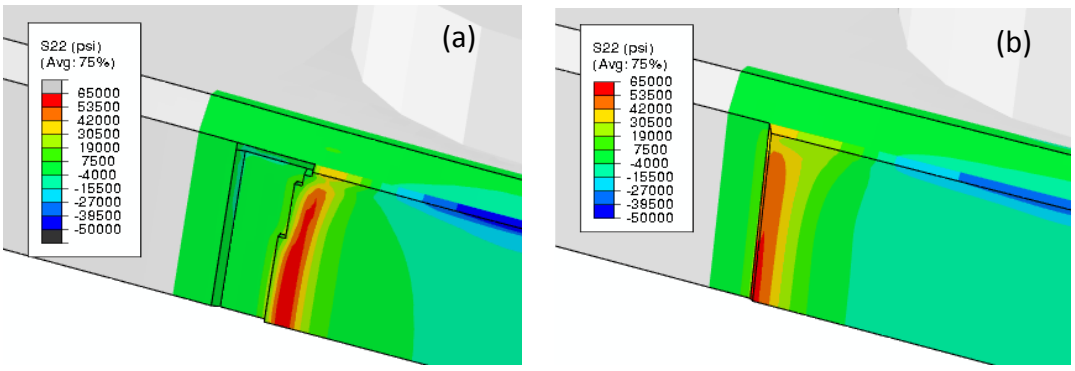

Figure 4. 15 Contour plots of the residual stress normal to the crack plane: (a) 220 kN side-compression, (b) 182 kN side-compression (stress unit in psi)

The contours of residual stresses normal to the crack plane for both cases are shown in Figure 4.15. The high positive residual stress was confined in a small region close to the crack tip, within about 1.3 mm from the crack tip, and the residual stress distribution was fairly uniform along the crack tip except in the region close to the free surface. Figure 4.16 displays the variation of the residual stress (σ_{22}) ahead of the crack front, showing that the residual stress decayed as the distance from crack tip increased. As can be seen, 220 kN side compression generated only slightly larger residual stress than 182 kN side compression did and the residual stress at the mid-plane was larger than at the specimen edge. Since the purpose was to study the residual stress effect on the fracture toughness, appropriate values of the compression force were used so that the unwanted crack growth during side the compression process was avoided.

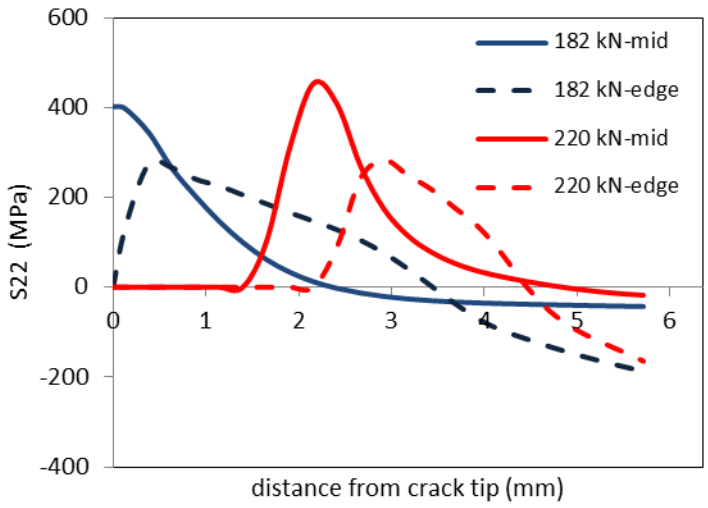

Figure 4. 16 Residual stresses (σ_{22}) distributions ahead of the crack tip at the mid-plane and the specimen edge

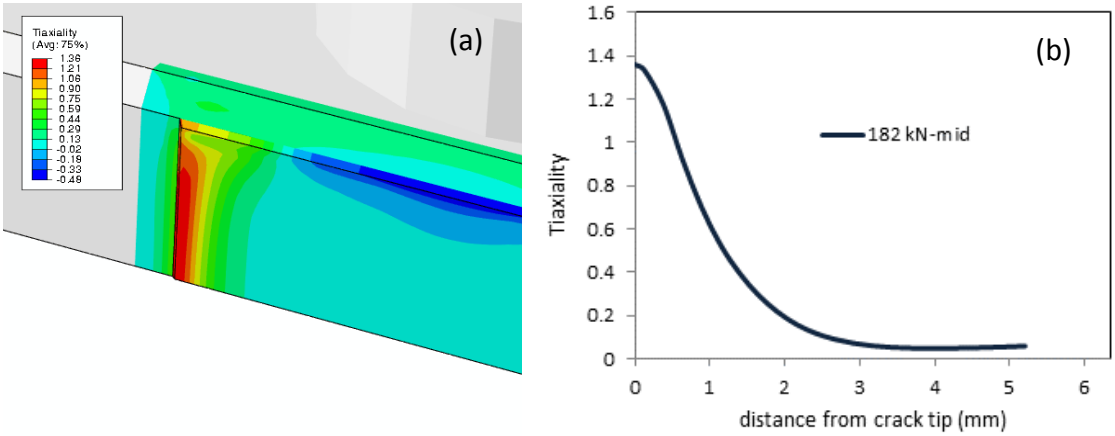

Figure 4. 17 Triaxiality distribution under 182 kN LOPC (tensile residual stress)

Tensile residual stress not only raises the crack driving force but also introduce additional crack-tip constraint [91, 92]. Figure 4.17(a) shows the distribution of triaxiality in the crack front region under 182 kN LOPC force and Figure 4.17(b) shows the variation of the triaxiality ahead of the crack at the mid-plane.

After the residual stress fields have been generated in the specimens, finite element analyses of the compact tension tests of these specimens were carried out. Figure 4.18 compares the model predicted load-displacement curves with experimental records for the as-received specimen as well as the specimens with tensile residual stress field. The numerical model captured the effect of the tensile residual stress on the fracture resistance. The existence of tensile residual stress drastically reduced the fracture resistance and lowered the specimen's load carrying capacity. After crack grew away from the residual stress influence area, the features of crack growth became similar to those exhibited by the virgin specimen.

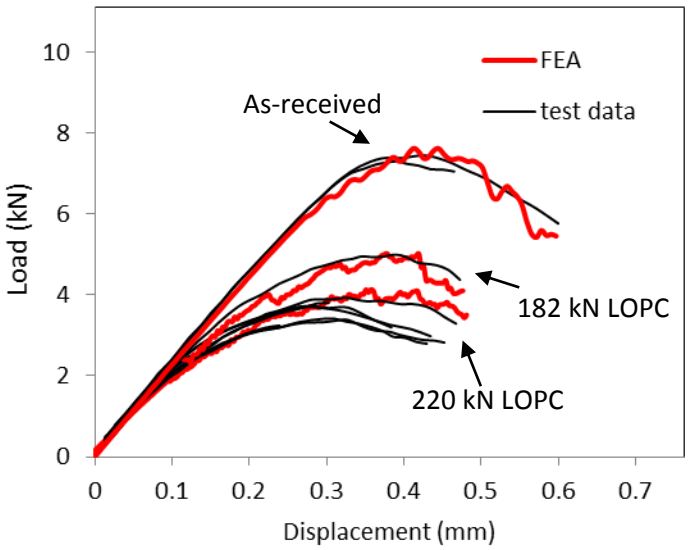

Figure 4. 18 Comparisons of the computed and measured load-displacement curves for C(T) specimen without residual stress and with tensile residual stress

2) Compressive residual stress

When side-compression was applied behind the crack tip, crack closed and the crack surfaces contacted each other. In finite element analysis, to prevent crack surface

penetration, a rigid surface was added to the symmetric plane behind the crack tip. The finite element analysis results showed that the high compressive residual stress region was at the initial EDM notch (behind the fatigue pre-crack front) and the residual stress distribution was not as uniform as tensile residual stress case, Figure 4.19 (a). Figure 4.19 (b) and (c) show the variations of the residual stress (σ_{22}) and the triaxiality with the distance in the crack growth direction (the crack tip is at x = 0) at the mid-plane respectively.

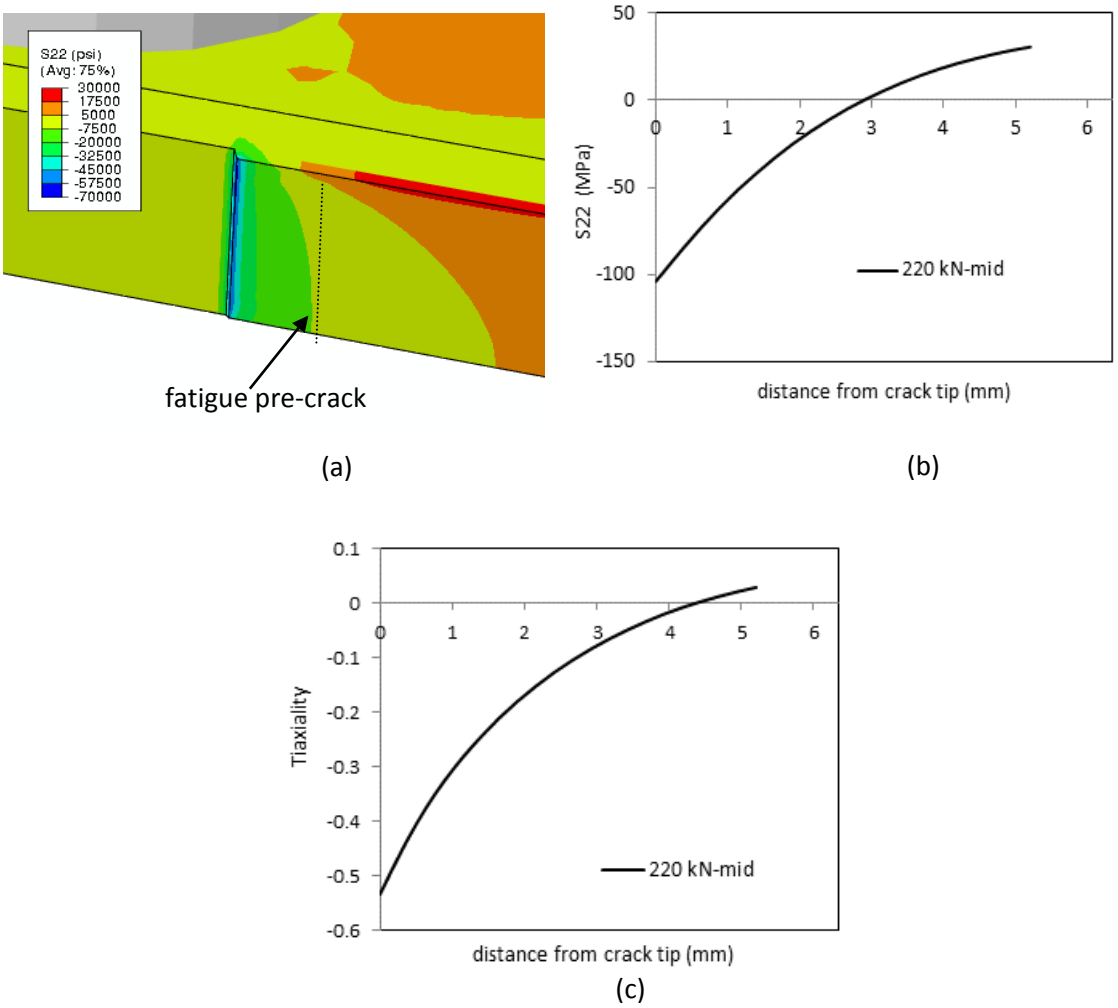

Figure 4. 19 (a) Contour plot of the residual stress normal to the crack plane; (b)&(c) variation of the residual stress (σ_{22}) and the triaxiality with the distance in the crack growth direction respectively (compressive residual stress)

Compressive residual stresses reduced the constraint level at the crack front region and tent to close the crack. Consequently, the compressive residual stress increased the fracture resistance. Figure 4.20 compares the load-displacement curves of the specimen with compressive residual stress field generated by 220 kN side compression with the as received specimen. Included in the Figure are also comparisons between the model predictions and the experimental measurements. Again, good agreement was observed.

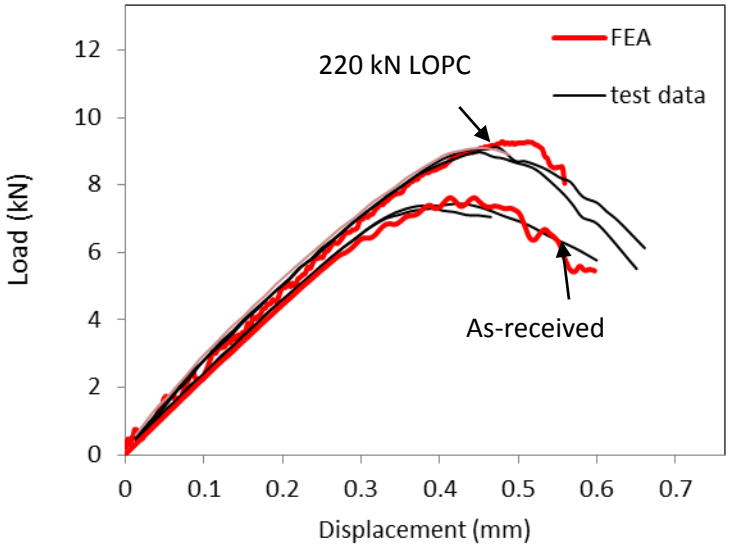

Figure 4. 20 Comparisons of the computed and measured load-displacement curves for C(T) specimen without residual stress and with compressive residual stress.

4.5 Concluding Remarks

In this chapter, the plasticity and ductile fracture behaviors of an AA 5083-H116 were studied through a series of experiments and finite element analyses. This material's plasticity behavior was shown to be J_3 dependent. A J_2-J_3 dependent plasticity model was calibrated and validated by a series of experimental tests and numerical analyses.

Xue-Wierzbicki ductile failure criterion based on the damage parameter defined in terms of the accumulative plastic strain as a function of the stress triaxiality and the Lode angle was implemented and the detailed model calibration process was described. With the calibrated model parameters, the 3D fracture locus was plotted in the space of stress triaxiality and Lode parameter. For this material, increasing stress triaxiality greatly reduced the failure strain while change in Lode parameter did affect the failure strain but the effect was not as strong. The plasticity and ductile fracture models were shown to have the ability to predict the crack growth in C(T) specimens with and without side-grooves.

In the second part of this investigation, a local out-of-plane compression approach was used to generate residual stress fields in C(T) specimens and these residual stress fields were quantified by finite element modeling of the side compression process. Tensile residual stress not only increased the crack driving force but also raised the constraint level in crack tip region, which resulted in lower fracture resistance. Compressive residual stress had the opposite effect. The numerical results, such as load-displacement curves and crack front profiles, were compared with experimental measurements and good agreements were observed. The presented fracture model can be further extended to predict the fracture behavior of welded structures where the residual stress field can be included in the analysis using the eigenstrain method.

CHAPTER V

AN EXTENDED GTN MODEL

In this chapter, a new extended GTN model is proposed by combining the damage mechanics concept of Lemaitre and Lippmann [52] with the GTN void growth model. In this model, two damage parameters, the volumetric damage (void volume fraction) and the shear damage, were coupled into the yield function and flow potential. The evolution law for void volume fraction remained the same as in the original GTN model and a new shear damage evolution law was proposed. Separate localization criterion was introduced for volumetric damage and shear damage and material failure was said to have occurred if the total damage parameter (a combination of volumetric damage and shear damage) reached one.

The extended model is presented after the discussions of the drawbacks of the existing models. The effectiveness of the new model was illustrated through a series of numerical tests that compared its performance with existing models in the literature. Next, the new model was applied to predict the ductile fracture behavior of a beta-treated Zircaloy-4, where the elastic-plastic response of the undamaged material exhibited tension-compression asymmetry and was described by a recently developed J_2-J_3 model (Zhai et al., 2013). The material constants involved in the model were determined based on the experimental observations reported by Cockeram and Chan [93, 94] as well as model calibrations using experimental data reported in Zhai et al., [95]. The predicted

failure initiation and propagation behavior and load-displacement response of specimens experiencing a wide range of stress states were compared with experiments.

5.1 Micromechanical ductile failure models

In this section, the drawbacks of the existing models are discussed first. A new extended GTN model is subsequently proposed in order to overcome these drawbacks.

5.1.1 Drawbacks of the existing models

As described in Chapter 2, the GTN model is incapable of predicting damage under low triaxiality where shear dominates. Xue [36] and Nahshon and Hutchinson [37] proposed similar idea of modification in the GTN model to incorporate the shear-induced damage. Although the above models have shown improvements in the prediction of shear dominated failure at zero or low, positive triaxiality stress states, it has been observed that these models have inherent drawbacks [96, 97]. In particular for combined stress states, the prediction of the location of fracture, the displacement to fracture, and the equivalent plastic strain to fracture were not representative of experimental results. As discussed by Nielsen and Tvergaard [96], the additional damage contribution due to the shear modification might have too strong effect in some cases where the stress triaxiality was not low. This forced them to modify the k_ω parameter in the Nahshon and Hutchinson model as a function of the triaxiality. Nielsen and Tvergaard [38] resolved this issue through modifications of the k_ω parameter in the Nahshon-Hutchinson model to be a function of the triaxiality. This modification defined no shear damage when the triaxiality exceeded a cutoff value.

For convenience, their yield function and void/shear damage evolution law are restated here, and nucleation is not included for simplicity.

Original GTN model:

$$\Phi = \left(\frac{\sigma_e}{\sigma_M}\right)^2 + 2q_1 f \cosh\left(\frac{q_2}{2}\frac{\sigma_{kk}}{\sigma_M}\right) - 1 - \left(q_1 f\right)^2 = 0, \tag{5.1}$$

$$\dot{f} = \dot{f}_g = \left(1 - f\right)\dot{\varepsilon}_{kk}^p, \tag{5.2}$$

Yield function used in the Nahshon-Hutchinson model can be written as same form as in the Xue model

$$\Phi = \left(\frac{\sigma_e}{\sigma_M}\right)^2 + 2D \cosh\left(\frac{q_2}{2}\frac{\sigma_{kk}}{\sigma_M}\right) - 1 - D^2 = 0, \tag{5.3}$$

where damage evolution law is defined as (5.4a) in the Nahshon-Hutchinson model and (5.4b) in the Xue model, and (5.4c) show the Lode angle dependent functions

$$\dot{D} = q_1\left(\dot{f}_g + \dot{f}_s\right), \quad \dot{f}_s = k_\omega f \omega\left(\sigma_{ij}\right)\frac{\sigma_{ij}\dot{\varepsilon}_{ij}^p}{\sigma_e}, \tag{5.4a}$$

$$\dot{D} = q_1 \dot{f}_g + \dot{D}_s, \quad \dot{D}_s = q_3 f^{q_4} g\left(\theta\right)\varepsilon_M^p \dot{\varepsilon}_M^p, \tag{5.4b}$$

$$\omega\left(\sigma_{ij}\right) = 1 - \left[\cos\left(3\theta + \pi/2\right)\right]^2, \quad g\left(\theta\right) = 1 - \frac{6\left|\theta\right|}{\pi}. \tag{5.4c}$$

The limitations of the existing models are attributed to the following reasons:

1) Use of a unified single damage parameter in the yield function

In the original Gurson model, the void coupled yield function was derived from the void deformation behavior in a matrix material. Therefore *f* represented the physical

void volume fraction, and the plastic volume change of the material was due to the void size change. This basis was kept when the Gurson model was extended to the GTN model. The incorporation of shear damage in the modified model was accomplished through the introduction of an additional term in the evolution equation of void volume fraction. This term does not represent a physical value of the porosity but ensures the detrimental effect of void distortion and inter-void linking, associated with the low stress triaxiality. Since only one scalar damage variable measures the total accumulation of different types of damage in the material in an average sense, it should not be used as same as *f*, the void volume fraction.

Shear damage, such as void distortion and inter-void linking, alters the shear loading capacity. However, it is questionable that shear damage has the same significant effects on plastic flow under hydrostatic tension as porosity has. Furthermore, the plastic volumetric strains predicted by Eq. (5.3) are too large compared to the original GTN model when D_s is high.

Assuming an incompressible matrix material and the associated flow rule, the plastic volume change can be obtained as

$$\dot{\varepsilon}_{kk}^{p} = \dot{\lambda}\, 3D \frac{q_2}{\sigma_M} \sinh\left(\frac{q_2}{2}\frac{\sigma_{kk}}{\sigma_M}\right), \tag{5.5}$$

The plastic multiplier $\dot{\lambda}$ can be derived from the consistency condition, and the void growth rate is determined by Eq. (5.2).

From the above equations, shear damage contributes to the plastic volume change, and therefore the void growth rate. This results in significant overestimates of volume

change predictions, which in turn lead to overestimates of void growth. This implicit coupling serves as one of the main reasons for the over-predicted damage under high triaxiality.

The models also result in unrealistic plastic volume change especially when the stress history is complex. For example, if the material has an initial porosity f_0 and is first subjected to a pure shear loading, the shear damage D_s will increase but the total volume will remain unchanged. If the material is then subjected to a pressure loading, the volume will immediately shrink at a rate above the rate suggested by the initial void volume fracture. The total volume can shrink beyond $(1-f_0)V_0$ because $D > 0$ at $f = 0$, Eq. (5.5), where V_0 represents the initial volume.

The above discussion suggests that the two failure mechanisms, volumetric damage and shear damage, cannot be adequately described using a single damage parameter in the yield function.

2) The Lode angle dependency

A Lode angle dependent function is used to distinguish the axisymmetric tension state and the pure shear state. The original GTN model provides good prediction at high triaxiality and no damage under pure shear, the Lode angle dependent function is taken to be zero for axisymmetric tension and one for pure shear. Xue [36] showed the ability of his modified GTN model to predict cup-cone fracture of the round bar tensile test and slant fracture of a C(T) specimen, indicating the necessity of the inclusion of the Lode angle dependency in the model.

However, the Lode angle dependent functions used in the existing models preclude failure at generalized tension or generalized compression with zero pressure. From the viewpoint of void ligament reduction, at these stress states, the shortest ligament distance can also be reduced under proportional loading without void volume change. Therefore, the Lode angle function needs to have a non-zero value to predict failure under zero or negative triaxiality.

3) The void volume dependency

If shear damage is related to void linkage and void distortion, the void size will play an important role in the shear damage accumulation. As discussed above, the void volume can have a pronounced effect on the accumulation of shear damage. The simple linear relationship between shear damage and void volume fraction used by Nahshon and Hutchinson might not be enough. This could be another reason why the Nahshon-Hutchinson model over-predicts the shear damage under high triaxiality. The power parameter q_4 used by Xue gives a better way to tackle this issue. Since the unit cell analysis made by Xue to determine q_4 may not be valid in reality, q_4 can be relaxed to a free parameter.

On the other hand, under low or negative triaxiality, the void volume is rather small or even tends to reduce, and the mechanism of shear interaction with voids is questionable. In fact, the formation of shear localization does not require the existence of voids. Any form of weakness can serve as the perturbation to trigger localization. For simplicity, it might be better to treat shear damage as not related to void volume fraction, in order to predict damage under negative triaxiality.

5.1.2 The proposed model

To overcome the above drawbacks, we proposed a new, extended GTN model. By combining the damage mechanics concept of Lemeitre and Lippmann [52] with the Gurson-type void growth model, shear damage in the new model only affects the deviatoric stress while the only cause of the plastic volume change is the porosity.

1) A new yield function with two damage parameters

In Lemaitre's damage mechanics model [52], one scalar damage parameter D is defined to represent the general loss of load bearing area, which is coupled in the plasticity model. The loss of load carrying capacity due to damage is reflected in both the yield function and the elastic stiffness. In the yield function, the effective stress is scaled by 1/(1-D), i.e., $\Phi = \frac{\sigma_e}{1-D} - \sigma_M$. When D equals unity, the material is said to have completely failed.

In the original GTN model, Eq. (1), if no pressure (hydrostatic stress) exists, the yield function can be written as

$$\begin{aligned} \Phi &= \left(\frac{\sigma_e}{\sigma_M}\right)^2 + 2q_1 f - 1 - (q_1 f)^2 \\ &= \left(\frac{\sigma_e}{\sigma_M}\right)^2 - (1 - q_1 f)^2 \end{aligned} \tag{5.6}$$

By replacing $q_1 f$ with D, Eq. (5.6) is equivalent to the Lemaitre model. Since f represents the void volume fraction, $q_1 f$ can be considered as a parameter which quantifies the void damage.

Under a deviatoric stress state, shear damage, D_s, accumulates in the material. If we assume the shear damage only affects the deviatoric stress, and the total damage is the combination of void damage and shear damage, we can add a D_s term in Eq. (5.6). Therefore, the yield function without pressure can be modified as

$$\begin{aligned}\Phi &= \left(\frac{\sigma_e}{\sigma_M}\right)^2 - \left(1 - q_1 f - D_s\right)^2 \\ &= \left(\frac{\sigma_e}{\sigma_M}\right)^2 + 2q_1 f + 2D_s - \left[1 + \left(q_1 f + D_s\right)^2\right]\end{aligned} \tag{5.7}$$

Under a general stress state, a void will grow due to hydrostatic stress. Assuming the softening effect due to void growth takes the same form as given in the original GTN model, the yield function of a new, extended GTN model can be expressed as

$$\Phi = \left(\frac{\sigma_e}{\sigma_M}\right)^2 + 2q_1 f \cosh\left(\frac{q_2}{2}\frac{\sigma_{kk}}{\sigma_M}\right) - \left[1 + \left(q_1 f + D_s\right)^2 - 2D_s\right] = 0, \tag{5.8}$$

When the total damage ($q_1 f$ + D_s) becomes unity, the material loses its load carrying capacity completely. The new model degenerates to the GTN model when no shear damage exists.

This new model separates contributions from the two failure mechanisms, *i.e.*, volumetric damage and shear damage. Shear damage provides a softening effect that shrinks the deviatoric yield surface and does not affect the volumetric plastic prediction. Volumetric deformation is affected by the porosity in the same way as in the original GTN model.

2) The shear damage evolution law

The shear damage evolution law, which features potential contributions from several failure mechanisms, might be fairly complex and the preliminary studies conducted by the authors attempted to balance the accuracy of the model and the number of material parameters to be calibrated. A quantitative relationship between void size and shear damage has not been firmly established since shear localization can occur with or without the existence of voids. In the material considered in this study (Zircaloy-4), we assumed that shear damage was not directly linked to the void volume fraction, and regarded void growth as merely one of the sources that weakened the material under shear loading.

The shear damage was taken to be a function of plastic strain and stress state. Let ε_f^s be the failure strain under the pure shear state, a shear damage parameter can be defined by a power function as below

$$D_s = \left(\frac{\varepsilon_M^p}{\varepsilon_f^s} \right)^n \tag{5.9}$$

where ε_M^p represents the matrix plastic strain and n is a constant larger than one. D_s is equal to one when ε_M^p reaches to ε_f^s. With n is greater than one, the softening effect is small at the early stage of plastic deformation and becomes larger as the material approaches failure. The incremental form of shear damage can be expressed as

$$\dot{D}_s = \frac{n D_s^{\frac{n-1}{n}}}{\varepsilon_f^s} \dot{\varepsilon}_M^p \tag{5.10}$$

To extend Eq. (5.10) to any arbitrary stress state, a function of triaxiality T^* and Lode angle was introduced as a weight factor

$$\dot{D}_s = \psi\left(\theta, T^*\right) \frac{n\, D_s^{\frac{n-1}{n}}}{\varepsilon_f^s} \dot{\varepsilon}_M^p \tag{5.11}$$

where the weight function $\psi\left(\theta, T^*\right)$ must have unit value under pure shear state. To our knowledge, there is no generally accepted form of this function at present. In this study, the weight function was taken to be the same as the $g(\theta)$ function used in the Xue model [36] for positive stress triaxiality (Eq. (5.4c)). A modification was made to provide the ability of predicting shear damage as $\theta = \pm\pi/6$ with negative stress triaxiality

$$\psi\left(\theta, T^*\right) = \begin{cases} g(\theta) & T^* > 0 \\ g(\theta)(1-k)+k & T^* \le 0 \end{cases} \tag{5.12}$$

where the constant *k* in (5.12) represents the value of the weight factor when the stress triaxiality is negative and $\theta = \pm\pi/6$, which can be calibrated using axisymmetric compression test data. In the Xue model and the Nahshon-Hutchinson model, shear damage was indirectly related to the stress triaxiality through the void volume fraction dependency. For the material (Zircaloy-4) considered in this study, it was found that Eq. (5.12) provided an adequate description of the stress state effect on shear damage. While the rather simplified form of the weight function given by Eq. (5.12) worked reasonably well for the material considered in this study by being able to capture the damage evolution process in various specimens and reproduce the experimental data, further investigation needs to be dedicated to explore different forms of the $\psi\left(\theta, T^*\right)$ function.

3) Evolution of volumetric damage

The volumetric damage is due to the increase of void volume. The evolution equation for void volume fraction is the same as in the original GTN model described in Section 5.1.1.

4) Separate criteria for initiation of localization caused by the two types of damage

The criterion for onset of localization plays a significant role in the prediction of failure initiation and propagation. After the onset of localization, damage increases rapidly and the softening process accelerates so that material loses its load carrying capacity quickly. The f^*-function described in Chapter 2.3 is a simple way to deal with the localization caused by void volume increase.

For the two kinds of damage discussed above, when triaxiality is high, volumetric damage (increase of void volume) triggers localization, but when triaxiality is low, shear damage often triggers localization (shear band). For example, in a round, tensile bar, the stress triaxiality is high at the center and low at the specimen surface. Void volume increase leads to material failure at the center, and shear damage causes material failure near the specimen surface, resulting in a cup-cone fracture surface. Consequently, a separate localization criterion can be established for each of the two damage mechanisms. Under the situation that void damage grows faster than shear damage, the porosity reaches the critical value first and triggers localization, and vice versa. The competition between the two localization mechanisms, influenced significantly by the stress state, results in a different mode of fracture and different appearance of the fracture surface.

In this study, localization caused by void damage was modeled the same way as described in Chapter 2.3 using the f^*-function. The shear damage evolution law was selected so that the localization effect was already reflected. For common ductile metals and alloys, the softening induced by shear damage increases slowly when the plastic strain is small and accelerates when ε_M^p approaches ε_f^s, so the *n*-power in the shear damage definition is usually greater than 4. The parameters ε_f^s and *n* determines shear localization.

5) Summarization of the extended GTN model

The following equations summarize our extended GTN model

$$\Phi = \left(\frac{\sigma_e}{\sigma_M}\right)^2 + 2q_1 f^* \cosh\left(\frac{q_2}{2}\frac{\sigma_{kk}}{\sigma_M}\right) - \left[1 + \left(q_1 f^* + D_s\right)^2 - 2D_s\right] = 0;$$

$$\dot{\varepsilon}_{ij}^p = \dot{\lambda} n_{ij};\ \ n_{ij} = \frac{\partial \Phi}{\partial \sigma_{ij}}$$

$$\dot{f} = \dot{f}_g + \dot{f}_n; \qquad \dot{f}_g = (1-f)\dot{\varepsilon}_{kk}^p; \qquad \dot{f}_n = A_N \dot{\varepsilon}_M^p;$$

$$A_N = \frac{f_n}{S_n\sqrt{2\pi}} \exp\left[-\frac{1}{2}\left(\frac{\varepsilon_M^p - \varepsilon_n}{S_n}\right)^2\right];$$

$$f^* = \begin{cases} f & \text{for } f \le f_c \\ f_c + \dfrac{1/q_1 - f_c}{f_f - f_c}(f - f_c) & \text{for } f_c \le f \le f_f \end{cases}; \qquad (5.14)$$

$$\dot{D}_s = \psi(\theta, T^*)\frac{n\, D_s^{\frac{n-1}{n}}}{\varepsilon_f^s}\dot{\varepsilon}_M^p;$$

$$D = q_1 f^* + D_s; \qquad \sigma_M \dot{\varepsilon}_M^p = (1 - D/q_1)\sigma_{ij}\dot{\varepsilon}_{ij}^p.$$

where D is the total damage parameter. When D reaches unity, the material is said to have completely failed.

6) Matrix plasticity behavior

For an isotropic material in general, the yield function and flow potential should be functions of the hydrostatic stress as well as the second and third invariant of the deviatoric stress tensor, J_2 and J_3 ([69] and references therein). If the material exhibits no pressure sensitivity or Lode dependency, the J_2 flow theory is usually used to describe the plastic response. In the original GTN model, the matrix plasticity behavior follows the J_2 flow plasticity theory, where the equivalent stress σ_e is the von Mises stress defined as $\sigma_e = \sqrt{3J_2}$.

5.2 Single Material Point Test

To illustrate the effect of the modifications presented above on the predicted material behavior, a series of numerical tests were conducted and the results were compared with the original GTN model as well as the Xue model and Nahshon-Hutchinson model.

5.2.1 Analysis procedure

For proportional loading histories, the stress tensor can be represented by a load proportionality factor $\tilde{\sigma}$ multiplied by a constant tensor R_{ij}. The designated stress triaxiality and Lode parameter can be obtained by choosing appropriate R_{ij} values.

A load-controlled process using $\tilde{\sigma}$ as the loading parameter is difficult to achieve because of the softening effect. Instead, an algorithm was developed to apply the plastic multiplier incrementally and compute $\tilde{\sigma}$ and the internal variables ε_M^p, f and D_s at each step accordingly.

To illustrate this process, we started with the consistency condition

$$\dot{\Phi} = \frac{\partial \Phi}{\partial \sigma_{ij}} \dot{\sigma}_{ij} + \frac{\partial \Phi}{\partial \sigma_M} \frac{\partial \sigma_M}{\partial \varepsilon_M^p} \dot{\varepsilon}_M^p + \frac{\partial \Phi}{\partial f^*} \frac{\partial f^*}{\partial f} \dot{f} + \frac{\partial \Phi}{\partial D_s} \dot{D}_s = 0 \tag{5.15}$$

where the rates of internal variables ε_M^p, f and D_s can be written as functions of $\dot{\lambda}$. Substituting $\dot{\varepsilon}_M^p$, $\dot{f}$ and $\dot{D}_s$ in (5.15) results in

$$\dot{\lambda} = \frac{1}{H} \frac{\partial \Phi}{\partial \sigma_{ij}} \dot{\sigma}_{ij} \tag{5.16}$$

where H is the hardening modulus

$$H = -\left(\frac{\partial \sigma_M}{\partial \varepsilon_M^p} \frac{\partial \Phi}{\partial \sigma_M} \frac{\partial \varepsilon_M^p}{\partial \lambda} + \frac{\partial \Phi}{\partial f^*} \frac{\partial f^*}{\partial f} \frac{\partial f}{\partial \lambda} + \frac{\partial \Phi}{\partial D_s} \frac{\partial D_s}{\partial \lambda} \right) \tag{5.17}$$

For a given stress state where the ratios between stress components are fixed, Eq. (5.16) can be written as (5.18a) and the increment of $\tilde{\sigma}$ can be obtained by (5.18b)

$$\dot{\lambda} = \frac{\dot{\tilde{\sigma}}}{H} \frac{\partial \Phi}{\partial \sigma_{ij}} R_{ij} \qquad \text{(a)}$$

$$\dot{\tilde{\sigma}} = \frac{H}{\dfrac{\partial \Phi}{\partial \sigma_{ij}} R_{ij}} \dot{\lambda} \qquad \text{(b)} \tag{5.18}$$

Eq. (5.18b) can be solved numerically. This was done in MATLAB using a forward Euler integration scheme. The increment size was reduced until the solution was converged. The initial values of $\tilde{\sigma}$ at the onset of plastic deformation ($\lambda = 0$) were solved from Eq. (5.8).

The details of the procedures described above to maintain the stress triaxiality and the Lode parameter at constant values during the loading history are given in Appendix A.

5.2.2 Numerical examples

In the numerical examples presented in this Section, the matrix material was assumed to follow the J_2 flow plasticity theory and obey a power-law hardening, true stress-strain relation

$$\begin{cases} \varepsilon = \dfrac{\sigma}{E} & \sigma \le \sigma_0 \\ \varepsilon = \dfrac{\sigma_0}{E}\left(\dfrac{\sigma}{\sigma_0}\right)^N & \sigma > \sigma_0 \end{cases} \tag{5.19}$$

Here the material parameters were taken to be $E/\sigma_0 = 300$ and $N = 0.1$, where E, σ_0 and N represent the Young's modulus, yield stress and hardening exponent respectively. The damage related parameters for extended GTN model are listed in Table 5.1, with no consideration of void nucleation.

Table 5.1 Model parameters for extended GTN model used in the single material point analyses

					ε_f^s	n	k
1.5 (q_1)	1 (q_2)	0.005 (f_0)	0.1 (f_c)	0.25 (f_f)	1.4	5	0.7

For comparisons among the current model and the Xue model, the Nahshon-Hutchinson model, and the original GTN model, the same matrix material constants and volumetric damage parameters were adopted in the numerical analyses. Specific parameters used to define shear damage contribution in the Xue model and the Nahshon-Hutchinson model were chosen to ensure these models predict similar behaviors as the current model under the pure shear condition. The parameters chosen were $k_\omega = 3$ for the Nahshon-Hutchinson model and q_3 = 1.8 and q_4 =1/3 for the Xue model.

1) Case 1 – Comparison of model predictions under generalized shear loading

For generalized tension (uniaxial tension + hydrostatic stress) where $T^* > 0$ and $\theta = -\pi/6$, there was no difference among predicted results from the four models. However, under generalized shear (pure shear + hydrostatic stress) where $\theta = 0$, the models predicted different behaviors. Here comparisons were made at three levels of stress triaxialities, T^*= 0, 0.7 and 1.2. Figure 5.1 shows the effective stress $\bar{\sigma}$ versus matrix plastic strain ε_M^p response generated by the four models, where the black solid curve represents the result of the current model and the blue, red and green dash lines represent the results of the Xue model, the Nahshon-Hutchinson model and the GTN model respectively.

For the pure shear case ($\theta = 0$, T^*=0) shown in Figure 5.1(a), the predictions of the current model, the Xue model, and the Nahshon-Hutchinson model showed little difference prior to shear localization. These three modified GTN models resulted in similar material softening behavior caused by shear damage. In contrast, the original GTN model did not predict any damage as expected.

The difference between the current model and the other two modified models was apparent as the stress triaxiality increased. Figure 5.1(b) displays the results for T^* =0.7 and Figure 5.1(c) displays the results for T^* =1.2. Results of the Xue model and the Nahshon-Hutchinson model both predicted significantly higher damage than the current model and the GTN model. But as discussed in Chapter 5.1.1, the shear damage corrections introduced in the Xue model and the Nahshon-Hutchinson model were too strong at high triaxiality levels. On the other hand, the predicted softening effect by the current model lied between the results from the original GTN model and the Xue and Nahshon-Hutchinson models. As the triaxiality level increased, the predictions of the current model approached the GTN model. With the new model, shear damage governed the failure behavior when the triaxiality was low. As the triaxiality increased, the dominant failure mechanism shifted to void growth and coalescence. At high triaxiality levels (for T^* >1.2 here), void damage was dominant, and the shear effect was negligible. This also matched findings by numerous researchers that the original GTN model worked well under high stress triaxiality conditions.

Material ductility reduces as the stress triaxiality increases. Figure 5.2 shows the predicted effective stress versus matrix plastic strain responses by the current model at three T^* levels. As T^* increased, the softening behavior became more pronounced and the onset of material failure occurred earlier.

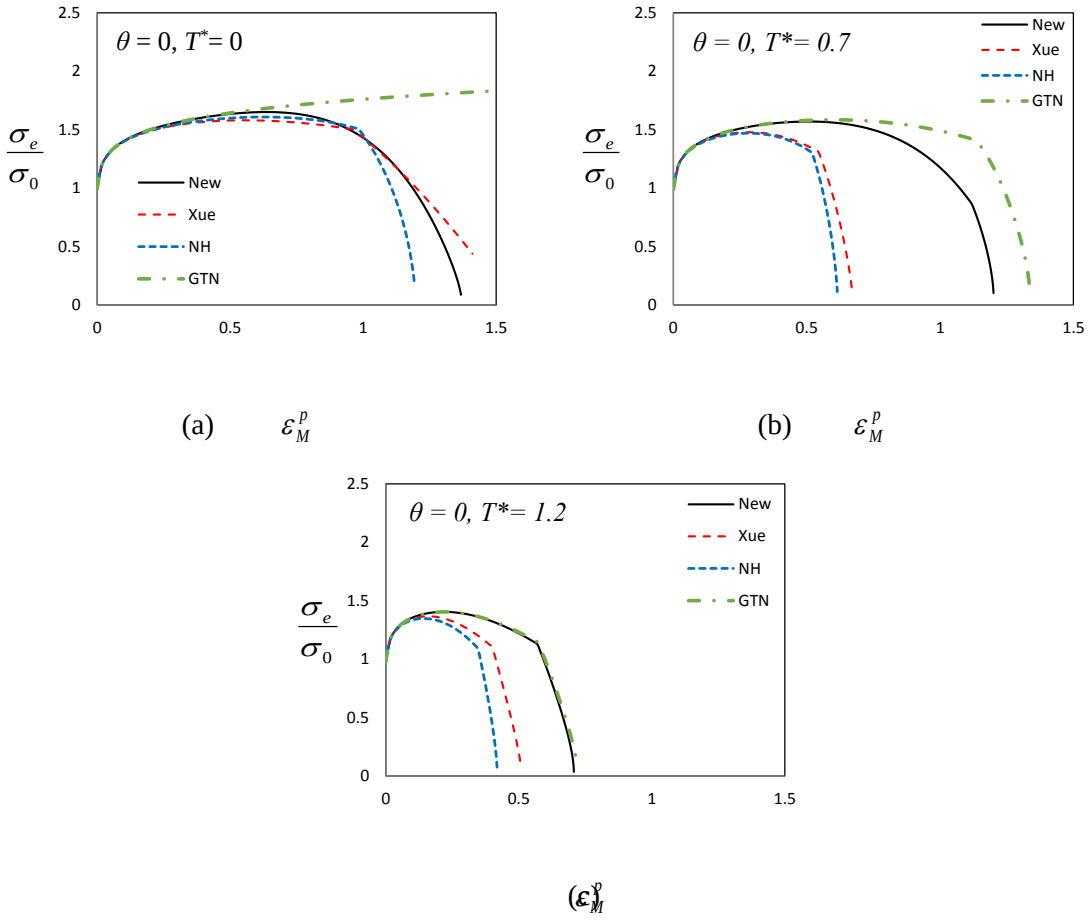

Figure 5. 1 Comparison of the effective stress versus matrix plastic strain response between the current model (New), the Xue model, the Nahshon-Hutchinson model (NH), and the GTN model under generalized shear condition with different stress triaxialities.

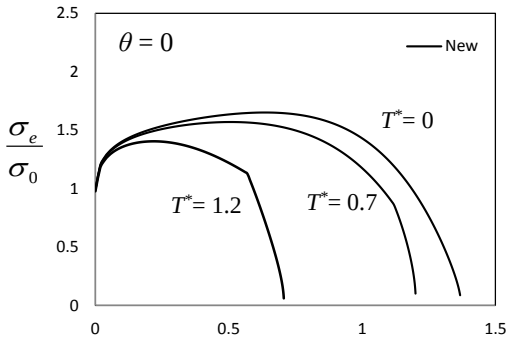

Figure 5. 2 The predicted effective stress versus matrix plastic strain responses by the current model at three T^* levels.

2) Case 2 – Effect of the introduction of two separate damage parameters in the yield function

To illustrate the effect of the introductions of two separate damage parameters in the yield function, we considered a modified Xue model, where the volumetric damage and shear damage parameters present separately in the yield function as shown in Eq. (5.8), and compared the numerical predictions with the original Xue model. Figure 5.3 plots the versus responses under generalized shear (θ = 0) for the T^* = 0, 0.7, and 1.2 cases, where the results of the modified Xue model, the original Xue's model and the GTN model are displayed in black, red and green lines respectively. For pure shear loading (T^* = 0), since the volumetric damage did not grow, the modified Xue model and the original Xue model became the same, Figure 5.3(a). The modified Xue model predicted less softening effect and delayed material failure compared to the original Xue model, Figs 5.3(b) and 3(c). It is worth noting that, unlike the new model developed in this study, the modified Xue model still predicted significant shear damage effect under high stress triaxiality level.

Figure 5.4 compares the void growth rates predicted by the modified Xue model, the original Xue's model and the GTN under θ = 0 and T^* = 0.7, which clearly indicated that the void growth rate predicted by using Eq. (5.8) was much slower than the original Xue model. In particular, the modified Xue model predicted almost the same void growth rate as the GTN model in the early stage of loading while the original Xue model predicted a much accelerated void growth rate.

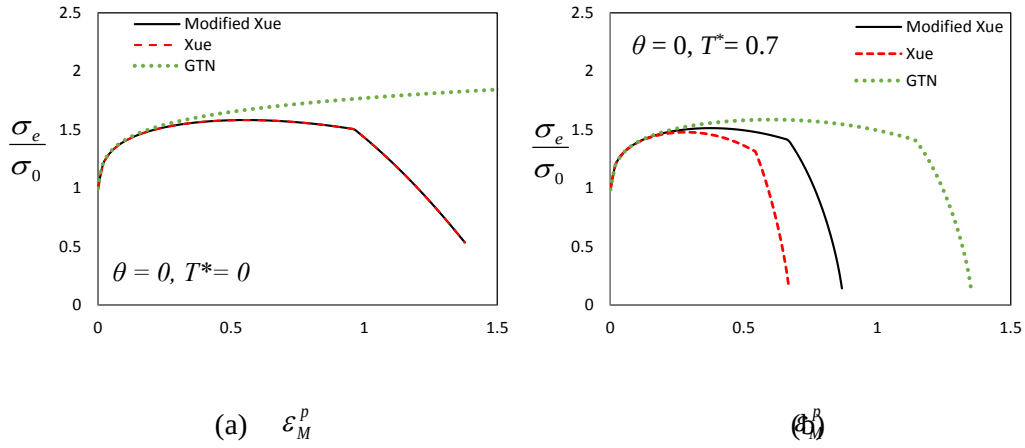

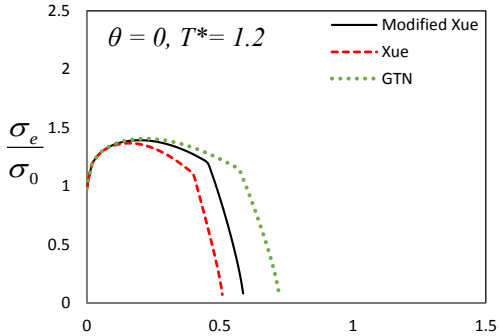

Figure 5. 3 Comparison of the effective stress versus matrix plastic strain response between the modified Xue model and the original Xue model under generalized shear condition with different stress triaxialities.

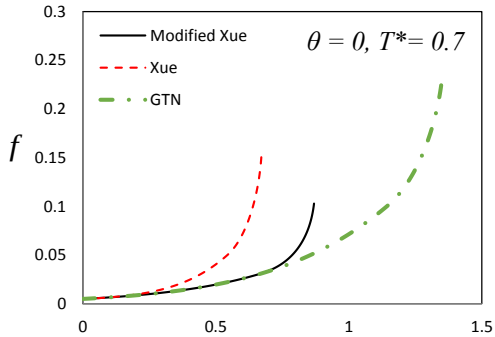

Figure 5. 4 Comparison of the void growth rates predicted by the modified Xue model, the original Xue's model and the GTN under $\theta = 0$ and $T^* = 0.7$.

3) Case 3 – Failure under negative stress triaxiality

Under very low or negative stress triaxiality, the void growth mechanism is suppressed, and shear damage becomes the driver for material failure. This case study illustrated the capability of our proposed model to predict damage and failure under these conditions. The loading conditions considered were for T^*= -1/3 with three different Lode angles: θ = -π/6, θ = -π/12, and θ = 0. The predicted versus and f versus responses are shown in Figure 5.5. The model predicted ductile failure even when the triaxiality was negative and the void tended to close (Figure 5.5(b)). From Figure 5.5(a), the θ = -π/6 case gave the highest failure strain while the θ = 0 gave the lowest failure strain. This difference in the predicted ductile failure behavior was determined by the parameter k introduced in Eq. (5.12).

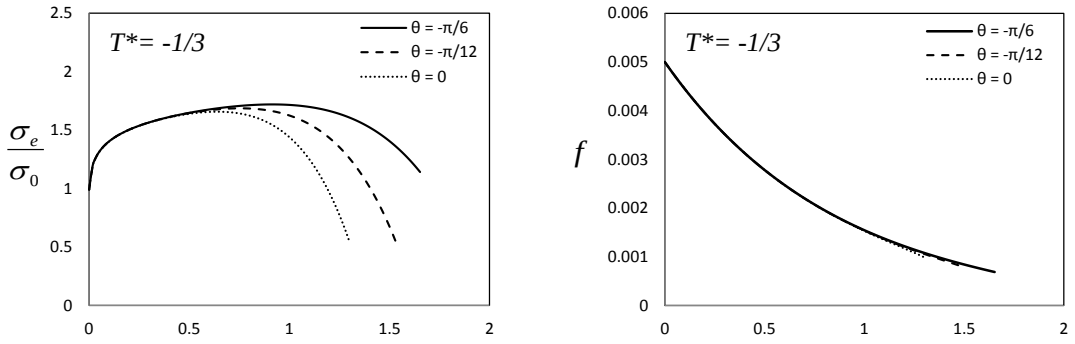

(a) (b)

Figure 5. 5 Predicted effective stress versus matrix plastic strain and void volume fraction versus matrix plastic strain responses under negative stress triaxiality (T^*= -1/3) and different Lode angles.

5.3 Modeling the ductile fracture behavior of a beta-treated Zircaloy-4

In this Section, the newly extended GTN model described above was calibrated for a beta-treated Zircaloy-4 and used to predict damage and fracture of a variety of specimens.

5.3.1 Material

The beta-treated Zircaloy-4 considered in this study is the same material studied by Zhai et al [95] and Zhang et al [98]. The chemical compositions of this material are listed in Table 5.2. All the specimens were extracted from wrought material in the longitudinal direction and tests were conducted at room temperature and quasi-static loading rate. The Zircaloy-4 was heat-treated to produce a random texture on a macroscopic scale and is considered isotropic in this study. The Young's modulus of the material is 99.6 GPa and the Poisson's ratio is 0.34.

Table 5.2 Nominal Chemical Composition of Zircaloy-4 (wt%)

Element	Fe	Sn	Cr	O	Zr
Composition	0.21	1.53	0.11	0.13	Balance

A recent study found out that the matrix plasticity behavior of this material exhibited tension-compression asymmetry and followed a J_2–J_3 dependent plasticity model [95]. According to this model, the definition of equivalent stress was modified as

$$\sigma_e = c_1(3\sqrt{3}J_2^{3/2} + b_1 J_3)^{1/3} \tag{5.20}$$

where b_1 is a function of ε_M^p as defined by Eq. (5.21) and $c_1 = 1/(2b_1/27+1)^{1/3}$

$$b_1 = 2.2 \qquad \text{when} \quad \varepsilon_M^p \le 0.1$$

$$b_1 = 17.3 \times (\varepsilon^p - 0.1) + 2.2 \qquad \text{when} \quad 0.1 < \varepsilon_M^p < 0.2 \tag{5.21}$$

$$b_1 = 4.8 \qquad \text{when} \quad \varepsilon_M^p \ge 0.2$$

Figure 5.6(a) illustrates the yield surface giving by the J_2-J_3 model as the parameter b_1 takes different values. When b_1 is zero, the model becomes identical to the Mises plasticity model. When b_1 is greater than zero, the yield stress in compression will be larger than the yield stress in tension. Figure 5.6 (b) shows the stress strain curve of the matrix material under tension. Details of this plasticity model can be found in [95].

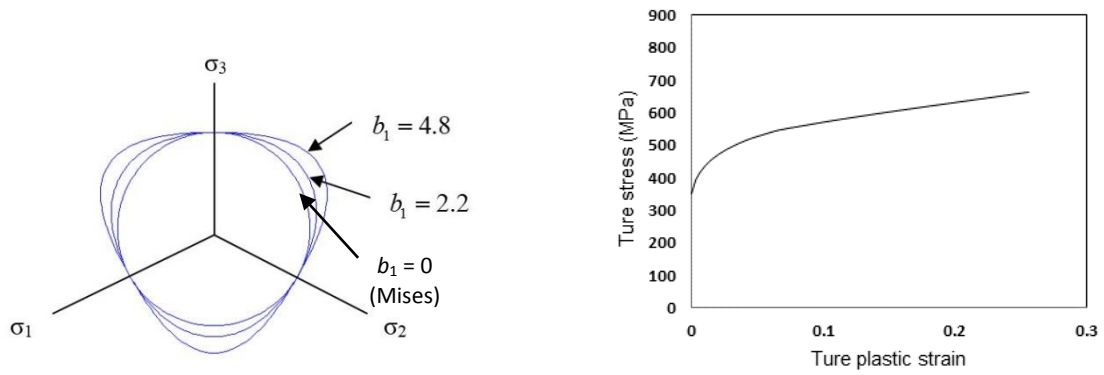

(a) (b)

Figure 5. 6 (a) Yield surface of the matrix material as b_1 takes different values, (b) tensile stress-strain curve.

Cockeram and Chan [94] conducted in-situ experimental studies over a range of positive stress triaxialities on beta-treated Zircaloy-4 and Zircaloy-2. Several important void formation and damage evolution characteristics observed in their experiments were utilized to determine the material constants in the void model. The material was initially void-free. Fracture was observed as a process of void nucleation, growth and coalescence.

The lath boundaries for beta-treated Zircaloy-4 were covered with laves phase particles that are localized sites for void nucleation. Voids were previously observed to nucleate on these precipitates located at lath boundaries. Void nucleation might also occur within the lath at the intersection of slip bands. Void coalescence generally resulted in the formation of larger elongated voids or microcracks. Many lath boundaries were observed to be dotted with rows of micron-sized voids, whose coalescence eventually would lead to the formation of grain boundary microcracks.

The experimental studies by Cockeram and Chan [94] also indicated that the critical local strain at the initiation of void nucleation was almost constant for all the stress states studied. The strain to failure was shown to be controlled by the process of void growth and coalescence that was strongly dependent on stress-state.

In the material modeling, we tried to correlate the void related material constants to the experimental observation. It must be pointed out though, *f* should be regarded as an effective void volume fraction, which was not correlated to the actual void size. The void distribution in the material was highly non-homogenous, mainly located along the lath boundaries in the form of micron-sized voids. In the coalescence process, microcracks were formed from the linkage of these small voids.

The initial void volume, f_0, was set to be zero and void nucleation was assumed to be strain-controlled. Cockeram and Chan [93] found that void nucleation process in the tensile specimens was observed to occur at the UTS and beyond. From the uniaxial tensile tests conducted in this study, the strain value when necking occurs was around 0.1, which can be regarded as the mean strain for void nucleation, ε_n. It was observed that

once the voids were nucleated, little growth was required before the voids coalesce. Therefore, we set the critical porosity f_c to be slightly larger than f_n. Other parameters were calibrated by matching the finite element analysis results to experimental obtained load-displacement response.

5.3.2 Specimens

This study analyzed numerical models of smooth round tensile bars, notched round tensile bars, cylindrical compression specimens, the Lindholm-type torsion specimens subjected to pure torsion and combined torsion-compression, the flat notched tensile specimens, and the flat grooved plane strain tensile specimens. Figure 5.7 shows sketches of these specimens. The experimental results for the testing of these specimens were reported in [95, 98]. The diameter of the gauge section of the smooth round tensile bar was 12.7 mm and the gauge length was 50.8 mm. For the notched round bars, the diameter at the notch section was 7.62 mm, the notched radius was 2.54 mm, and the gauge length was 25.4 mm. The compression specimen had a diameter of 8.0 mm and length/diameter (L/D) ratio of 1.5. The Lindholm-type torsion specimen was a hollow cylinder having an inner diameter of 13.1 mm and outer diameter of 25.4 mm. The gauge section length and wall-thickness were 2.54 mm and 0.7366 mm respectively. Torsion-compression tests were performed with a central pin to prevent inward buckling. The flat notched tensile specimens had a thickness of 2.286 mm and the gauge section length was 12.7 mm. The thickness of the flat grooved plane strain specimen at the groove was 2.032 mm, the radius of the groove was 2.032 mm, the plate thickness at the specimen shoulder was 6.096 mm, and the length of gauge section for this specimen was 12.7 mm.

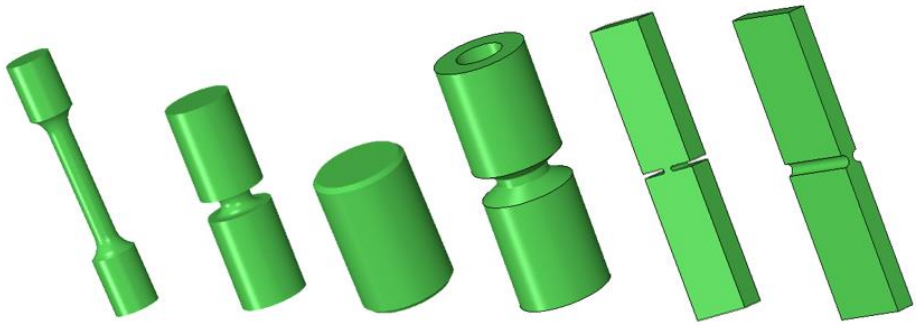

Figure 5. 7 Sketches of a smooth round bar, a notched round bar, a compression specimen, a torsion specimen, a flat notched tensile specimen, and a flat grooved plane strain specimen.

5.3.3 Finite element procedure

ABAQUS/Explicit was used to analyze all the specimens, where the material model was implemented via a user defined subroutine VUMAT. A forward-Euler with correction return scheme for the stress integration, original proposed by Crisfield [99] was adopted. The detailed numerical implementation procedure is given in the Appendix B.

In the finite element analyses, 4-node axisymmetric elements with reduced integration (CAX4R) are used for round tensile specimens and the element size is 63.5 $\mu m \times 63.5$ μm around the mid-plane where failure was expected to occur. Three-dimensional, 8-node brick elements with reduced integration (C3D8R) were used for all other specimens, where similar element size was adopted in critical regions. To improve model efficiency, symmetry conditions were applied whenever available. Figure 5.8 shows typical finite element meshes of a round tensile specimen, a notched round bar tensile specimen, a compression specimen, a torsion specimen, a flat notched tensile specimen, and a flat grooved plane strain tensile specimen. For compression tests, the

compression platen was modeled as a rigid surface, and frictional surface contact modeled the interaction between the platen and the specimen. Since the exact friction coefficient was unknown and difficult to obtain, a value of 0.08 was used in the finite element analysis.

After the fully damaged material loses the ability to sustain hydrostatic tension load and shear load, it still can withstand pressure load. Therefore, special treatment was required after the complete failure of material under compressive stress states. Completely damaged material retains its bulk modulus for compressive hydrostatic loads. This corresponds to a fluid-like behavior. When the failed element under undergoes extremely large deformation, computational efficiency is reduced drastically, the element will be removed.

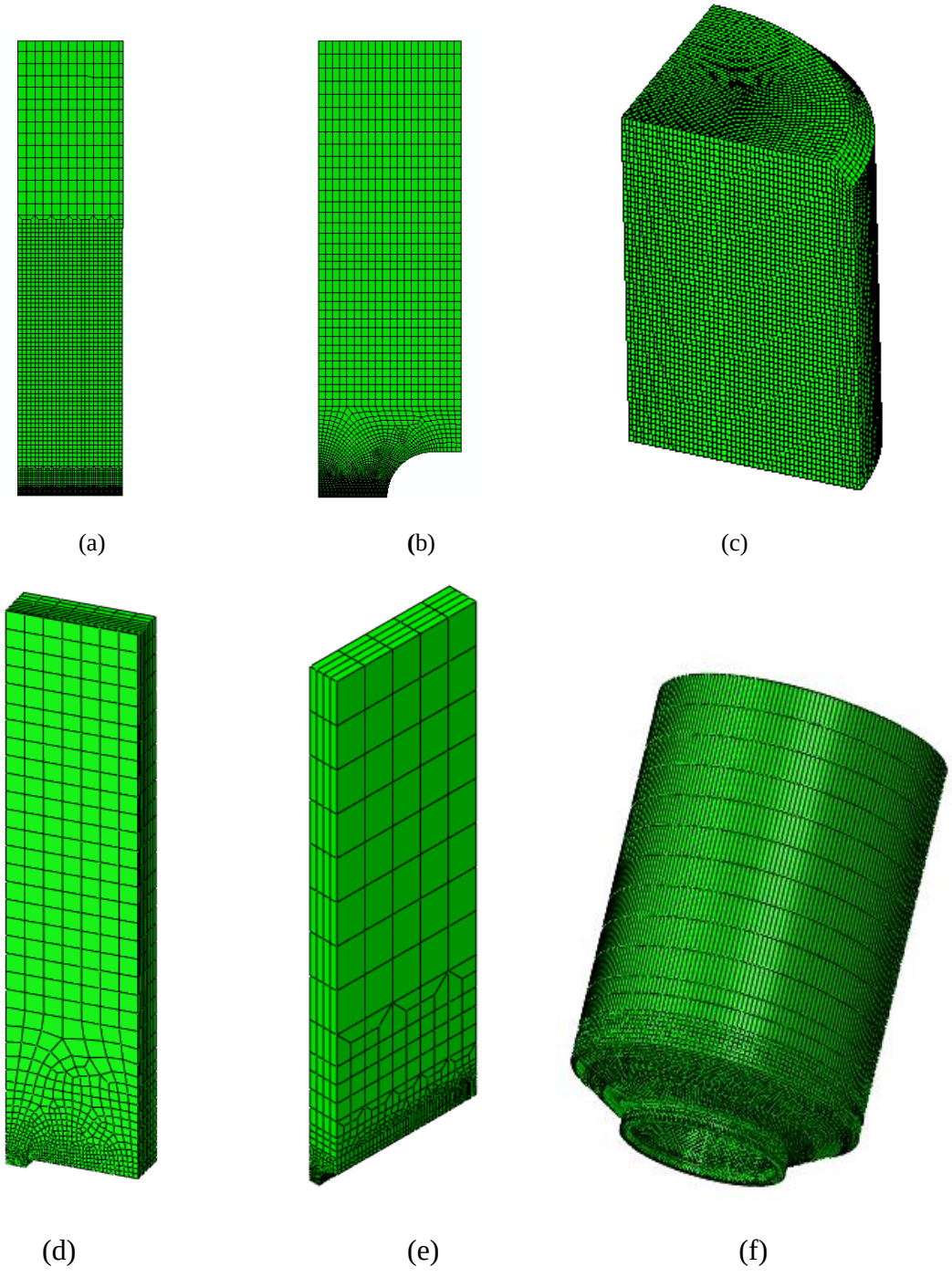

Figure 5. 8 Finite element mesh of (a) a smooth round tensile specimen, (b) a notched round tensile specimen, (c) a compression specimen with L/D = 1.5, (d) a flat notched tensile specimen, (e) a flat grooved plane strain tensile specimen, and (f) a pure torsion specimen.

5.3.4 Results and discussion

1) Model calibration and verification

Model calibration followed a three-step strategy. For specimens where the onset of fracture was dominated by the void damage mechanism, the calibration of void related parameters could be conducted. The shear damage parameters were calibrated using test data where fracture was dominated by shear damage. Finally the parameter *k* in the weight function of the shear damage evolution were calibrated using experimental data obtained from a specimen with negative triaxiality and $g(\theta) \neq 1$.

Table 5.3 lists all calibrated material constants. The values of q_1 and q_2 were the suggested by Tvergaard [54]. Standard deviation of the void nucleation strain, S_n, was chosen to be a relatively small value to produce a rapid void nucleation process. Parameters f_n, f_c, and f_f, were calibrated from the smooth and notched round bar specimens. Effective failure strain under pure shear, ε_f^s, and the shear damage softening parameter *n* were calibrated from the pure torsion test. The value of parameter *k* was calibrated using the compression test data.

Table 5.3 Model parameters for Zircaloy-4

			f_n	S_n	ε_n			ε_f^s	n	k
1.5	1	0	0.012	0.02	0.1	0.03	0.08	0.5	5	0.5

Figure 5.9 provides comparisons of the load vs. displacement and torque vs. twist angle responses among numerical simulations and experimental data for specimens used in the calibrations. Since these specimens were used to fit material parameters, the extended GTN model with the calibrated model parameters predicted the plasticity responses and the onset of fracture very well for all the specimens.

To validate the calibrated model, the flat notched tensile specimen, the flat grooved plane strain tensile specimen and the torsion-compression specimen were analyzed. Figure 5.10 provides comparisons of the load vs. displacement among numerical simulations and experimental data for the flat notched tensile specimen and the flat grooved plane strain tensile specimen respectively. The predictions of the load-displacement response and fracture onset agreed with very well with experimental data.

Figure 5.11 shows comparisons of the load vs. displacement and torque vs. twist angle responses among numerical simulations and experimental data for the torsion-compression specimen. This specimen was under negative triaxiality and the Lode angle was between pure shear and uniaxial compression. The comparison between model prediction and experimental data was reasonably well up until failure initiation. Experimental results showed slowly softening after the peak load was reached which was not accurately captured by our model. There are several potential explanations. The weight function used to describe the stress state effect on shear damage might not be adequate. Alternatively, the newly created free surfaces contact and friction prevented rapid shear sliding. This behavior could provide some resistance to additional loading but was not included in the present model, which responded like a fluid (no shear resistance)

after being fully damaged. These effects may be considered in further studies of fracture under negative triaxiality in the future.

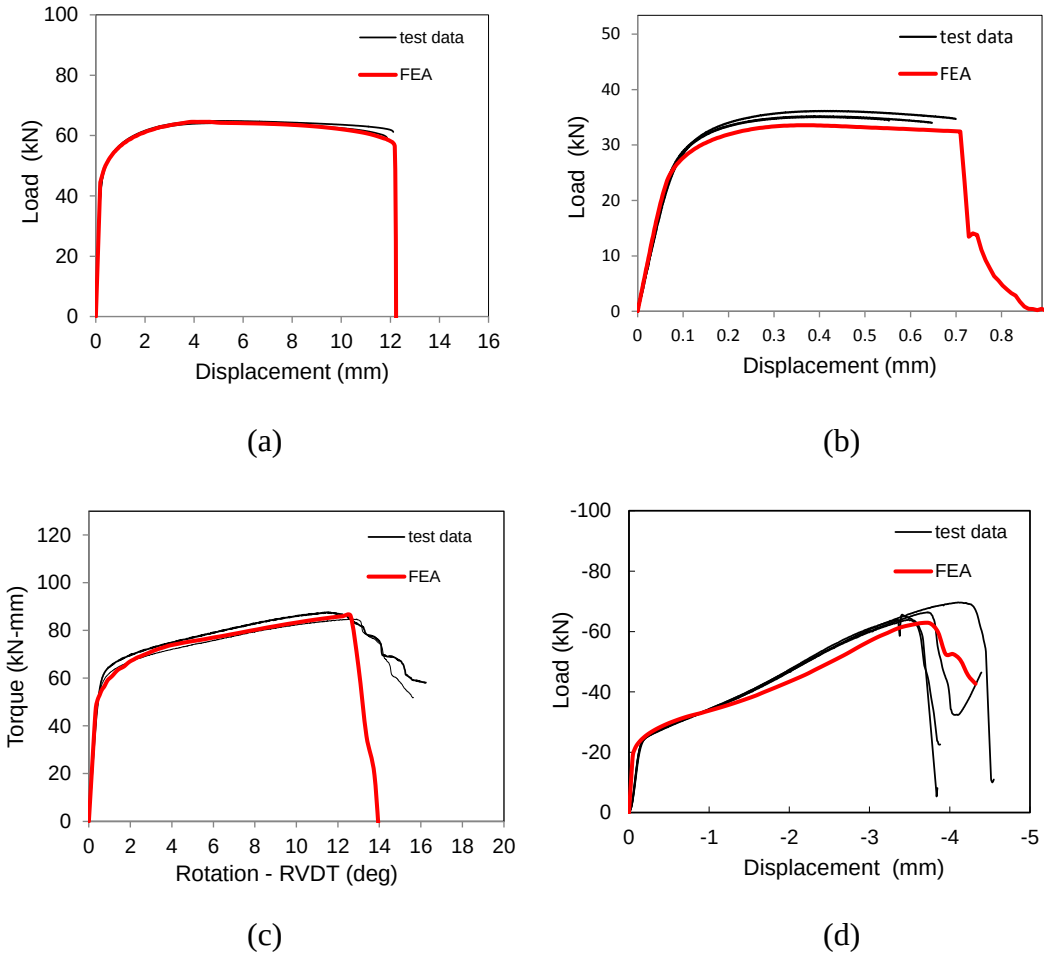

Figure 5. 9 Comparison of load vs. displacement or torque vs. twist angle response between the experimental data and FEA prediction: (a) Smooth round tensile specimen; (b) Notched round tensile specimen; (c) Pure torsion specimen; (d) Compression specimen .

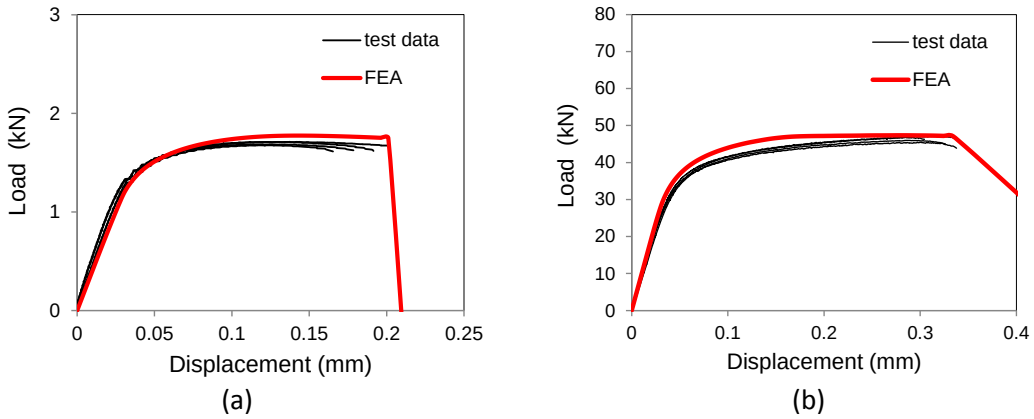

Figure 5. 10 Comparison of the computed load vs. displacement responses with experimental data for (a) flat notched tensile specimen and (b) flat grooved plane strain tensile specimen.

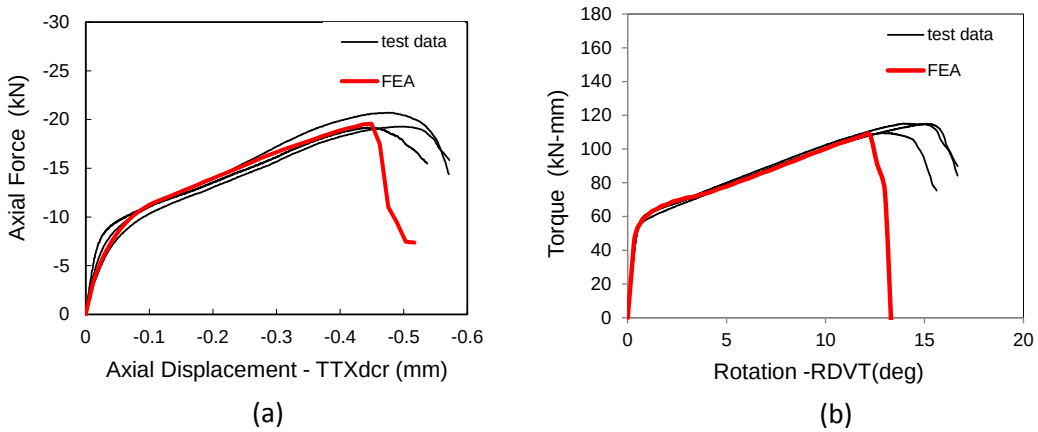

Figure 5. 11 Comparisons between the numerical predictions and the experimental data of the torsion-compression specimen: (a) axial force vs. axial displacement; (b) torque vs. twist angle

2) Prediction of fracture initiation and propagation

To further examine the capability of the extended GTN model, prediction of fracture initiation, propagation and fracture surface appearance are discussed in this section. Figures 5.12 to 5.18 provide the contour plots of several state variables during

the loading history to show the volumetric and shear damage initiation, accumulation, and propagation process.

For the smooth round bar tensile specimen, as shown in Figure 5.12, the crack initiated in the center of specimen where the triaxiality was high. The crack growth remained normal to the loading direction initially, was then followed by a slat fracture as it approached to the specimen surface, and finally resulted in a cup-cone fracture surface. The notched round bar specimen does not show the cup-cone features, Figure 5.13.

Figure 5.14 shows fracture initiation occurs at the transition region in the pure torsion specimen due to strain concentration in this region (only a representative section is shown). The crack growth direction was normal to the direction of the applied torque.

For the compression specimen, Figure 5.15 shows that fracture initiates at the top surface where the weight function had a higher value. The crack then propagated towards the specimen center, leading a slant fracture surface. Figure 5.15(a) and (b) are obtained using a 1/8-symmetric finite element model while Figure 15 (c) shows the result of the full model where a coarser mesh was used to reduce the computational cost. In Figure 5.15 (d) is shown the picture of a failed specimen, confirming the features of the failure process and fracture surface predicted in Figure 5.15 (a)-(c).

Figure 5.16 shows contour plots of flat notched tensile specimen, which was under a similar stress state as notched round bar. Fracture started in the center of the specimen, where it had the highest triaxiality, and propagated toward the specimen surface. The fracture surface was mostly flat, with a slight potion of slant fracture at the notch region where shear damage was caused by high plastic strain.

For the flat grooved plane strain specimen, both the stress triaxiality and the shear damage weight function had high values in a large region around the specimen center, Figures 5.17(a) and (b). Fracture initiated at the center of the specimen and propagated to the sides of the specimen with a strong tunneling effect, as shown in Figure 5.17(c). As the crack front approached the specimen edge, shear damage was shown to be high in a slant plane, leading to the formation of a slant shear lip, Figure 5.17(d).

Figure 5.18 provides the contour plots of a representative section of torsion-compression specimen. Similar to the pure torsion test, crack initiation developed at the transition region. Crack growth followed a slant direction towards the center of the specimen.

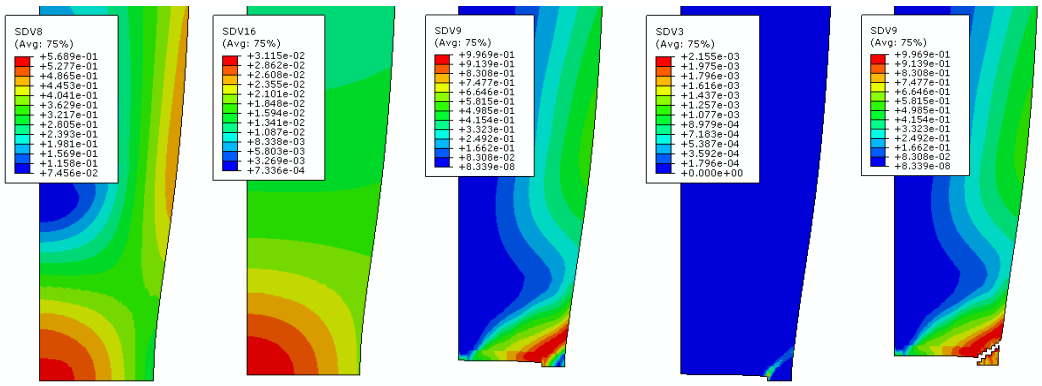

Figure 5. 12 Crack initiation and growth in the smooth round tensile specimen: (a) contour plot of triaxiality before fracture initiation; (b) contour plot of porosity before fracture initiation; (c) contour plot of the weight function after some amount of crack propagation; (d) contour plot of shear damage after some amount of crack propagation; (e) final fracture.

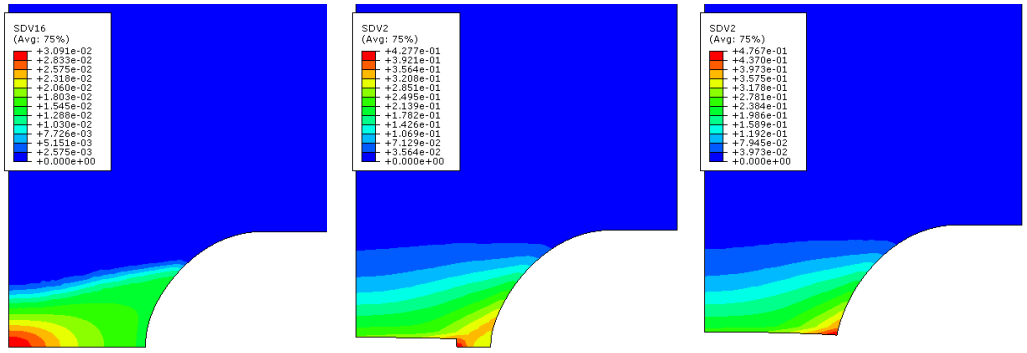

Figure 5. 13 Crack initiation and growth in the notched round tensile specimen: (a) contour plot of porosity before fracture initiation; (b) contour plot of effective plastic strain after some amount of crack propagation; (c) final fracture.

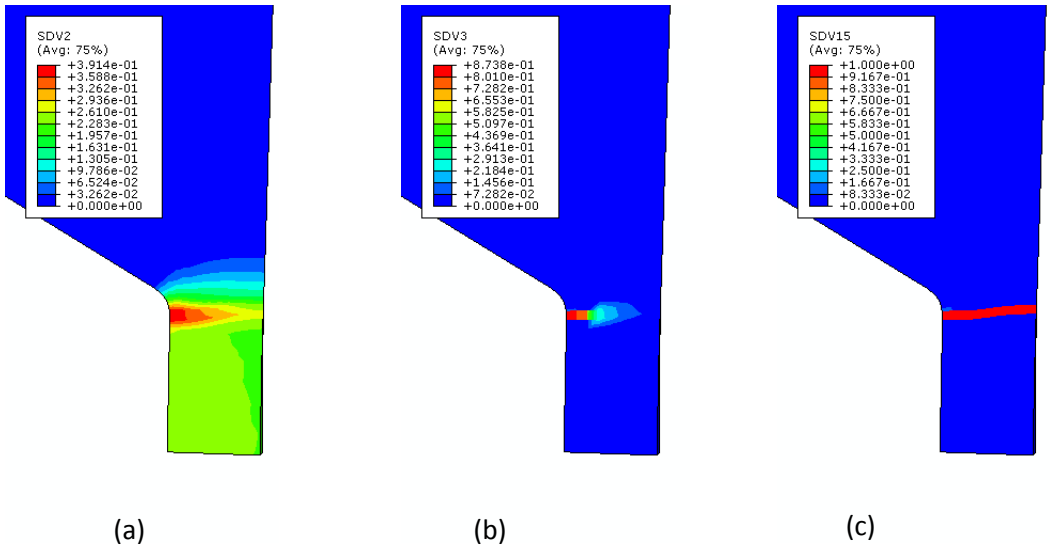

Figure 5. 14 Crack initiation and growth in the pure torsion specimen: (a) contour plot of equivalent plastic strain before fracture initiation; (b) contour plot of shear damage before fracture initiation; (c) final fracture.

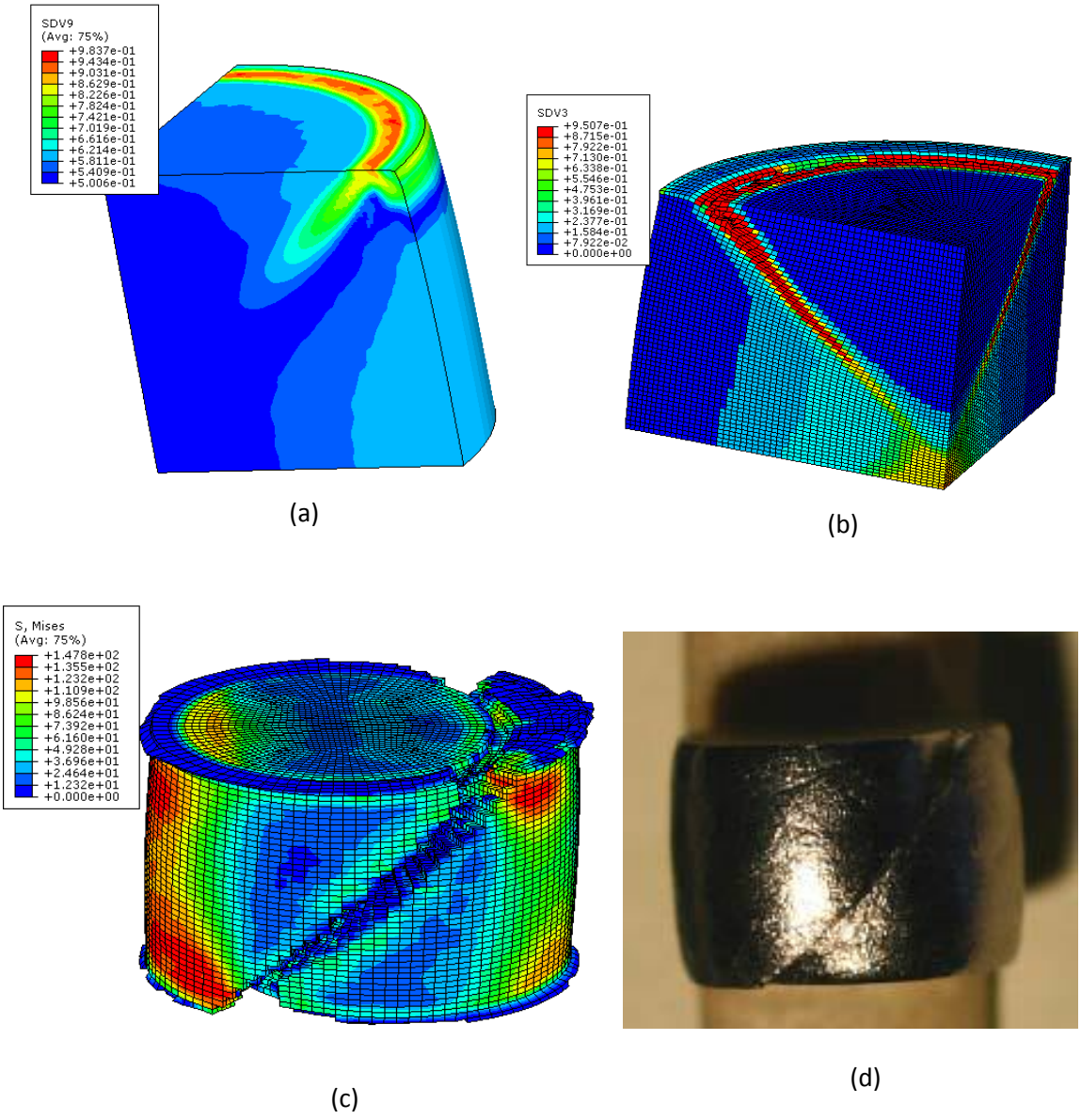

Figure 5. 15 Crack initiation and growth in the compression specimen: (a) contour plot of the weight function before fracture initiation; (b) contour plot of shear damage showing slant crack growth from the top of the specimen toward the center of the specimen; (c) slant fracture predicted using a full model with a coarse mesh.

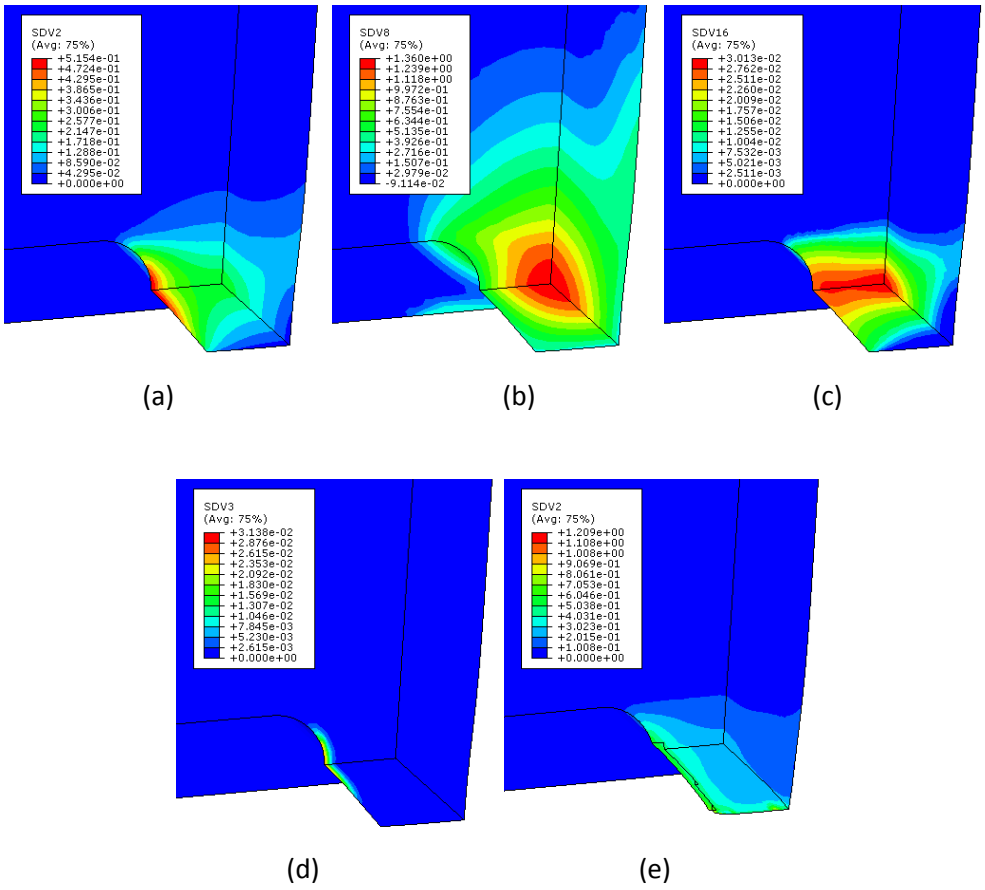

Figure 5. 16 Crack initiation and growth in the flat notched tensile specimen: (a-d) contour plots of equivalent plastic strain, triaxiality, porosity and shear damage before fracture initiation; (e) final fracture.

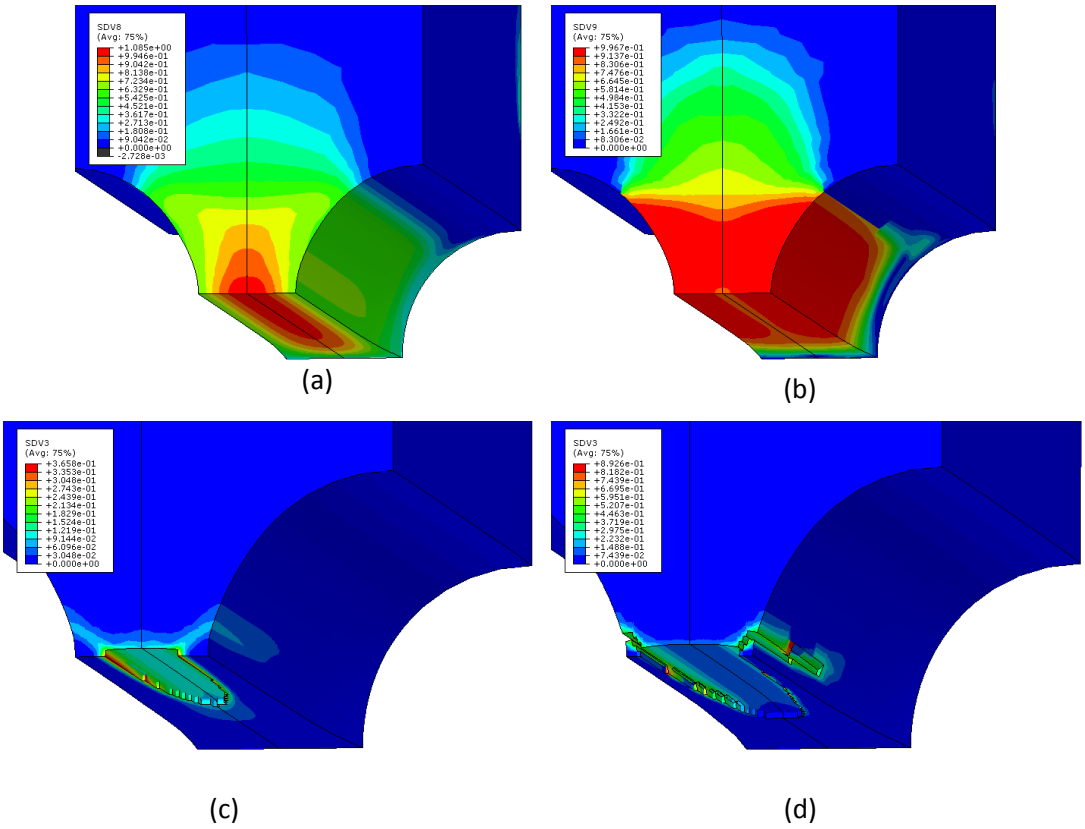

Figure 5. 17 Crack initiation and growth in the flat grooved plane strain tensile specimen: (a-b) contour plots of triaxiality and shear damage weigh function before fracture initiation; (c) contour plot of shear damage after some amount of crack propagation; (d) final fracture.

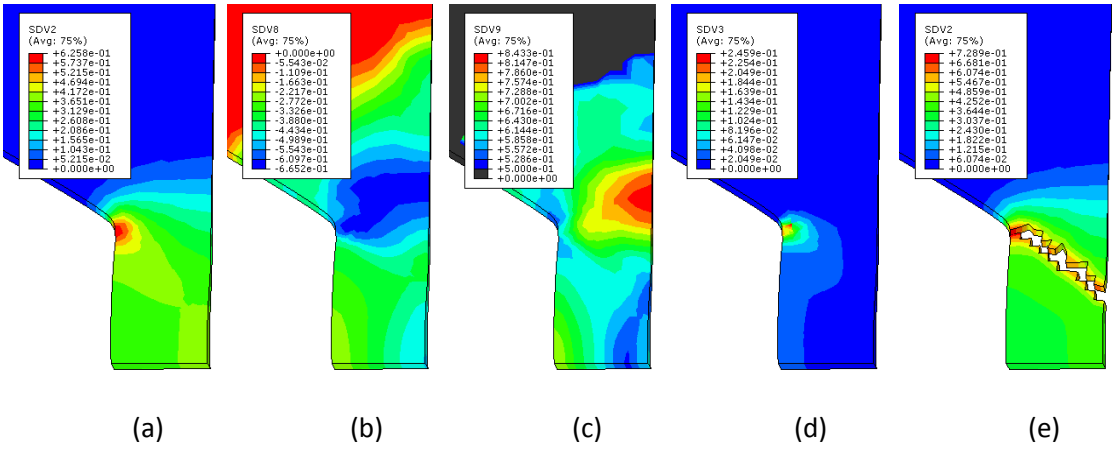

Figure 5. 18 Crack initiation and growth in the torsion-compression specimen: (a-d) contour plots of equivalent plastic strain, triaxiality, shear damage weigh function and shear damage before fracture initiation; (e) final fracture.

5.4 Concluding Remarks

In this chapter, the GTN model was extended to account for shear-induced damage by combining the damage mechanics concept with the void growth model. In particular, two damage parameters, the volumetric damage and the shear damage, were coupled into the yield function and flow potential. The evolution law for void volume fraction remained the same as in the original GTN model and a new shear damage evolution law was proposed. Separate localization criteria were introduced for volumetric damage and shear damage. Material failure occurred once the total damage parameter reaches unity. The effectiveness of the new model was illustrated through a series of numerical tests comparing its performance with existing models. As an application, the model was employed to predict the ductile failure behavior of a beta-treated Zircaloy-4, where the plastic response of the undamaged matrix material exhibited tension-compression asymmetry, by coupling the proposed damage modeling framework with a recently developed J_2-J_3 plasticity model for the matrix material. The combined plasticity and ductile failure model was implemented in ABAQUS via a user defined subroutine. A model calibration scheme was presented and the material constants were determined based on experimental observations a semi-inverse method of matching the predicted load-displacement responses with experimental data for various specimens. The calibrated model predicted very well the load-displacement response, fracture initiation point, and propagation behavior in a variety of specimens, including specimens that exhibited zero or negative stress triaxiality.

CHAPTER VI

CONCLUSIONS AND FUTURE WORK

6.1 Conclusions

In this thesis, many aspects of ductile fracture have been studied. The conclusions from the study are summarized as below:

1). From the study on the effects of strain rate and temperature on ductile failure, the strain-rate dependency and temperature dependency given by the Johnson-Cook plasticity and fracture models cannot be generally applied for the AA 5XXX series materials, especially in the temperature and loading rate ranges where DSA effect exists. For AA 6082-T6, the effect of temperature softening and failure strain increase with elevated temperature was well predicted by the Johnson-Cook plasticity and fracture models. The triaxiality dependency of ductile fracture was also well defined by Johnson-Cook fracture model for all the materials studied.

2). It was observed that AA 5083-H116 displayed strong lode angle/J_3 dependency in its plasticity behaviors, and weak dependency in fracture behaviors. The Xue-Wierzbicki fracture model with dependency on both triaxiality and the Lode angle, was calibrated with the experimental results and implemented into a user subroutine (VUMAT) in ABAQUS. The model was shown to have the ability to predict the crack initiation and growth for complex loading cases.

3). A local out-of-plane compression approach was used to generate residual stress fields in C(T) specimens and these residual stress fields were quantified with finite element modeling of the side compression process. Tensile residual stress not only increased the crack driving force but also raised the constraint level in crack tip region, which resulted in lower fracture resistance. Compressive residual stress had the opposite effect. The whole process, from residual stress generation to the breakage of specimen was well simulated with the calibrated plasticity model and ductile fracture model. This test combined with numerical method proved to be an effective way to study the residual stress effect on ductile fracture.

4). The GTN model was extended to account for shear-induced damage by combining the damage mechanics concept with the void growth model. Two damage parameters, the volumetric damage and the shear damage, were coupled into the yield function and flow potential. Separate localization criterion was introduced for volumetric damage and shear damage, and material failure was said to have occurred if the total damage parameter reached unity. The effectiveness of the new model was validated through a series of numerical tests that compare the new model with existing Gurson type models in several aspects: the predicted shear damage under high triaxiality was greatly improved compared to the existing models; the void growth prediction was more realistic; the model also showed the ability to predict the shear failure under negative triaxiality.

5). The extended GTN model was implemented to study the ductile failure behavior of a beta-treated Zircaloy-4, where the plastic response of the undamaged matrix material exhibits tension-compression asymmetry and follows a previously

developed *J2-J3* model. A model calibration scheme was presented. The calibrated model predicted very well the load-displacement response and fracture initiation and propagation behavior in a variety of specimens, including specimens that exhibit zero or negative stress triaxiality.

6.2 Future work

Although the extended GTN model in Chapter 5 successfully predicted material behaviors under various loading conditions, there are still some remaining issues that need further consideration.

6.2.1 Micromechanical model - a tentative attempt

The models discussed in Chapter 5 assumed no shear damage under axisymmetric tensile loading. This assumption was based on the experimental observation that the main failure mechanism under this type of loading was void growth and coalescence, for which the original Gurson-type model can predict reasonably good results. However, in the absence of hydrostatic tension, the fracture model should have the ability to predict failure caused by shear induced damage. This is the reason why we introduced a constant k for negative triaxiality to describe failure caused by material shear or distortion at any lode angle (Eq. 5.12). This treatment is ad hoc and without physical explanation.

Under the assumption of no shear damage for generalized tension ($\theta = -\pi/6$) and full shear damage for generalized shear ($\theta = 0$), the case with $\theta = -\pi/6$ is supposedly the upper limit and $\theta = 0$ the lower limit in terms of the failure strain. However, this is not always the case. As shown in the experiments in [80], plane strain specimens ($\theta = 0$)

experienced higher failure strain than the notched round bar specimens (θ = -π/6) at the same triaxiality level. As we discussed in Chapter 4, in the 3D fracture locus constructed in the space of (ε_f, T^*, θ), there should be three limiting cases, θ = -π/6, θ = 0 and θ = π/6. It is possible for any of these limiting cases to become the upper or lower bound limit; it is also possible that these three curves will intersect with each other when the 3D surface is projected into the plane of the equivalent fracture strain and stress triaxiality [44].

From the above discussion, we can make a further assumption that any type of plastic deviatoric deformation can result in damage. Based on this, we proposed a new tentative damage model, with the effect of void damage and shear damage fully separated. "Fully" here means any type of deviatoric deformation will results in damage, and void damage only describes the void size change. Under this assumption, with the exception of pure hydrostatic loading, any plastic loading will result in deviatoric damage, including the axisymmetric tensile loading where the void is elongated. The volumetric damage is caused by void size increase, same as in the other porous models.

Starting from the model proposed in last chapter, the yield function is not altered here since it already has two damage parameters f and D_s:

$$\Phi = \left(\frac{\sigma_e}{\sigma_M}\right)^2 + 2q_1 f \cosh\left(\frac{q_2}{2}\frac{\sigma_{kk}}{\sigma_M}\right) - \left[1 + \left(q_1 f + D_s\right)^2 - 2D_s\right] = 0, \qquad (6.1)$$

The new model can no longer degenerate to the GTN model except for pure hydrostatic loading, when it can be rewritten as:

$$\Phi = 2q_1 f \cosh\left(\frac{q_2}{2}\frac{\sigma_{kk}}{\sigma_M}\right) - (q_1 f)^2 = 0, \tag{6.2}$$

When the deviatoric loading is applied, the void shape will change. Here an assumption is made that the void shape will not affect the void growth law. This assumption can greatly simplify the model, and is a good approximation prior to the void linkage. It can be verified through a cell model study under pure hydrostatic loading with different void shape.

The shear damage evolution law and its weight function are different from the extended GTN model given in Chapter 5. As discussed in Chapter 5, the void size should affect the shear damage when it is large enough, but the quantitative relationship is obscure. Here we adopt the shear damage evolution law proposed in Xue model, with one additional parameter:

$$\dot{D}_s = q_3(f^{q_4} + Q)g'(\theta)\varepsilon_M^p \dot{\varepsilon}_M^p \tag{6.3}$$

where Q represents the shear damage which is not related to the void shearing effect. If Q has a higher value, the void size effect on shear damage will be lower.

The Lode angle dependency function $g'(\theta)$ is simply defined as

$$g'(\theta) = g(\theta)(1-k) + k = \left(1 - \frac{6|\theta|}{\pi}\right)(1-k) + k \tag{6.4}$$

The symmetric assumption about θ is still used as in the previous chapter to reduce the model complexity. The parameter k distinguishes the generalized shear ($g'(\theta)$

= 1) and generalized tension ($g'(\theta)$ = k). If k =1, then the material fracture behavior is insensitive to the Lode angle; however, it still can predict the failure under zero or positive pressure.

The coalescence criterion is defined as the same as in the Xue model: when the total damage ($q_1 f$ + D_s) reaches the critical value D_c = $q_1 f$, the damage accumulation speeds up until final fracture.

The complete theory structure proposed here can be summed in Eq. (6.5):

$$\Phi = \left(\frac{\sigma_e}{\sigma_M}\right)^2 + 2q_1 f^* \cosh\left(\frac{q_2}{2}\frac{\sigma_{kk}}{\sigma_M}\right) - \left[1 + D^2 - 2D_s^*\right] = 0;$$

$$D = q_1 f^* + D_s^*; \qquad \sigma_M \dot{\varepsilon}_M^p = (1 - D/q_1)\sigma_{ij}\dot{\varepsilon}_{ij}^p,$$

$$\dot{\varepsilon}_{ij}^p = \dot{\lambda} n_{ij}; \quad n_{ij} = \frac{\partial \Phi}{\partial \sigma_{ij}}$$

$$K_d = \begin{cases} 1 & \text{for } D \le D_c \\ \dfrac{1/q_1 - f_c}{f_f - f_c} & \text{for } D_c < D \le 1 \end{cases}; \tag{6.5}$$

$$\dot{f} = (1 - f)\dot{\varepsilon}_{kk}^p; \quad \dot{f}^* = K_d (1 - f)\dot{\varepsilon}_{kk}^p;$$

$$\dot{D}_s^* = K_d \, q_3 (f^{q_4} + Q) g'(\theta) \varepsilon_M^p \dot{\varepsilon}_M^p$$

$$g'(\theta) = \left(1 - \frac{6|\theta|}{\pi}\right)(1 - k) + k$$

Some preliminary study has been conducted with single material point tests, in order to validate the new model proposed above. Table 6.1 lists the constant values that are used for the validation study:

Table 6.1. Constants for the tentative model

q_1	q_2	f_0	f_c	f_f	q_3	q_4
1.5	1	0.005	0.1	0.25	1.8	1/3

The same matrix material constants and volumetric damage parameters are adopted as in Chapter 5. Deviatoric damage parameters are q_3= 1.8 and q_4=1/3, as are used in Xue model to ensure the same behaviors under pure shear.

This study mainly focuses on the effect of parameters *k* and *Q*. *Q* is set to be zero expect for Case 3.

• *Case 1*. Effect of the parameter *k* under zero pressure (T^* = 0)

For generalized shear (pure shear + hydrostatic stress) where θ = 0, the new model yields the same results as the original Xue model and, and the model predication is insensitive to the parameter k. For any other cases where $\theta \neq 0$, the prediction of the new model is affected by the parameter *k*, which defines the shear damage dependency on the Lode angle. Here the results for generalized tension (uniaxial tension + hydrostatic stress, θ = -π/6) are presented as one limit case.

The effect of the parameter *k* was studied for θ = -π/6, T^* = 0 (generalized tension + zero pressure loading conditions) with *k* =0, 0.5, 1, 1.5. Figure 6.1 plots the resultant effective stress σ_e versus matrix plastic strain ε_M^p. It shows that the higher *k* is, the lower the ductility. For *k* = 0, the new model degenerates to the Xue model, and there is no shear damage. For *k* =1, the predicted shear damage is the same as the pure shear case (θ = 0, T^* = 0, plotted as the black dash line). In fact, as can be predicted from Eq. (6.4), the

shear damage for k =1 is the same for any Lode angle. Other values of k>1, or k<1 at θ = -π/6 corresponds to more or less shear damage compared to the pure shear case.

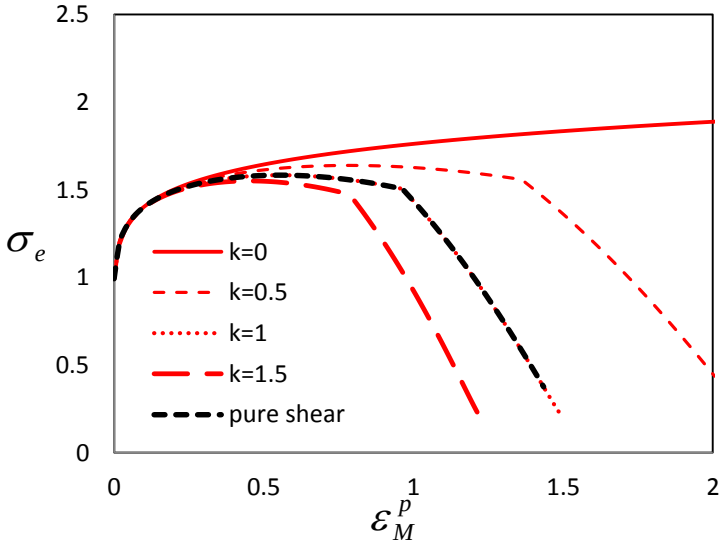

Figure 6. 1 Comparison of the effective stress versus matrix plastic strain response of the prosed model, for k =0, 0.5, 1, 1.5, at θ = -π/6, T^* = 0

• *Case 2.* Effect of parameter k on fracture locus

For a specific k value, the critical strain *Ec* (equivalent strain at the beginning of coalescence) can be obtained with any combination of T^* and θ, and the 3D plot of fracture locus can be generated. Here we studied the fracture loci for k =0, 0.25, 0.5, 1, 2.

The results are shown in Figure 6.2 (a~e), where the shape of the fracture locus changes drastically as k varies. The curve corresponding to the predicted critical strains under generalized shear (at θ = 0) stays the same as k varies, and serves as the lower bound curve for the fracture locus at k < 1, or the upper bound curve for k > 1. Another bound curve of the fracture locus is at generalized tension (θ = -π/6), which gets lower as

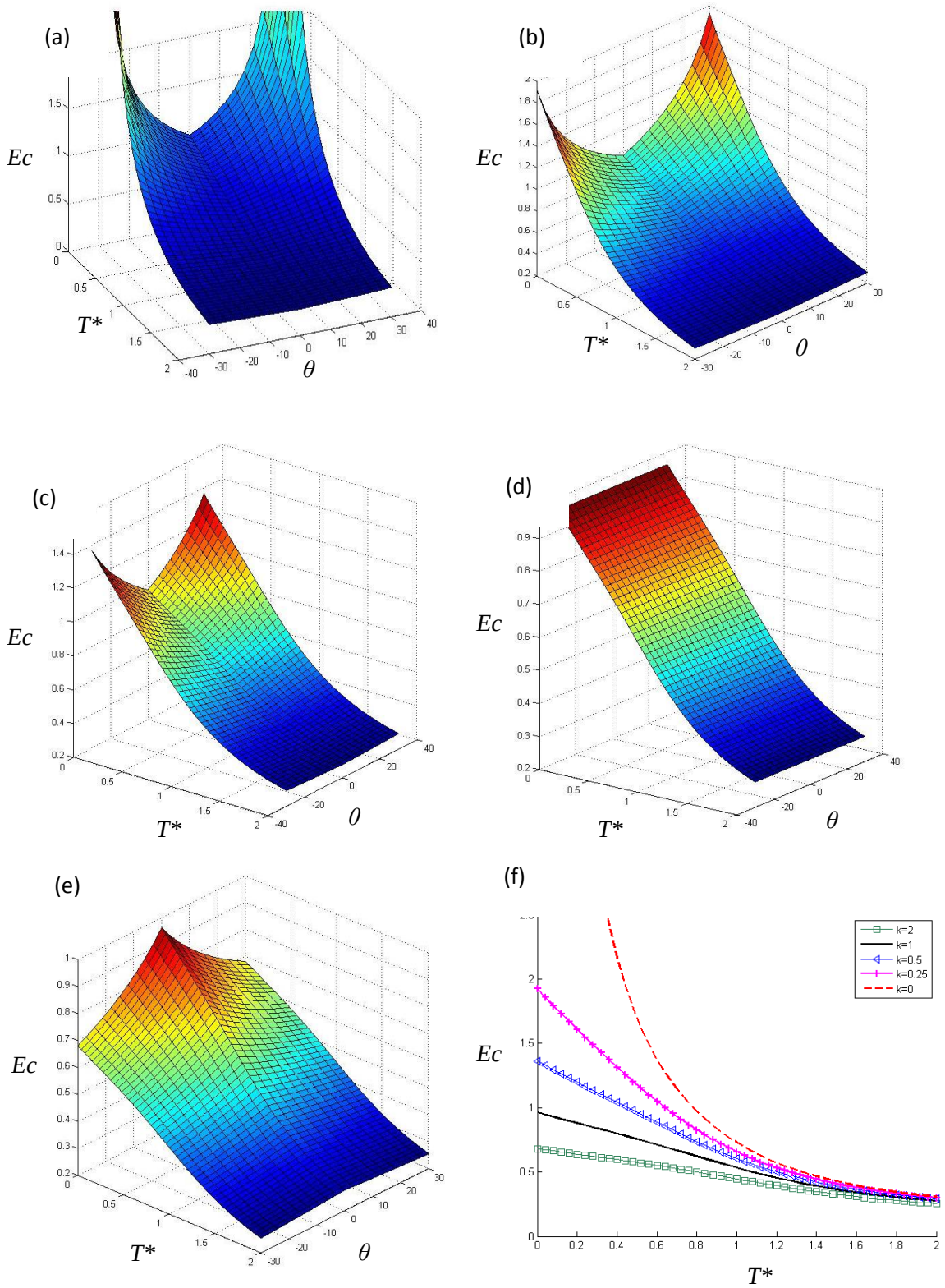

Figure 6. 2 (a~e)The fracture locus at k=0, 0.25, 0.5, 1, 2.; and (f) their projection to the T^*-Ec plane for $\theta = -\pi/6$

k increases, as shown in Figure 6.2(f) when projected to the T^*~ *Ec* space. The effect of the Lode angle on ductility is gradually reduced as the triaxiality get higher.

It is an interesting observation that the shape of the fracture locus predicted by the proposed model is quite similar to that from the macroscopic fracture initiation model. When *k* is smaller than 1 and greater than zero, the shape is a concave, similar to that shown in the Xue-Wierzbicki model (Figure 6.3 (a)).When *k* is equal to 1, the predicted fracture locus flattens out (Figure 6.2 (d)), similar to that from the Johnson and Cook model (Figure 6.3 (b)).

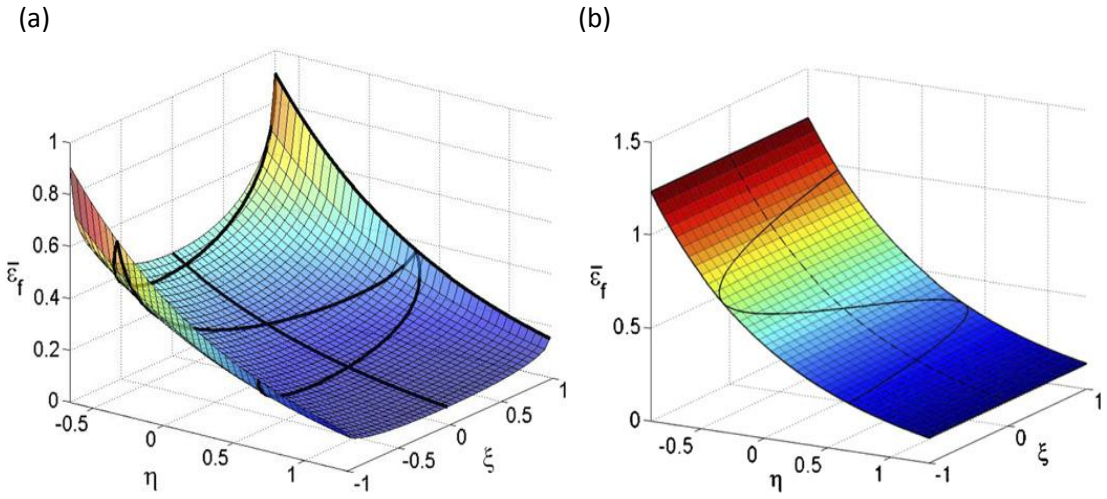

Figure 6. 3 The fracture locus postulated by (a) Xue and Wierzbicki [29]; and (b) Johnson and Cook [17]. (figures from [44])

The symmetric assumption for the Lode angle dependency in Eq. (6.4) also can be released if the material behaviors are different for generalized tension (θ = -π/6) and generalized compression (θ = π/6), such as shown in Figure 6.4.

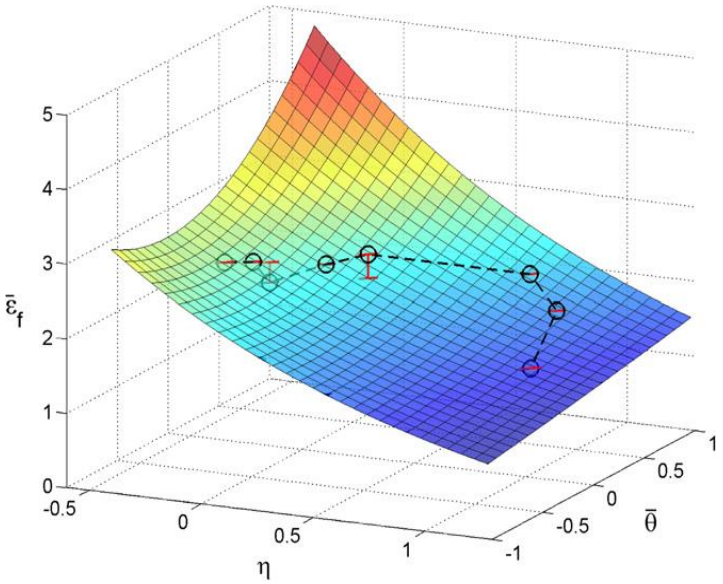

Figure 6. 4 3D Fracture locus of A710 steel [100] (figure from [44]).

- *Case 3.* Effect of Q under generalized shear ($\theta = 0$)

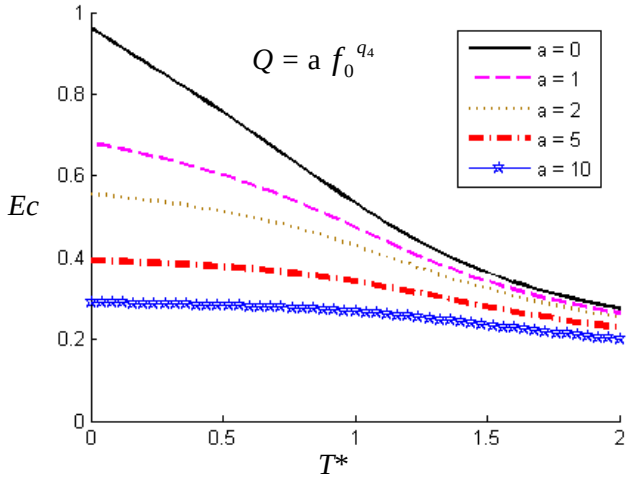

Figure 6. 5 Critical strain. vs. Triaxiality at different Q values ($\theta = 0$)

Parameter Q in Eq. (6.3) represents the shear damage which is not related to the void shearing effect. Here we tested the effect of $Q = a\ f_0^{q_4}$, with a = 0, 1, 2, 5, 10, under

generalized shear loading. The results are shown in Figure 6.5. As Q value increases, the void size effect on shear damage decreases, and the critical strain curve become flatter.

If we set initial void volume fraction f_0 = 0, and the Lode angle dependency parameter k =1, any value of Q great than zero will give constant critical strain.

• *Summary of the case study*

The tentative model assumes damage can be induced by any deviatoric plastic deformation. It is therefore capable of predicting damage under generalized tension with zero pressure (unlike the ad hoc modification in Chapter 5). The Lode angle dependency parameter k has great effect on the shape of fracture locus. The close correlation between the new proposed micro-mechanical model and existing macroscopic fracture models indicates the strong potential of this model. The influence of void size effect on shear damage can be reduced by the additional parameter Q, which represents the shear damage not related to the void shearing effect.

This model is still under development, and the application and calibration process for real materials needs further investigation.

6.2.2 Other suggestions of future work

The proposed constitutive model can be improved in some other aspects:

• *Shear damage evolution law*

The proposed model adopts the shear damage evolution law similar to the Xue model (Eq. 6.3). A more reliable approach to model void shearing induced damage would

be through a cell model study, where the void shape and distribution effects on shear damage can be studied.

- *Coalescence condition*

The coalescence condition defined by a critical value of the summation of void and shear contribution is just a rough assumption. A better coalescence condition such as the one based on the ligament distance shrinkage needs to be defined. Cell model study can also be conducted to investigate how the ligament distance shrinks under the combination of tension and shear field.

- *Pure shear or simple shear*

Pure shear and simple shear are defined with the same Lode angle and triaxiality; however, the material deformation is quite different under the two loading cases. Most cell study of void-shearing effect is for simple shear loading. It is questionable to apply the same conclusion to pure shear.

Thus another interesting direction of future study would be a comparison of pure shear and simple shear case study, in order to find out appropriate fracture model for different deformation modes.

BIBLIOGRAPHY

[1] Besson, J. Continuum models of ductile fracture: a review. *International Journal of Damage Mechanics*. 19, 3-52, 2010.

[2] Pineau, A. Development of the local approach to fracture over the past 25 years: theory and applications. *International Journal of Fracture*. 138, 139-166, 2006.

[3] Lemaitre, J. Local approach of fracture. *Engineering fracture mechanics*. 25, 523-537, 1986.

[4] Pineau, A. Review of fracture micromechanisms and a local approach to predicting crack resistance in low strength steels. *ICF5, Cannes (France) 19811980).*

[5] Stone, R.V., Cox, T., Low, J. and Psioda, J. Microstructural aspects of fracture by dimpled rupture. *International Metals Reviews*. 30, 157-180, 1985.

[6] Garrison Jr, W. and Moody, N. Ductile fracture. *Journal of Physics and Chemistry of Solids*. 48, 1035-1074, 1987.

[7] Ludwik, P. and Scheu, R. Ueber Kerbwirkungen bei Flusseisen. *Stahl u. Eisen*. 43, 999-1001, 1923.

[8] Orowan, E. *Notch, Brittleness and the Strength of Metals*. (Institution of Engineers and Shipbuilders in Scotland, 1945).

[9] Bridgman, P.W. *Studies in large plastic flow and fracture*. (Harvard University Press, 1964).

[10] French, I. and Weinrich, P. The effect of hydrostatic pressure on the tensile fracture of α-brass. *Acta metallurgica*. 21, 1533-1537, 1973.

[11] French, I. and Weinrich, P. The effects of hydrostatic pressure on the mechanism of tensile fracture of aluminum. *Metallurgical Transactions A*. 6, 1165-1169, 1975.

[12] French, I.E. and Weinrich, P.F. The influence of hydrostatic pressure on the tensile deformation and fracture of copper. *Metallurgical Transactions A*. 6, 785-790, 1975.

[13] McClintock, F.A. A criterion for ductile fracture by the growth of holes. *Journal of Applied Mechanics*. 35, 363, 1968.

[14] Rice, J.R. and Tracey, D.M. On the ductile enlargement of voids in triaxial stress fields∗. *Journal of the Mechanics and Physics of Solids*. 17, 201-217, 1969.

[15] Gurson, A. Continuum Theory of Ductile Rupture by Void Nucleation and Growth: Part I—Yield Criteria and Flow Rules for Porous Ductile Media. *Journal of Engineering Materials and Technology*. 99, 2, 1977.

[16] Hancock, J. and Mackenzie, A. On the mechanisms of ductile failure in high-strength steels subjected to multi-axial stress-states. *Journal of the Mechanics and Physics of Solids*. 24, 147-160, 1976.

[17] Johnson, G.R. and Cook, W.H. Fracture characteristics of three metals subjected to various strains, strain rates, temperatures and pressures. *Engineering fracture mechanics*. 21, 31-48, 1985.

[18] Børvik, T., Hopperstad, O., Berstad, T. and Langseth, M. A computational model of viscoplasticity and ductile damage for impact and penetration. *European Journal of Mechanics-A/Solids*. 20, 685-712, 2001.

[19] Børvik, T., Hopperstad, O., Dey, S., Pizzinato, E., Langseth, M. and Albertini, C. Strength and ductility of Weldox 460 E steel at high strain rates, elevated temperatures and various stress triaxialities. *Engineering fracture mechanics*. 72, 1071-1087, 2005.

[20] McClintock, F.A. Plasticity aspects of fracture. *Fracture: an advanced treatise*. 3, 47-225, 1971.

[21] Xue, L. Ductile fracture modeling: theory, experimental investigation and numerical verification. (Massachusetts Institute of Technology, 2007).

[22] Bao, Y. and Wierzbicki, T. On fracture locus in the equivalent strain and stress triaxiality space. *International Journal of Mechanical Sciences*. 46, 81-98, 2004.

[23] Kim, J., Gao, X. and Srivatsan, T. Modeling of crack growth in ductile solids: a three-dimensional analysis. *International Journal of Solids and Structures*. 40, 7357-7374, 2003.

[24] Kim, J., Gao, X. and Srivatsan, T.S. Modeling of void growth in ductile solids: effects of stress triaxiality and initial porosity. *Engineering fracture mechanics*. 71, 379-400, 2004.

[25] Kim, J., Zhang, G. and Gao, X. Modeling of ductile fracture: Application of the mechanism-based concepts. *International Journal of Solids and Structures*. 44, 1844-1862, 2007.

[26] Gao, X. and Kim, J. Modeling of ductile fracture: significance of void coalescence. *International Journal of Solids and Structures*. 43, 6277-6293, 2006.

[27] Gao, X., Wang, T. and Kim, J. On ductile fracture initiation toughness: effects of void volume fraction, void shape and void distribution. *International Journal of Solids and Structures*. 42, 5097-5117, 2005.

[28] Barsoum, I. and Faleskog, J. Rupture mechanisms in combined tension and shear—experiments. *International Journal of Solids and Structures*. 44, 1768-1786, 2007.

[29] Xue, L. and Wierzbicki, T. Ductile fracture initiation and propagation modeling using damage plasticity theory. *Engineering fracture mechanics*. 75, 3276-3293, 2008.

[30] Rice, J.R. *The localization of plastic deformation*. (Division of Engineering, Brown University, 1976).

[31] Fleck, N. and Hutchinson, J. Void growth in shear. *Proceedings of the Royal Society of London. A. Mathematical and Physical Sciences*. 407, 435-458, 1986.

[32] Barsoum, I. and Faleskog, J. Rupture mechanisms in combined tension and shear—micromechanics. *International Journal of Solids and Structures*. 44, 5481-5498, 2007.

[33] Tvergaard, V. Shear deformation of voids with contact modelled by internal pressure. *International Journal of Mechanical Sciences*. 50, 1459-1465, 2008.

[34] Scheyvaerts, F., Onck, P., Tekoglu, C. and Pardoen, T. The growth and coalescence of ellipsoidal voids in plane strain under combined shear and tension. *Journal of the Mechanics and Physics of Solids*. 59, 373-397, 2011.

[35] Anderson, P., Fleck, N. and Johnson, K. Localization of plastic deformation in shear due to microcracks. *Journal of the Mechanics and Physics of Solids*. 38, 681-699, 1990.

[36] Xue, L. Constitutive modeling of void shearing effect in ductile fracture of porous materials. *Engineering fracture mechanics*. 75, 3343-3366, 2008.

[37] Nahshon, K. and Hutchinson, J. Modification of the Gurson model for shear failure. *European Journal of Mechanics-A/Solids*. 27, 1-17, 2008.

[38] Nielsen, K.L. and Tvergaard, V. Ductile shear failure or plug failure of spot welds modelled by modified Gurson model. *Engineering fracture mechanics*. 77, 1031-1047, 2010.

[39] Hill, M.R. and Panontin, T.L. Effect of residual stress on brittle fracture testing. *Fatigue and Fracture Mechanics: 29th Volume, ASTM STP*. 1332, 154-175, 1999.

[40] Panontin, T. and Hill, M. The effect of residual stresses on brittle and ductile fracture initiation predicted by micromechanical models. *International Journal of Fracture*. 82, 317-333, 1996.

[41] Almer, J.D., Cohen, J. and Winholtz, R. The effects of residual macrostresses and microstresses on fatigue crack propagation. *Metallurgical and Materials Transactions A*. 29, 2127-2136, 1998.

[42] Meith, W.A., Hill, M.R. and Panontin, T.L. Analytical & Experimental Study of Fracture in Bend Specimens Subjected to Local Compression. *ASTM SPECIAL TECHNICAL PUBLICATION*. 1417, 426-444, 2003.

[43] Mahmoudi, A., Truman, C. and Smith, D. Using local out-of-plane compression (LOPC) to study the effects of residual stress on apparent fracture toughness. *Engineering fracture mechanics*. 75, 1516-1534, 2008.

[44] Bai, Y. and Wierzbicki, T. A new model of metal plasticity and fracture with pressure and Lode dependence. *International Journal of Plasticity*. 24, 1071-1096, 2008.

[45] Johnson, G.R. and Cook, W.H. A constitutive model and data for metals subjected to large strains, high strain rates and high temperatures. *Proceedings of the 7th International Symposium on Ballistics*, pp. 541-547 (The Hague, Netherlands: International Ballistics Committee, 1983).

[46] Wierzbicki, T., Bao, Y., Lee, Y.-W. and Bai, Y. Calibration and evaluation of seven fracture models. *International Journal of Mechanical Sciences*. 47, 719-743, 2005.

[47] Cockcroft, M. and Latham, D. Ductility and the workability of metals. *J Inst Metals*. 96, 33-39, 1968.

[48] Wilkins, M., Streit, R. and Reaugh, J. Cumulative-strain-damage model of ductile fracture: simulation and prediction of engineering fracture tests. (Lawrence Livermore National Lab., CA (USA); Science Applications, Inc., San Leandro, CA (USA), 1980).

[49] Manual, A.U.s. Version 6.7. *Hibbit, Karlsson & Sorensen*, 2007.

[50] Lemaitre, J. Coupled elasto-plasticity and damage constitutive equations. *Computer Methods in Applied Mechanics and Engineering*. 51, 31-49, 1985.

[51] Li, Y. and Wierzbicki, T. Prediction of plane strain fracture of AHSS sheets with post-initiation softening. *International Journal of Solids and Structures*. 47, 2316-2327, 2010.

[52] Lemaitre, J. and Lippmann, H. *A course on damage mechanics*. (Springer Berlin, 1996).

[53] Rousselier, G. Ductile fracture models and their potential in local approach of fracture. *Nuclear engineering and design*. 105, 97-111, 1987.

[54] Tvergaard, V. Influence of voids on shear band instabilities under plane strain conditions. *International Journal of Fracture*. 17, 389-407, 1981.

[55] Tvergaard, V. Influence of void nucleation on ductile shear fracture at a free surface. *Journal of the Mechanics and Physics of Solids*. 30, 399-425, 1982.

[56] Chu, C. and Needleman, A. Void nucleation effects in biaxially stretched sheets. *Journal of Engineering Materials and Technology*. 102, 249, 1980.

[57] Tvergaard, V. and Needleman, A. Analysis of the cup-cone fracture in a round tensile bar. *Acta metallurgica*. 32, 157-169, 1984.

[58] Koplik, J. and Needleman, A. Void growth and coalescence in porous plastic solids. *International Journal of Solids and Structures*. 24, 835-853, 1988.

[59] McClintock, F.A., Kaplan, S.M. and Berg, C.A. Ductile fracture by hole growth in shear bands. *International Journal of Fracture Mechanics*. 2, 614-627, 1966.

[60] Gologanu, M., Leblond, J.-B. and Devaux, J. Approximate models for ductile metals containing non-spherical voids—case of axisymmetric prolate ellipsoidal cavities. *Journal of the Mechanics and Physics of Solids*. 41, 1723-1754, 1993.

[61] Gologanu, M., Leblond, J.-B. and Devaux, J. Approximate models for ductile metals containing nonspherical voids: case of axisymmetric oblate ellipsoidal cavities. *Journal of Engineering Materials and Technology*. 116, 290-297, 1994.

[62] Thomason, P. A three-dimensional model for ductile fracture by the growth and coalescence of microvoids. *Acta metallurgica*. 33, 1087-1095, 1985.

[63] Pardoen, T. and Hutchinson, J. An extended model for void growth and coalescence. *Journal of the Mechanics and Physics of Solids*. 48, 2467-2512, 2000.

[64] Zhang, Z. and Niemi, E. A new failure criterion for the Gurson-Tvergaard dilational constitutive model. *International Journal of Fracture*. 70, 321-334, 1994.

[65] Benzerga, A.A. and Besson, J. Plastic potentials for anisotropic porous solids. *European Journal of Mechanics-A/Solids*. 20, 397-434, 2001.

[66] Wang, D.-A., Pan, J. and Liu, S.-D. An anisotropic Gurson yield criterion for porous ductile sheet metals with planar anisotropy. *International Journal of Damage Mechanics*. 13, 7-33, 2004.

[67] Besson, J. and Guillemer-Neel, C. An extension of the Green and Gurson models to kinematic hardening. *Mechanics of materials*. 35, 1-18, 2003.

[68] Mühlich, U. and Brocks, W. On the numerical integration of a class of pressure-dependent plasticity models including kinematic hardening. *Computational Mechanics*. 31, 479-488, 2003.

[69] Gao, X., Zhang, T., Zhou, J., Graham, S.M., Hayden, M. and Roe, C. On stress-state dependent plasticity modeling: Significance of the hydrostatic stress, the third invariant of stress deviator and the non-associated flow rule. *International Journal of Plasticity*. 27, 217-231, 2011.

[70] Perrin, G. and Leblond, J.-B. Accelerated void growth in porous ductile solids containing two populations of cavities. *International Journal of Plasticity*. 16, 91-120, 2000.

[71] Besson, J., Devillers-Guerville, L. and Pineau, A. Modeling of scatter and size effect in ductile fracture: application to thermal embrittlement of duplex stainless steels. *Engineering fracture mechanics*. 67, 169-190, 2000.

[72] Pardoen, T., Dumont, D., Deschamps, A. and Brechet, Y. Grain boundary versus transgranular ductile failure. *Journal of the Mechanics and Physics of Solids*. 51, 637-665, 2003.

[73] Zhou, J., Hayden, M. and Gao, X. An investigation of the strain rate and temperature effects on the plastic flow stress and ductile failure strain of aluminum alloys 5083-H116, 6082-T6 and a 5183 weld metal. *Proceedings of the Institution of Mechanical Engineers, Part C: Journal of Mechanical Engineering Science*. 227, 883-895, 2013.

[74] Clausen, A.H., Børvik, T., Hopperstad, O.S. and Benallal, A. Flow and fracture characteristics of aluminium alloy AA5083–H116 as function of strain rate, temperature and triaxiality. *Materials Science and Engineering: A*. 364, 260-272, 2004.

[75] Naka, T. and Yoshida, F. Deep drawability of type 5083 aluminium–magnesium alloy sheet under various conditions of temperature and forming speed. *Journal of Materials Processing Technology*. 89, 19-23, 1999.

[76] Van den Beukel, A. Theory of the effect of dynamic strain aging on mechanical properties. *Physica status solidi (a)*. 30, 197-206, 1975.

[77] Mukai, T., Higashi, K. and Tanimura, S. Influence of the magnesium concentration on the relationship between fracture mechanism and strain rate in high purity Al-Mg alloys. *Materials Science and Engineering: A*. 176, 181-189, 1994.

[78] Chen, Y., Clausen, A., Hopperstad, O. and Langseth, M. Stress–strain behaviour of aluminium alloys at a wide range of strain rates. *International Journal of Solids and Structures*. 46, 3825-3835, 2009.

[79] ABAQUS. 6.9 Documentation. *Dassault Systemes Simulia Corporation*, 2010.

[80] Gao, X., Zhang, G. and Roe, C. A study on the effect of the stress state on ductile fracture. *International Journal of Damage Mechanics*. 19, 75-94, 2010.

[81] Lagarias, J.C., Reeds, J.A., Wright, M.H. and Wright, P.E. Convergence properties of the Nelder--Mead simplex method in low dimensions. *SIAM Journal on Optimization*. 9, 112-147, 1998.

[82] Skinner, D., Zedalis, M. and Gilman, P. Effect of strain rate on tensile ductility for a series of dispersion-strengthened aluminum-based alloys. *Materials Science and Engineering: A*. 119, 81-86, 1989.

[83] Baird, J. The inhomogeneity of plastic deformation. *ASM, Metals Park, OH*, 191, 1973.

[84] Spitzig, W.A., Sober, R.J. and Richmond, O. Pressure dependence of yielding and associated volume expansion in tempered martensite. *Acta Metallurgica*. 23, 885-893, 1975.

[85] Brünig, M. Numerical simulation of the large elastic-plastic deformation behavior of hydrostatic stress-sensitive solids* 1. *International Journal of Plasticity*. 15, 1237-1264, 1999.

[86] Brünig, M., Berger, S. and Obrecht, H. Numerical simulation of the localization behavior of hydrostatic-stress-sensitive metals. *International Journal of Mechanical Sciences*. 42, 2147-2166, 2000.

[87] Gao, X., Zhang, T., Hayden, M. and Roe, C. Effects of the stress state on plasticity and ductile failure of an aluminum 5083 alloy. *International Journal of Plasticity*. 25, 2366-2382, 2009.

[88] Xue, L. and Wierzbicki, T. Ductile Fracture Characterization of Aluminum Alloy 2024-T351 Using Damage Plasticity Theory. *International Journal of Applied*. 1, 267-304, 2009.

[89] Li, Y., Wierzbicki, T., Sutton, M.A., Yan, J. and Deng, X. Mixed mode stable tearing of thin sheet AI 6061-T6 specimens: experimental measurements and finite element simulations using a modified Mohr-Coulomb fracture criterion. *International Journal of Fracture*, 1-19, 2010.

[90] Kim, J. and Gao, X. A generalized approach to formulate the consistent tangent stiffness in plasticity with application to the GLD porous material model. *International Journal of Solids and Structures*. 42, 103-122, 2005.

[91] Liu, J., Zhang, Z. and Nyhus, B. Residual stress induced crack tip constraint. *Engineering Fracture Mechanics*. 75, 4151-4166, 2008.

[92] Ren, X., Zhang, Z. and Nyhus, B. Effect of residual stresses on the crack-tip constraint in a modified boundary layer model. *International Journal of Solids and Structures*. 46, 2629-2641, 2009.

[93] Cockeram, B. and Chan, K. In situ studies and modeling the fracture of Zircaloy-4. *Journal of Nuclear Materials*. 393, 387-408, 2009.

[94] Cockeram, B. and Chan, K. In-situ Studies and Modeling of the Deformation and Fracture Mechanism for Wrought Zircaloy-4 and Zircaloy-2 as a Function of Stress-State. *Journal of Nuclear Materials*, 2012.

[95] Zhai, J., Gao, X., Sobotka, J.C., Webler, B.A., Cockeram B.V. Modeling the tension-compression asymmetric yield behavior of a β-treated Zircaloy-4., 2013.

[96] Nielsen, K.L. and Tvergaard, V. Effect of a shear modified Gurson model on damage development in a FSW tensile specimen. *International Journal of Solids and Structures*. 46, 587-601, 2009.

[97] Malcher, L., Andrade Pires, F. and César de Sá, J. An assessment of isotropic constitutive models for ductile fracture under high and low stress triaxiality. *International Journal of Plasticity*. 30, 81-115, 2012.

[98] Zhang, T., Gao, X., Webler, B.A., Cockeram, B.V., Hayden, M. and Graham, S.M. Application of the Plasticity Models that Involve Three Stress Invariants. *International Journal of Applied Mechanics*. 4, 2012.

[99] Crisfield, M. Nonlinear finite element analysis of solids and structures, v. 1. 1997.

[100] Wierzbicki, T., Bao, Y. and Bai, Y. A new experimental technique for constructing a fracture envelope of metals under multi-axial loading. *Proceedings of the 2005 SEM annual conference and exposition on experimental and applied mechanics*, pp. 1295-13032005).

[101] Ortiz, M. and Popov, E.P. Accuracy and stability of integration algorithms for elastoplastic constitutive relations. *International Journal for Numerical Methods in Engineering*. 21, 1561-1576, 1985.

[102] Simo, J. and Ortiz, M. A unified approach to finite deformation elastoplastic analysis based on the use of hyperelastic constitutive equations. *Computer Methods in Applied Mechanics and Engineering*. 49, 221-245, 1985.

[103] Ortiz, M. and Simo, J. An analysis of a new class of integration algorithms for elastoplastic constitutive relations. *International Journal for Numerical Methods in Engineering*. 23, 353-366, 1986.

APPENDICES

APPENDIX A

SINGLE MATERIAL POINT TEST PROCEDURE

The following summarizes the procedure of the single material point test which keeps the stress triaxiality and Lode parameter constant during the loading history.

Consider in the principal stress space and let $\tilde{\sigma}$ be a proportionality factor. The mean stress can be expressed as

$$\sigma_m = \frac{1}{3}\sigma_{kk} = \beta\tilde{\sigma} \tag{A1}$$

The three principal deviatoric stresses components can be expressed as

$$s_1 = \tilde{\sigma}, \quad s_2 = \alpha\tilde{\sigma}, \quad s_3 = (-1-\alpha)\tilde{\sigma} \tag{A2}$$

where α and β are constants which can be related to the stress triaxiality and Lode parameter and the three principal stresses can be expressed as

$$\boldsymbol{\sigma} = \left(1+\beta, \quad \alpha+\beta, \quad \beta-1-\alpha\right)^T \tilde{\sigma} \tag{A3}$$

Therefore the von Mises equivalent stress can be expressed as

$\sigma_e = \tilde{\sigma}\sqrt{3(1+\alpha+\alpha^2)}$ and the stress triaxiality and Lode angle can be related to constant α and β through

$$T^* = \frac{\beta}{\sqrt{3(1+\alpha+\alpha^2)}}$$
$$\theta = \tan^{-1}\left[\left(2\frac{2\alpha+1}{2+\alpha}-1\right)\frac{1}{\sqrt{3}}\right] \tag{A4}$$

For any prescribed T^* and θ, parameters α and β can be solved from Eq. (A4). For θ varying from $-\pi/6$ to $\pi/6$, α varies from -0.5 to 1.

The values of α and β together with the value of $\tilde{\sigma}$ solved from Eq. (5.18b) determines the three principal stresses. Let $h_M = \partial\sigma_M / \partial\varepsilon_M^p$ be the tangent modulus of the matrix material, the following derivatives are needed to compute the hardening modulus, *H*, Eq. (5.17).

$$\frac{\partial f^*}{\partial f} = \begin{cases} 1 & \text{for } f \le f_c \\ \dfrac{1/q_1 - f_c}{f_f - f_c} & \text{for } f_c \le f \le f_f \end{cases}$$

$$\frac{\partial \Phi}{\partial \sigma_M} = -2\frac{\sigma_{eq}^2}{\sigma_M^3} - \frac{3q_1q_2 f^* \sigma_m}{\sigma_M^2}\sinh\left(\frac{3q_2\sigma_m}{2\sigma_M}\right)$$
$$\frac{\partial \Phi}{\partial f^*} = 2q_1\cosh\left(\frac{3q_2\sigma_m}{2\sigma_M}\right) - 2q_1\left(q_1 f^* + D_s\right) \tag{A5}$$
$$\frac{\partial \Phi}{\partial D_s} = 2 - 2\left(q_1 f^* + D_s\right)$$

$$\frac{\partial \varepsilon_M^p}{\partial \lambda} = \frac{\sigma_{ij} n_{ij}}{(1-f)\sigma_M}, \quad \frac{\partial f}{\partial \lambda} = (1-f)n_{kk} + A_n\frac{\partial \varepsilon_M^p}{\partial \lambda}, \quad \frac{\partial D_s}{\partial \lambda} = \psi(\theta,T)\frac{n\, D_s^{\frac{n-1}{n}}}{\varepsilon_f^s}\frac{\partial \varepsilon_M^p}{\partial \lambda}$$

APPENDIX B

STRESS INTEGRATION SCHEME FOR MODIFIED GTN MODEL

In the numerical implementation of plasticity model, the stress integration method can be implicit or explicit. Among implicit methods, backward Euler is the most popular because it's unconditionally stable and relatively easy to implement. However, in the Gauss point level, convergence of the backward Euler can be a major issue for complex models, e.g. models with coupled hardening and softening parameters [101]. In these cases the plastic corrector can have difficulty returning stresses to the yield surface.

Compared to the backward Euler method, the explicit stress integration method can achieve better convergence behavior. However it has two major limitations. First, it lacks exact linearization which is required in the full Newton–Raphson method in solving the global system. Second, it's conditionally stable and requires small time increment. In the present study, the explicit finite element solver was used, for which there was no need to solve global nonlinear equations, and small time increment was already a prerequisite.

A forward-Euler with correction scheme, original proposed by Crisfield [99], was adopted in Chapter 5. The procedure follows three steps as illustrated below:

- STEP 1: Determine the initial yield stress $\boldsymbol{\sigma}^0$.

To implement a forward-Euler scheme in the plastic region, the location of the initial yield position needs to be found.

If the stress tensor at time t ($\boldsymbol{\sigma}^t$) lies on the yield surface, $\boldsymbol{\sigma}^0 = \boldsymbol{\sigma}^t$. Otherwise if $\boldsymbol{\sigma}^t$ lies within the yield surface, and at $t + \Delta t$, a strain increment $\Delta\boldsymbol{\varepsilon}^*$ is applied which results in yielding:

$$\Phi^t = \Phi\left(\boldsymbol{\sigma}^t\right) < 0,\ \Phi^* = \Phi\left(\boldsymbol{\sigma}^t + \Delta\boldsymbol{\sigma}^*\right) > 0, \tag{B1}$$

Here $\Delta\boldsymbol{\sigma}^* = \mathbf{C} : \Delta\boldsymbol{\varepsilon}^*$ is the elastic predictor stress increment. The initial yielding stress can be written as

$$\boldsymbol{\sigma}^0 = \boldsymbol{\sigma}^t + \alpha\Delta\boldsymbol{\sigma}^*,\ \ 0 < \alpha < 1 \tag{B2}$$

Now the problem reduces to finding α. α can be solved by setting the yield surface function to zero

$$\Phi^0 = \Phi\left(\boldsymbol{\sigma}^t + \alpha\Delta\boldsymbol{\sigma}^*\right) = 0, \tag{B3}$$

The Newton–Raphson method is used to solve the above formula

$$\alpha_{(n+1)} = \alpha_{(n)} - \Phi_{(n)} \Big/ \left(\frac{\partial\Phi}{\partial\alpha}\right)_{(n)} = \alpha_{(n)} - \frac{1}{\mathbf{a}_{(n)} : \Delta\boldsymbol{\sigma}^*}\Phi_{(n)} \tag{B4}$$

where $\mathbf{a} = \dfrac{\partial\Phi}{\partial\boldsymbol{\sigma}}$. The initial guess of α can be simply taken as $\alpha_{(0)} = -\dfrac{\Phi^t}{\Phi^* - \Phi^t}$.

After the initial yield stress $\boldsymbol{\sigma}^0$ is found, the remaining portion of the strain increment $\Delta\boldsymbol{\varepsilon} = (1-\alpha)\Delta\boldsymbol{\varepsilon}^*$ can be treated in an elasto-plastic manner.

- STEP 2: Forward-Euler return.

In the elasto-plastic region, the forward Euler scheme is used to compute the plastic portion of the strain increment. The key is to find the plastic multiplier $\Delta\lambda$.

The consistency condition is applied:

$$\dot{\Phi} = \frac{\partial \Phi}{\partial \boldsymbol{\sigma}} : \dot{\boldsymbol{\sigma}} + \frac{\partial \Phi}{\partial \sigma_M} \frac{\partial \sigma_M}{\partial \varepsilon_M^p} \dot{\varepsilon}_M^p + \frac{\partial \Phi}{\partial f^*} \frac{\partial f^*}{\partial f} \dot{f} + \frac{\partial \Phi}{\partial D_s} \dot{D}_s = 0 \tag{B5}$$

$$\dot{\boldsymbol{\sigma}} = \mathbf{C} : (\dot{\boldsymbol{\varepsilon}} - \dot{\boldsymbol{\varepsilon}}^p) = \mathbf{C} : (\dot{\boldsymbol{\varepsilon}} - \dot{\lambda}\mathbf{n}), \tag{B6}$$

where $\mathbf{n} = \frac{\partial \Theta}{\partial \boldsymbol{\sigma}}$. For associated flow rule, $\mathbf{n} = \mathbf{a}$.

Substitute Eq. (B6) into Eq. (B5)

$$\dot{\Phi} = \mathbf{a} : \mathbf{C} : (\dot{\boldsymbol{\varepsilon}} - \dot{\lambda}\mathbf{n}) + H\dot{\lambda} = 0, \tag{B7}$$

where H is the hardening modulus

$$H = -\left(h_M \frac{\partial \Phi}{\partial \sigma_M} \frac{\partial \varepsilon_M^p}{\partial \lambda} + \frac{\partial \Phi}{\partial f^*} \frac{\partial f^*}{\partial f} \frac{\partial f}{\partial \lambda} + \frac{\partial \Phi}{\partial D_s} \frac{\partial D_s}{\partial \lambda} \right) \tag{B8}$$

The derivatives in Eq. (B8) are defined as in Eq. (A5).

The rate form of plastic multiplier can be derived from the above

$$\dot{\lambda} = \frac{\mathbf{a} : \mathbf{C} : \dot{\boldsymbol{\varepsilon}}}{\mathbf{a} : \mathbf{C} : \mathbf{n} + H} \tag{B9}$$

The incremental form $\Delta\lambda$ is obtained through forward-Euler integration, which assumes all derivatives are computed at the beginning of plastic loading:

$$\Delta\lambda = \frac{\mathbf{a}^{(0)} : \mathbf{C} : \Delta\boldsymbol{\varepsilon}}{\mathbf{a}^{(0)} : \mathbf{C} : \mathbf{n}^{(0)} + H^{(0)}}, \tag{B10}$$

Consequently, the stress tensor and internal variables at $t + \Delta t$ can be updated:

$$\boldsymbol{\sigma}^{(1)} = \boldsymbol{\sigma}^{*} - \Delta\lambda\, \mathbf{C} : \mathbf{n}^{(0)} \quad , \qquad \varepsilon_M^{p\,(1)} = \varepsilon_M^{p\,t} + \left(\frac{\partial \varepsilon_M^p}{\partial \lambda}\right)^{(0)} \Delta\lambda ,$$

$$f^{(1)} = f^{t} + \left(\frac{\partial f}{\partial \lambda}\right)^{(0)} \Delta\lambda , \qquad D_s^{(1)} = D_s^{t} + \left(\frac{\partial D_s}{\partial \lambda}\right)^{(0)} \Delta\lambda \tag{B11}$$

• STEP 3: Further relaxation to the yield surface.

In general, the stress tensor obtained from the forward-Euler procedure above lies outside the yield surface, and needs further corrections back to the yield surface. The 'operator splitting' method proposed by Simo and Ortiz [102] is adopted, which assumes fixed total strain and introduces additional plastic strain in order to 'relax' the stress tensor onto the yield surface.

For each iteration step of the relaxation, all the derivatives are computed with the current values of the stress and internal variables. The stress and internal variables can be updated as follows:

$$\boldsymbol{\sigma}^{(k+1)} = \boldsymbol{\sigma}^{(k)} - \delta\lambda^{(k)} \mathbf{C} : \mathbf{n}^{(k)}, \qquad \varepsilon_M^{p\,(k+1)} = \varepsilon_M^{p\,(k)} + \left(\frac{\partial \varepsilon_M^p}{\partial \lambda}\right)^{(k)} \delta\lambda^{(k)},$$

$$f^{(k+1)} = f^{(k)} + \left(\frac{\partial f}{\partial \lambda}\right)^{(k)} \delta\lambda^{(k)}, \quad D_s^{(k+1)} = D_s^{(k)} + \left(\frac{\partial D_s}{\partial \lambda}\right)^{(k)} \delta\lambda^{(k)}, \tag{B12}$$

where $\delta\lambda^{(k)}$ is the plastic multiplier increment during the relaxation iteration step *k*, and can be derived from the truncated Taylor series of yield function

$$\Phi^{(k+1)}\left(\boldsymbol{\sigma}, \sigma_M, f^*, D_s^*\right) = \Phi^{(k+1)}(\delta\lambda^{(k)}) = \Phi^{(k)} + \left(\frac{\partial\Phi}{\partial\lambda}\right)^{(k)} \delta\lambda^{(k)} = 0 \tag{B13}$$

Combine Eq. (B13) with Eq. (B7) and Eq. (B8),

$$\delta\lambda^{(k)} = \frac{\Phi^{(k)}}{\mathbf{a}^{(k)} : \mathbf{C} : \mathbf{n}^{(k)} + H^{(k)}} \tag{B14}$$

The relaxation process will iterate until convergence is achieved.

Note: The relaxation step after initial return is the same as the Cutting Plane Method (CPM) [103]. CPM computes the derivatives at the trial stress for the initial return step, and does not use information at the initial yield point. Since the trial stress is usually much different from the real stress, this results in errors in computing internal variables, such as ε_M^p in the Gurson-type model. This error will be magnified once time increment is comparatively large. The integration method adopted here avoids this problem by using the derivatives at the initial yield point.